

THE DESIGN SPACE EXPLORATION AND PRELIMINARY  
TESTING OF A NEW CLASS OF TAILSITTING  
QUADROTOR AIRCRAFT

By

Eric Bodlak

Submitted to the graduate degree program in the Department of Aerospace Engineering  
and the Graduate Faculty of The University of Kansas in partial fulfillment of the  
requirements for the degree of Master of Science.

---

Chairperson: Dr. Ron Barrett

---

Dr. Shawn Keshmiri

---

Dr. Ray Taghavi

Date Defended: December 16, 2016

The Dissertation Committee for Eric Bodlak certifies that this is the approved version of the following dissertation :

The Design Space Exploration and Preliminary Testing of a New Class of Tailsitting Quadrotor Aircraft

---

Chairperson: Dr. Ron Barrett

Date Approved: December 16, 2016

## ACKNOWLEDGMENTS

The author would like to thank Dr. Barrett, Dr. Keshmiri, and Dr. Taghavi for overseeing this thesis, and Dr. Richard Bramlette his assistance throughout the project's duration, Ryan Bodlak for his many miscellaneous contributions, and the faculty and students of the University of Kansas Aerospace Department for building and sustaining a tradition of excellence within the program.

## ABSTRACT

Within the last decade, multi-rotor aircraft have become the most prevalent form of unmanned aerial vehicle (UAV), with applications in the military, commercial, and civilian sectors. This is due primarily to advances in electronics that allow small-scale aircraft systems to be produced and controlled in an affordable manner. Such systems are maneuvered by precisely varying the thrust and torque of individual rotors to produce flight control forces, thereby eliminating much of the mechanical complexity inherent in conventional helicopter configurations.

Although many UAV missions exploit the ability to hover in place, many also require the ability to quickly and efficiently dash from point to point. Rotorcraft, in general, are limited in this capacity, since rotor thrust must also be used to produce lift. Transitional aircraft represent an alternative that blends the vertical take-off and landing (VTOL) capabilities of rotorcraft with the forward flight performance of fixed-wing aircraft, but they often rely on cumbersome mechanisms, such as additional or rotating powerplants. UAVs, however, have no need to maintain cockpit orientation. Consequently, a tailsitting quadcopter concept was devised by Dr. Ron Barrett to combine quadcopter hovering performance with the high-speed flight of fixed-wing craft.

This paper lays out the arguments for such an aircraft — the XQ-139 — and examines the performance of XQ-139 variants with installed power values ranging from 100 W to 10,000 kW. Battery-electric, rotary engine, turboprop, and hybrid propulsive options are considered, and the merits of each discussed.

Additionally, an XQ-139 prototype was designed and constructed, and stationary test was used to compare the aircraft's installed efficiency with that of a typical quadcopter. The prototype was found to be approximately 5% more efficient in hover mode than the quadcopter to which it was compared.

# CONTENTS

<b>1</b>	<b>Introduction</b>	<b>1</b>
1.1	Background . . . . .	1
1.1.1	Unmanned Aerial Vehicles . . . . .	2
1.1.2	Multi-Rotor Aircraft . . . . .	6
1.1.3	Convertible Aircraft . . . . .	8
1.1.4	DARPA VTOL X-Plane Program . . . . .	11
1.2	Focus . . . . .	12
1.2.1	The XQ-139 Aircraft Family . . . . .	14
1.2.2	Applications . . . . .	23
<b>2</b>	<b>Theory and Performance Bounds</b>	<b>25</b>
2.1	Configuration . . . . .	25
2.2	Propulsion . . . . .	27
2.2.1	Battery-Electric Propulsion . . . . .	27
2.2.2	Rotary Engine Propulsion . . . . .	34
2.2.3	Turboshaft and Turboprop Propulsion . . . . .	39
2.2.4	Hybrid-electric Propulsion . . . . .	41
2.2.5	Rotor Performance Modeling . . . . .	43
2.3	Aerodynamics . . . . .	49
2.4	Structures and Weights . . . . .	53
2.5	Transition Strategy . . . . .	55
2.6	Performance . . . . .	57
<b>3</b>	<b>XQ-139B Design and Construction</b>	<b>63</b>
3.1	Sizing . . . . .	64
3.2	Propulsion . . . . .	65
3.3	Electronics . . . . .	65
3.4	Structures . . . . .	67
3.5	Summary . . . . .	69

<b>4</b>	<b>Testing and Results</b>	<b>70</b>
<b>5</b>	<b>Conclusions and Future Work</b>	<b>74</b>
5.1	Conclusions . . . . .	74
5.2	Future Work . . . . .	75
<b>Appendices</b>		
<b>A</b>	<b>Figure of Merit Data for VTOL Aircraft</b>	<b>77</b>
<b>B</b>	<b>Aviation Powerplant Scaling Trends</b>	<b>78</b>
B.1	Data for Electric Motor Scaling Trends . . . . .	78
B.2	Data for Rotary Engine Scaling Trends . . . . .	80
B.3	Data for Turboprops and Turboshaft Scaling Trends . . . . .	81
<b>C</b>	<b>Miscellaneous Battery Data</b>	<b>82</b>
<b>D</b>	<b>Data for Carson Cruise Efficiency Comparison</b>	<b>83</b>
<b>E</b>	<b>International Standard Atmosphere</b>	<b>84</b>
	<b>References</b>	<b>85</b>

## LIST OF FIGURES

1.1	General Atomics MQ-9 Reaper. . . . .	2
1.2	Aerovironment RQ-11 Raven. . . . .	2
1.3	A.M. Low’s Aerial Target. . . . .	3
1.4	Kettering Bug. . . . .	3
1.5	Radioplane OQ-2. . . . .	3
1.6	Fritz X Glide Bomb. . . . .	3
1.7	USD-1 Observer. . . . .	4
1.8	Ryan Firebee. . . . .	4
1.9	IAI Scout. . . . .	4
1.10	AAI RQ-2 Pioneer. . . . .	4
1.11	AAI RQ-7 Shadow. . . . .	5
1.12	MQ-1 Predator. . . . .	5
1.13	U.S. Department of Defense UAS Inventory. . . . .	6
1.14	Northrop Grumman MQ-8. . . . .	7
1.15	Gyrodyne QH-50 DASH. . . . .	7
1.16	Oehmichen No. 2. . . . .	8
1.17	Jerome-de Bothezat Helicopter. . . . .	8
1.18	DJI Phantom 3. . . . .	8
1.19	Mobile Recon Systems KittyHawk. . . . .	8
1.20	Dornier Do 31. . . . .	9
1.21	Lockheed Martin F-35B Lightning II. . . . .	9
1.22	Canadair CL-84. . . . .	9
1.23	Bell Boeing V-22 Osprey. . . . .	9
1.24	Hawker Siddeley Harrier. . . . .	9
1.25	Ryan VZ-3 Vertiplane. . . . .	9
1.26	Heinkel Lerche II concept. . . . .	10
1.27	Convair XFY-1 Pogo. . . . .	10
1.28	Northrop Grumman TERN concept. . . . .	10
1.29	XQ-138 UAV. . . . .	10

1.30	KUTRI QuadraPlex Concept. . . . .	11
1.31	Aurora Flight Sciences LightningStrike Concept. . . . .	11
1.32	QuadRKT prototypes. . . . .	12
1.33	VTOL aircraft and propulsion concepts. . . . .	13
1.34	Installed hover figures of merit vs. top speed for historical VTOL aircraft. . . . .	14
1.35	Control degrees of freedom for the XQ-139 in the x-orientation. . . . .	15
1.36	Control degrees of freedom for the XQ-139 in the plus-orientation. . . . .	15
1.37	Retreating blade stall. . . . .	16
1.38	Vertical cross-flow drag comparison for rotorcraft with matched disk areas. . . . .	17
1.39	Comparison of counter-torque strategies for helicopters and multi-rotor aircraft. . . . .	18
1.40	Helicopter and multi-rotor airfoil sections. . . . .	19
1.41	Multi-rotor blade manufactured with near-ideal taper and twist. . . . .	20
1.42	Typical helicopter rotor blade. . . . .	20
1.43	Balance of forces and moments during standard multi-rotor translation. . . . .	21
1.44	Balance of forces and moments during XQ-139 in-plane translation. . . . .	21
1.45	Typical quadrotor gust response. . . . .	22
1.46	XQ-139 gust response. . . . .	22
1.47	Honeywell RQ-16a T-Hawk FCS Class I OAV. . . . .	24
2.1	XQ-139 configuration variants. . . . .	26
2.2	Takeoff and landing footprint of representative VTOL aircraft for matched disk areas. . . . .	26
2.3	Powerplant efficiency vs. rated power. . . . .	27
2.4	Powerplant mass vs. rated power. . . . .	27
2.5	Powerplant diameter vs. rated power. . . . .	27
2.6	Powerplant volume vs. rated power. . . . .	27
2.7	Installed specific properties for considered propulsion systems. . . . .	28
2.8	Pack vs. cell-level specific energy relationship for mass estimates. . . . .	28
2.9	Airbus E-Fan. . . . .	29
2.10	Joby Aviation S2 concept. . . . .	29
2.11	3D normalized motor efficiency map. . . . .	29
2.12	2D normalized motor efficiency map. . . . .	29
2.13	Motor efficiency vs. rated power. . . . .	30
2.14	Motor mass vs. rated power. . . . .	30
2.15	Motor diameter vs rated power. . . . .	30
2.16	Peak motor speed vs. rated power. . . . .	30
2.17	Comparison of battery specific properties . . . . .	31
2.18	Lifetime vs. initial battery costs per Wh. . . . .	31



2.19	Discharge curves for various battery chemistries. . . . .	32
2.20	G/NMC discharge curves for battery model. . . . .	33
2.21	Rotary-powered CybAero Vantage UAV. . . . .	34
2.22	E-Go rotary-powered light sport aircraft. . . . .	34
2.23	Relative rotary and piston engine size comparison. . . . .	35
2.24	3D normalized rotary engine SFC map. . . . .	36
2.25	2D normalized rotary engine SFC map. . . . .	36
2.26	Rotary engine SFC vs. rated power. . . . .	36
2.27	Rotary engine mass vs. rated power. . . . .	36
2.28	Rotary engine diameter vs. rated power. . . . .	36
2.29	Peak rotary engine speed vs. rated power. . . . .	36
2.30	Altitude effects on engine output power and supercharger power consumption. . . . .	37
2.31	Altitude effects on exhaust jet thrust increment. . . . .	38
2.32	Turboprop SFC vs. power. . . . .	40
2.33	Turboprop mass vs. power. . . . .	40
2.34	Turboprop diameter vs. rated power. . . . .	40
2.35	Turboprop output speed vs. power. . . . .	40
2.36	NASA GL-10 prototype. . . . .	41
2.37	Horizon X3 hybrid concept. . . . .	41
2.38	NASA's LEAPTech concept. . . . .	42
2.39	Series hybrid architecture. . . . .	43
2.40	Parallel hybrid architecture. . . . .	43
2.41	Control volume for ideal rotor momentum theory. . . . .	44
2.42	Definition of 2D blade element parameters. . . . .	45
2.43	Rotor diameter scaling trends for the XQ-139 concept. . . . .	49
2.44	Maximum rotor figure of merit scaling trends for the XQ-139 concept. . . . .	49
2.45	Maximum 2D lift-to-drag ratio for NACA 00XX airfoil space. . . . .	50
2.46	Angle of attack at maximum 2D lift-to-drag ratio for NACA 00XX airfoil space. . . . .	50
2.47	Zero-lift drag coefficient for NACA 00XX airfoil space. . . . .	50
2.48	Maximum 2D lift coefficient for NACA 00XX airfoil space. . . . .	50
2.49	XQ-139 2D and 3D lift coefficients for A=6 and RE=50,000. . . . .	52
2.50	XQ-139 2D and 3D lift-to-drag ratios for an A=6 and RE=50,000. . . . .	52
2.51	Feathered rotor drag coefficient for model-optimized rotors. . . . .	53
2.52	XQ-139 empty mass fraction scaling trends as modeled. . . . .	55
2.53	XQ-139 entry transition. . . . .	56
2.54	XQ-139 exit transition. . . . .	56

2.55	Comparison of $T/(W_{use}V_C)$ for XQ-139 and other aircraft options. . . . .	58
2.56	Sizing trends for XQ-139 design. . . . .	59
2.57	Cruise SFC scaling trends. . . . .	59
2.58	XQ-139 cruise power scaling trends. . . . .	59
2.59	Cruise efficiency scaling trends. . . . .	59
2.60	XQ-139 cruise speed scaling trends. . . . .	59
2.61	XQ-139 cruise L/D scaling trends. . . . .	59
2.62	XQ-139 rotorcraft endurance scaling trends. . . . .	60
2.63	XQ-139 maximum endurance scaling trends. . . . .	60
2.64	XQ-139 cruise range scaling trends. . . . .	61
2.65	Cruise range scaling trends for XQ-139 hybrid propulsion. . . . .	61
3.1	XQ-139A prototype. . . . .	63
3.2	XQ-139B design. . . . .	63
3.3	E-flite Power 10 brushless DC motor. . . . .	64
3.4	APC 12X6E propeller. . . . .	65
3.5	XQ-139B propulsion system. . . . .	65
3.6	SP Racing F3 Deluxe. . . . .	66
3.7	APC 12X6E propeller. . . . .	66
3.8	APC 12X6E propeller. . . . .	66
3.9	Nose-mounted electronics bay. . . . .	66
3.10	ESC installation. . . . .	66
3.11	Servos installed for control surface actuation. . . . .	67
3.12	XQ-139 structural makeup. . . . .	68
3.13	XQ-139B main quadrant tool. . . . .	68
3.14	XQ-139B nose tool. . . . .	68
3.15	XQ-139B prototype. . . . .	69
4.1	Turnigy H.A.L. for comparative testing. . . . .	70
4.2	H.A.L. frame constrained for efficiency testing. . . . .	71
4.3	Electrical power draw versus rotor speed test results. . . . .	72
4.4	Comparison of estimated figures of merit (installed). . . . .	72
4.5	XQ-139B constrained for efficiency testing. . . . .	73

## LIST OF TABLES

1.1	Future Combat Systems Proposed UAV Classes. . . . .	23
2.1	Current-market lithium-ion batteries and specific properties. <sup>(96-104)</sup> . . . . .	33
2.2	FAA limit load factor requirements by aircraft category <sup>(135-138)</sup> . . . . .	53
2.3	Example XQ-139 UAS. . . . .	62
A.1	Figure of merit data for VTOL aircraft . . . . .	77
B.1	Data for electric motor scaling trends . . . . .	78
B.3	Data for rotary engine scaling trends . . . . .	80
B.4	Data for turboprops and turboshaft scaling trends . . . . .	81
C.1	Vehicle cell and pack-level battery data . . . . .	82
D.1	Data for Carson cruise efficiency comparison . . . . .	83
E.1	International Standard Atmosphere . . . . .	84

## LIST OF SYMBOLS

$A$	Rotor actuator disk area.
$A$	Wing aspect ratio.
$a'$	Swirl factor.
$b$	Aircraft wingspan.
$C_{D90}$	Drag coefficient at $90^\circ$ .
$C_L$	Lift coefficient.
$C_{L\alpha}$	3D lift curve slope.
$c$	Nondimensional blade chord.
$D$	Diameter.
$d$	Fuselage diameter.
$dP$	Elemental power.
$dQ$	Elemental torque.
$dT$	Elemental thrust.
$F$	Fuselage lift factor.
$F$	Prandtl tip-loss function.
$FM$	Rotor figure of merit.
$f_h$	Hub parameter.
$f_t$	Tip-loss parameter.
$h$	True altitude.
$h_{crit}$	Critical altitude.
$I_{ref}$	Reference current.
$L/D$	Lift-to-drag ratio.
$M$	Mach number.

$m$	Mass.
$N_b$	Number of rotor blades.
$N_z$	Limit load factor.
$P$	Power.
$p$	Engine operating pressure.
$p_{alt}$	Power output at altitude.
$P_{amb}$	Ambient atmospheric pressure.
$Q$	Torque.
$q$	Dynamic pressure.
$R$	Rotor radius.
$r$	Nondimensionalized radial position.
$RE$	Reynolds number.
$S_{exposed}$	Exposed wing area.
$S_{ref}$	Planform reference area.
$T$	Total rotor thrust.
$T_{ref}$	Reference temperature.
$V_\infty$	Freestream velocity.
$V_T$	Local tangential velocity.
$y$	Distance from rotor center to blade element.
$\Gamma$	Wing dihedral angle.
$\gamma$	Experimentally determined constant for Hausmann-Depcik equation.
$\Delta T_{jet}$	Incremental jet thrust.
$\delta$	Experimentally determined constant for Hausmann-Depcik equation.
$\eta$	Efficiency.
$\theta$	Local blade pitch angle.
$\theta_c$	Collective pitch angle.
$\Lambda$	Wing sweep angle.
$\lambda$	Inflow ratio.
$\lambda$	Wing taper ratio.
$\lambda_i$	Local inflow ratio.

- $\lambda_0$  . . . . . Ideal nominal inflow ratio.
- $\rho$  . . . . . Density.
- $\sigma$  . . . . . Stress.
- $\phi$  . . . . . Local inflow angle.
- $\chi$  . . . . . Experimentally determined constant for Hausmann-Depcik equation.
- $\Omega$  . . . . . Rotor rotational velocity.

## LIST OF ABBREVIATIONS

<b>AC</b>	Alternating current.
<b>BEMT</b>	Blade element momentum theory.
<b>BLDC</b>	Brushless direct current motor.
<b>CAS</b>	Close air support.
<b>CCA</b>	Close combat attack.
<b>CFD</b>	Computational fluid dynamics.
<b>DARPA</b>	Defense Advanced Research Projects Agency.
<b>DC</b>	Direct current.
<b>EASA</b>	European Aviation Safety Agency.
<b>ehp</b>	Equivalent horsepower.
<b>ekW</b>	Equivalent kilowatts.
<b>FAA</b>	Federal Aviation Administration.
<b>FCS</b>	Future Combat Systems.
<b>ICE</b>	Internal combustion engine.
<b>KUTRI</b>	University of Kansas Transportation Research Institute.
<b>LFP</b>	Lithium iron phosphate.
<b>MAV</b>	Micro air vehicle.
<b>MTOW</b>	Maximum takeoff weight.
<b>NMC</b>	Lithium nickel manganese cobalt oxide.
<b>OAV</b>	Organic air vehicle.
<b>RC</b>	Radio-controlled.
<b>RPM</b>	Revolutions per minute.
<b>SFC</b>	Specific fuel consumption.

**SOC** . . . . . State of charge.  
**TERN** . . . . . Tactically Exploited Reconnaissance Node.  
**UAS** . . . . . Unmanned aircraft system.  
**UAV** . . . . . Unmanned aerial vehicle.  
**VTOL** . . . . . Vertical takeoff and landing.



*“Ah, the helix,” replied Phil Evans. “But the bird has no helix; That we know!” “So,” said Robur; ”but Penaud has shown that in reality the bird makes a helix, and its flight is helicopteral. The motor of the future is the screw.”*

— Jules Verne, *The Clipper of the Clouds*, 1887<sup>(4)</sup>

# 1 INTRODUCTION

## Contents

---

<b>1.1 Background</b>	<b>1</b>
1.1.1 Unmanned Aerial Vehicles	2
1.1.2 Multi-Rotor Aircraft	6
1.1.3 Convertible Aircraft	8
1.1.4 DARPA VTOL X-Plane Program	11
<b>1.2 Focus</b>	<b>12</b>
1.2.1 The XQ-139 Aircraft Family	14
1.2.2 Applications	23

---

## 1.1 Background

Unmanned aerial vehicles (UAVs) find numerous applications in the military, commercial, and private sectors. Most UAVs (commonly called drones) are piloted remotely, but others can operate autonomously. Without the need for an onboard pilot, UAVs can be made smaller and more affordably than their manned counterparts and can be used for missions that are considered too dangerous or extreme for humans. The General Atomics MQ-1 Predator, an example military drone, is used for reconnaissance and attack missions, while civilian UAV functions vary from remote sensing and security operations to photography and package delivery.

UAVs can range considerably in size. Some military aircraft, like the General Atomics MQ-9 Reaper (Figure 1.1), have a maximum takeoff weight (MTOW) of over 10,000 lb, whereas the AeroVironment RQ-11 Raven (Figure 1.2) weighs in at under five pounds. Commercial UAVs, which must abide by civil aviation regulations, are generally under 220



**Fig. 1.1:** General Atomics MQ-9 Reaper.<sup>(1)</sup>



**Fig. 1.2:** Aerovironment RQ-11 Raven.<sup>(2)</sup>

lb MTOW,<sup>(3)</sup> and recreational drones are even smaller, with many not intended to carry payload at all.

While the bulk of UAV production (in terms of revenue) is military,<sup>(5)</sup> Deloitte estimates that 300,000 non-military drones are being sold annually and that the global commercial/consumer fleet has grown to over 1 million units.<sup>(6)</sup> The Teal Group projects that annual production of unmanned aircraft systems (UAS) will rise from US\$4 billion to \$14 billion by 2025, with commercial and civil markets experiencing the most growth in that time period. To better understand how the global UAV fleet has reached its current state and to set the stage for the topic of this thesis, the background of several relevant classes of aircraft will be examined in Section 1.1.1, including UAVs, multi-rotors, and convertible aircraft. Then, in Section 1.2, the scope of this paper will be narrowed to the design of a specific configuration – that of the XQ-139 vehicle family.

### 1.1.1 Unmanned Aerial Vehicles

In 1898, Nikola Tesla demonstrated<sup>(7)</sup> and patented<sup>(8)</sup> the world's first remotely-piloted vehicle, a three-foot radio-controlled (RC) boat that he believed would have numerous military applications. Seventeen years later, following advances in the field of aeronautics, Tesla extended his RC concept to aircraft during an interview for the New York Times, in what was the first public mention of a radio-controlled aircraft.<sup>(9)</sup>

In 1916, Archibald Montgomery Low devised the “Aerial Target” (Figure 1.3) for the British Royal Air Force.<sup>(12)</sup> The Aerial Target was a remotely-piloted aircraft that was intended to counteract German Zeppelin airships, while also functioning as a guided bomb.

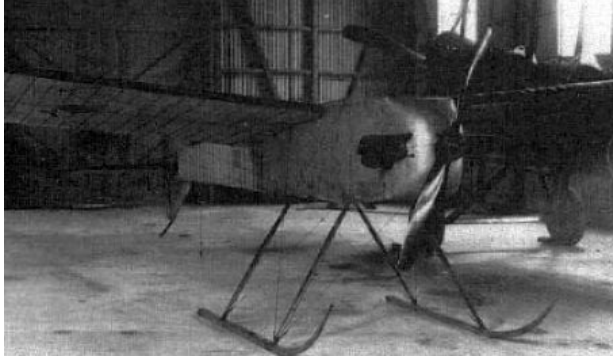


**Fig. 1.3:** A.M. Low's Aerial Target.<sup>(10)</sup>

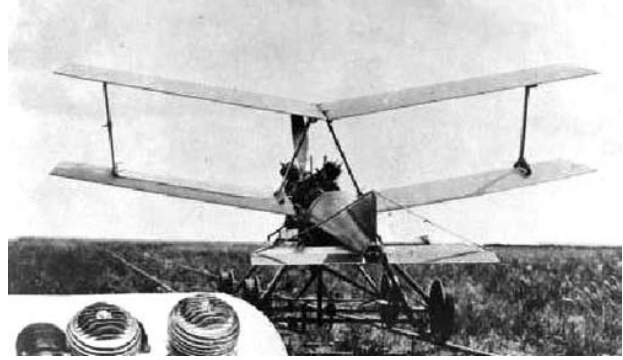


**Fig. 1.4:** Kettering Bug.<sup>(11)</sup>



**Fig. 1.5:** Radioplane OQ-2.<sup>(15)</sup>

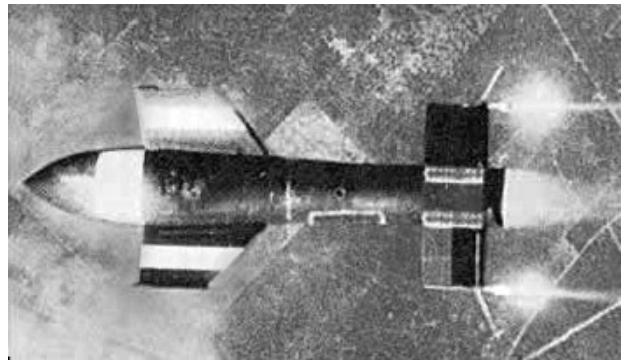


**Fig. 1.6:** Fritz X Glide Bomb.<sup>(16)</sup>

The project was unsuccessful and eventually abandoned, but as the first of its kind, it pointed toward the future.

Low's efforts were soon followed by American attempts at developing "aerial torpedoes" such as the Hewitt-Sperry Automatic Airplane and the Kettering Bug (Figure 1.4), which are considered precursors to the modern cruise missile. These endeavors, however, relied on gyroscopes instead of radio control for guidance.<sup>(13)</sup> In 1924, a radio-controlled Curtiss F-5L became the first aircraft to be remotely piloted through all flight phases, but in World War I's wake, most research regarding guided weapons and UAVs was terminated or suspended.<sup>(14)</sup> It would be over a decade before such projects were again seriously entertained.

From the mid-1930s through the end of World War II, radio-controlled target drones – particularly the DH-82 Queen Bee and Reginald Denny's OQ-2 (Figure 1.5) – became popular training aids for both British and American military forces.<sup>(13)</sup> World War II brought about a number of advances in UAV and guided weapon technology, as the United States



**Fig. 1.7:** USD-1 Observer.<sup>(18)</sup>



**Fig. 1.8:** Ryan Firebee.<sup>(19)</sup>



**Fig. 1.9:** IAI Scout.<sup>(21)</sup>



**Fig. 1.10:** AAI RQ-2 Pioneer.<sup>(22)</sup>

launched the TDR-1, the world's first armed drone, and the Germans created the first successful precision-guided weapon, the Fritz X glide bomb (Figure 1.6),<sup>(17)</sup> which was piloted remotely from its launching aircraft.

Target drones continued to be developed and used after World War II, but it wasn't until the 1950s and 1960s that UAVs began to serve more frequently in other roles.<sup>(17)</sup> In 1955, a Radioplane OQ-19 target drone was modified for reconnaissance purposes and introduced into U.S. Army service as the USD-1 Observer (Figure 1.7).<sup>(13)</sup> Shortly thereafter, another target drone – the Ryan Firebee, seen in Figure 1.8 – was also converted for the same type of mission. The Firebee, along with the Ryan 147B Lightning Bug, saw extensive action during the Vietnam War, when over 3000 Ryan reconnaissance drones were deployed.<sup>(20)</sup>

Since that time, UAVs have gradually taken on greater roles in battlefield operations. During the 1980s, Israel was one of the leading developers of military drone technology. Israeli IAI Scout (Figure 1.9) and Tadiran Mastiff UAVs are known to have been key compo-



**Fig. 1.11:** AAI RQ-7 Shadow.<sup>(24)</sup>



**Fig. 1.12:** MQ-1 Predator.<sup>(25)</sup>

nents in Israel's victory in the 1982 Lebanon War,<sup>(23)</sup> and another Israeli aircraft, the AAI RQ-2 Pioneer (Figure 1.10), was used by U.S. forces in the Gulf War. The RQ-7 Shadow, shown in Figure 1.11, is a current successor to the Pioneer.

Building on the early successes of military UAS, the United States has embraced the technology like never before, employing an array of aircraft, including armed multi-role UAVs such as the MQ-1 Predator (Figure 1.12) and MQ-9 Reaper, both made by General Atomics. The majority of the U.S. UAV fleet, however, is made up of small UAVs and micro air vehicles (MAVs).

Military MAVs were born out of Department-of-Defense-funded research projects in the 1990s.<sup>(26)</sup> These projects were initiated with the goal of developing specialized mission-support aircraft with flight weights under 100 grams. The aircraft were intended for surveillance and sensing operations, and the resulting research led to the miniaturization of critical aircraft components – setting the stage for a future wave of MAV development.

Currently, the United States is the leading manufacturer of military UAS, spending more money on such systems than the rest of the world combined.<sup>(5)</sup> In 2013, the U.S. Department of Defense reported an inventory of over 10,000 UAVs,<sup>(28)</sup> a breakdown of which is shown in Figure 1.13. Most are small UAV platforms, such as those made by AeroVironment, but the much larger aircraft manufactured by General Atomics and Northrop Grumman (RQ-4 Global Hawk and MQ-8 Fire Scout) represent the most significant portion of the worldwide market in terms of UAS revenue and funding.

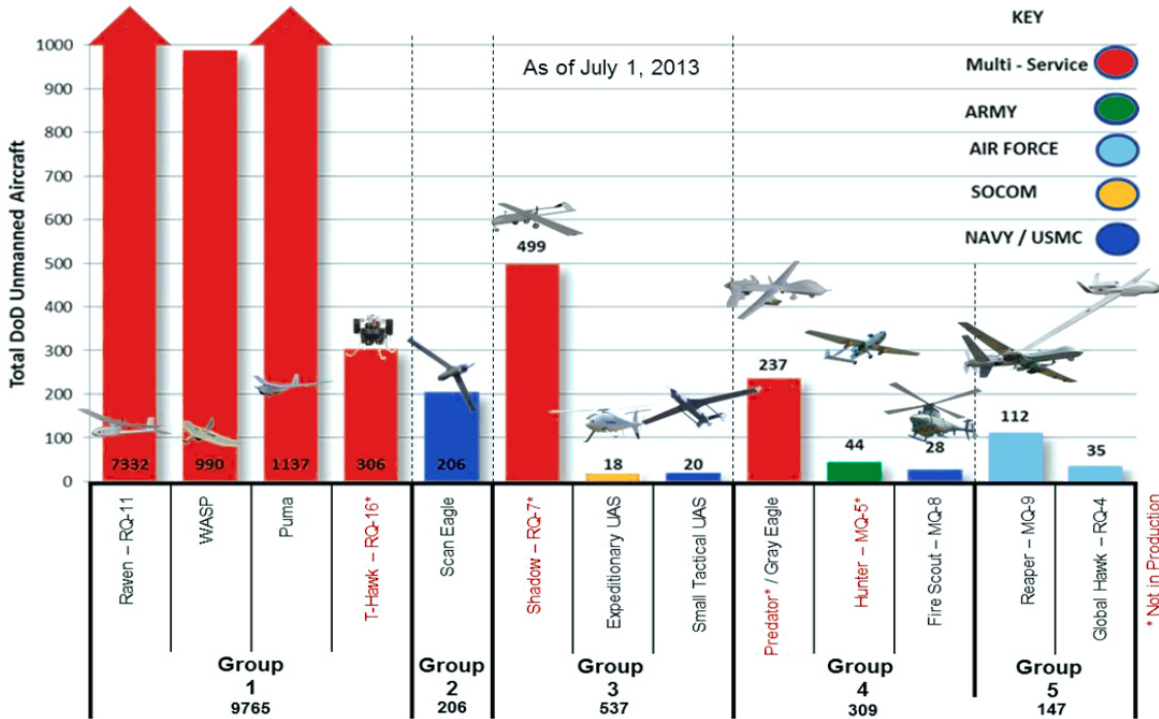


**Fig. 1.13:** U.S. Department of Defense UAS Inventory.<sup>(27)</sup>

In terms of aircraft volume, however, small aircraft used for civil and commercial purposes are much more prevalent than their military analogues. Most of these are multi-rotor aircraft, the subject of the next section.

### 1.1.2 Multi-Rotor Aircraft

While UAVs have historically been fixed-wing craft, there are exceptions such as the Northrop Grumman MQ-8 (Figure 1.14) and Gyrodyne QH-50 DASH (Figure 1.15), which was introduced by the U.S. Navy in 1963. Rotorcraft provide vertical takeoff and landing (VTOL) capabilities, as well as the ability to hover in space, but helicopters are expensive, mechanically complex, and difficult to pilot. For this reason, unmanned helicopters have been limited mainly to military applications. Recent developments in electronic components, however, have led to small, low-cost flight controllers, motors, and batteries – greatly reducing the need for pilot experience and training. With these advances, unmanned rotorcraft have become the most prevalent form of UAV in the civilian world.



**Fig. 1.14:** Northrop Grumman MQ-8.<sup>(29)</sup>



**Fig. 1.15:** Gyrodyne QH-50 DASH.<sup>(30)</sup>

The majority of these UAVs are multi-rotor aircraft and not traditional helicopters. This is because such aircraft are much simpler mechanically than helicopters, which translates to cost savings and increased reliability for small UAVs. Helicopters rely on complicated mechanisms, such as swashplates, to maneuver by collectively and cyclically varying the pitch of each rotor blade. In contrast, multi-rotor aircraft use fixed-pitch rotors and maneuver by precisely varying the thrust and torque of individual rotors to effect flight control forces. For small multi-rotor UAVs powered by electric motors, the rotors are the aircraft's only moving components – a simplicity that generally trumps a helicopter's complexity in terms of cost and reliability. The most common multi-rotor configuration is the quadcopter, since four is the minimum number of rotors that allows an aircraft to be controlled by variable rotor speeds alone.

Quadcopters are not new, as they represent some of the earliest attempts at developing hovering aircraft. The first quadcopter was the Breguet-Richet Gyroplane No. 1, which was constructed in 1907 by Breguet Aviation. Though unsuccessful, others followed, including the Oehmichen No. 2 (Figure 1.16) and the Jerome-de Bothezat helicopter (Figure 1.17), both of which achieved limited flight in the early 1920s. From 1930 onward, other configurations, specifically coaxial helicopters, tandem helicopters, and the now-common main rotor/tail rotor combination, have dominated helicopter research. In 1958, the Curtiss-Wright company developed the VZ-7 quadrotor aircraft for the U.S. Army. The aircraft was more controllable than previous quadcopters but was unable to meet the Army's performance requirements. Current multi-rotor UAVs, such as the popular DJI Phantom 3

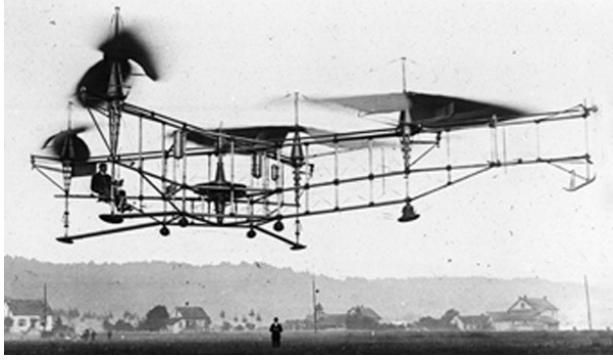


**Fig. 1.16:** Oehmichen No. 2.<sup>(31)</sup>

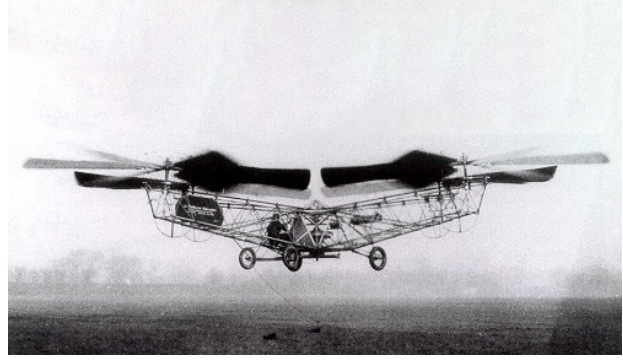


**Fig. 1.17:** Jerome-de Bothezat Helicopter.<sup>(32)</sup>



**Fig. 1.18:** DJI Phantom 3.<sup>(33)</sup>



**Fig. 1.19:** MRS KittyHawk.<sup>(34)</sup>

(Figure 1.18) and the much larger KittyHawk from Mobile Recon Systems (Figure 1.19, take advantage of modern electronics to provide operators with effortless control and reliable, versatile UAV performance.

### 1.1.3 Convertible Aircraft

Many UAV missions benefit from the ability to rapidly and efficiently dash from point to point, while at the same time having the capacity to hover in place. Fixed-wing craft, by and large, have poor low-speed performance, while rotorcraft generally have limited top-end speed and efficiency in forward flight, since rotor thrust must also be used to produce lift. Convertible aircraft represent an alternative that blends the vertical takeoff and landing capabilities of rotorcraft with the forward-flight performance of fixed-wing aircraft.

A range of convertible solutions have been developed for manned aircraft. Broadly, they can be classified as aircraft that require additional powerplants/auxiliary devices for VTOL and hovering operations, and those that use the same powerplant(s) for all





**Fig. 1.20:** Dornier Do 31.<sup>(35)</sup>



**Fig. 1.21:** Lockheed Martin F-35B.<sup>(36)</sup>



**Fig. 1.22:** Canadair CL-84.<sup>(37)</sup>



**Fig. 1.23:** Bell Boeing V-22 Osprey.<sup>(38)</sup>



**Fig. 1.24:** Hawker Siddeley Harrier.<sup>(39)</sup>



**Fig. 1.25:** Ryan VZ-3 Vertiplane.<sup>(40)</sup>

flight activities. Examples of aircraft in the first category are the Dornier Do 31 (Figure 1.20), which required eight vertically-mounted turbojets for takeoff and landing, and the Lockheed Martin F-35B Lightning II (Figure 1.21), which uses a shaft-driven lift fan and vectored engine thrust for VTOL operations. Aircraft like these are heavier and less aerodynamic than those that require only one set of powerplants.

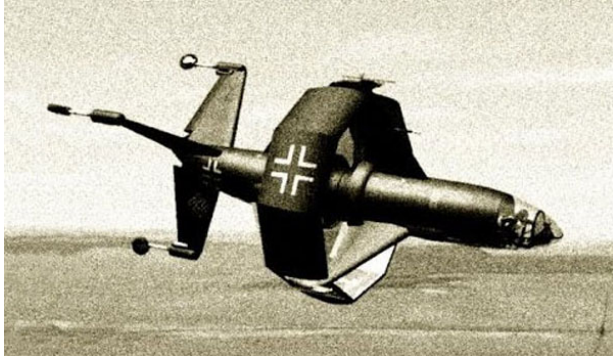


**Fig. 1.26:** Heinkel Lerche II concept.<sup>(41)</sup>



**Fig. 1.27:** Convair XFY-1 Pogo.<sup>(42)</sup>



**Fig. 1.28:** TERN concept.<sup>(43)</sup>



**Fig. 1.29:** XQ-138 UAV.<sup>(44)</sup>

This second category is more expansive, with many of its members depending on tilting mechanisms for VTOL functions. Examples include the Canadair CL-84 (Figure 1.22), a tiltwing aircraft, and the Bell Boeing V-22 Osprey (Figure 1.23), a military tiltrotor. Meanwhile, other aircraft maintain the orientation of their powerplants, but vector the thrust output. This has been done by the turbofan-powered Hawker Siddeley Harrier (Figure 1.24) and the Ryan VZ-3 (Figure 1.25), which could hover by deflecting its propeller slipstream. Finally, a class of aircraft called tailsitters achieves convertible flight by transitioning from a tail-down takeoff/landing position to a horizontal orientation for forward flight. This concept hails back to World War II in German designs such as the Heinkel Lerche II, pictured in Figure 1.26. Though the Lerche II never took flight, tailsitters were explored extensively during the 1950s and 1960s. The Convair XFY Pogo (Figure 1.27) is one of the most famous of the designs from that era. Tailsitters are the simplest convertible aircraft from a mechanical standpoint, but are difficult to pilot because of the variations in cockpit attitude during flight.

With no need to maintain cockpit orientation and with the benefit of modern electronic controls, a number of tailsitting UAVs have recently been proposed. These designs include Northrop Grumman's submission for the Tactically Exploited Reconnaissance Node (TERN) (Figure 1.28) program, which was sponsored by the Defense Advanced Research Projects Agency (DARPA),<sup>(43)</sup> and the XQ-138 designed by KU professor Dr. Ron Barrett, pictured in Figure 1.29.<sup>(44)</sup> The AeroVironment SkyTote and Google's Project Wing UAV are other notable examples.

#### 1.1.4 DARPA VTOL X-Plane Program

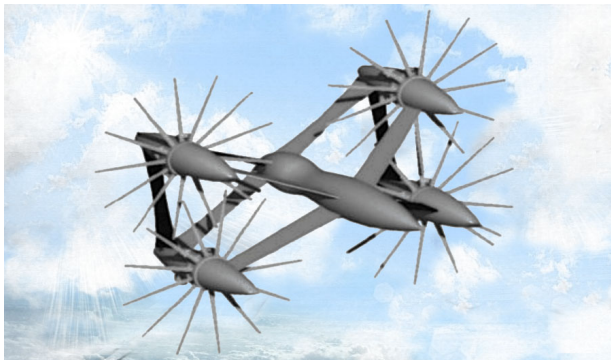


**Fig. 1.30:** KUTRI QuadraPlex concept.<sup>(45)</sup>



**Fig. 1.31:** Aurora LightningStrike concept.<sup>(46)</sup>

In 2013, DARPA announced the VTOL X-Plane program,<sup>(47)</sup> with the goal of developing an aircraft capable of vertical takeoff and landing, efficient hovering performance, and top-end speeds greater than those of conventional rotorcraft. Specifically, the program called for the following objectives to be achieved:

1. Speed: Achieve a top sustained flight speed of 300 to 400 knots
2. Hover efficiency: Raise hover efficiency from 60 percent to at least 75 percent
3. Cruise efficiency: Present a cruise lift-to-drag ratio of at least 10, up from 5 to 6
4. Useful load capacity: Maintain the ability to perform useful work by carrying a load of at least 40 percent of the vehicle's projected gross weight of 10,000-12,000 pounds

The University of Kansas Transportation Research Institute (KUTRI) submitted a design to this competition called the “Quadraplex”, shown in Figure 1.30.<sup>(45)</sup> The aircraft, conceived by Dr. Ron Barrett, was a tailsitting quadrotor aircraft that merged the hovering performance and maneuverability of a quadcopter into a high-speed UAV platform.

Though the competition was eventually won by the series-hybrid LightningStrike UAV from Aurora Flight Sciences (Figure 1.31),<sup>(48)</sup> the Quadraplex design was reimaged as the foundation for the XQ-139 family of VTOL aircraft. A start-up company (QuadRKT, LLC - Figure 1.32) and several pending patents<sup>(49)</sup> proceeding from the KUTRI proposal.



**Fig. 1.32:** QuadRKT prototypes.<sup>(50)</sup>

## 1.2 Focus

Since the 1940s, helicopters have been used for nearly all military missions requiring vertical takeoff and landing operations. Helicopters are excellent in roles where extended hovering or flexible low-speed maneuverability is required. Still, helicopters have a number of shortcomings – most notably in terms of cost, complexity, and limited capabilities in high-speed flight. Many attempts have been made at creating alternative aerial platforms that are able to combine the flexibility of helicopter operations with the speed and efficiency of conventional fixed-wing aircraft. Despite these efforts, there are no VTOL

aircraft that have been able to consistently match or outperform helicopters in their currently established roles.<sup>(47)</sup>

The American Helicopter Society's VTOL Wheel, shown in Figure 1.33, expands upon the aircraft categories discussed in Section 1.1.3. These designs are mostly undone by mechanical complexity and/or compromised performance in one or both major flight phases. It was previously mentioned that, of these options, tailsitters are the least complex from a mechanical perspective. Though manned versions have been operationally infeasible in the past, there are arguments to be made for the performance value of unmanned tailsitting designs. These arguments will be given in Section 1.2.1.

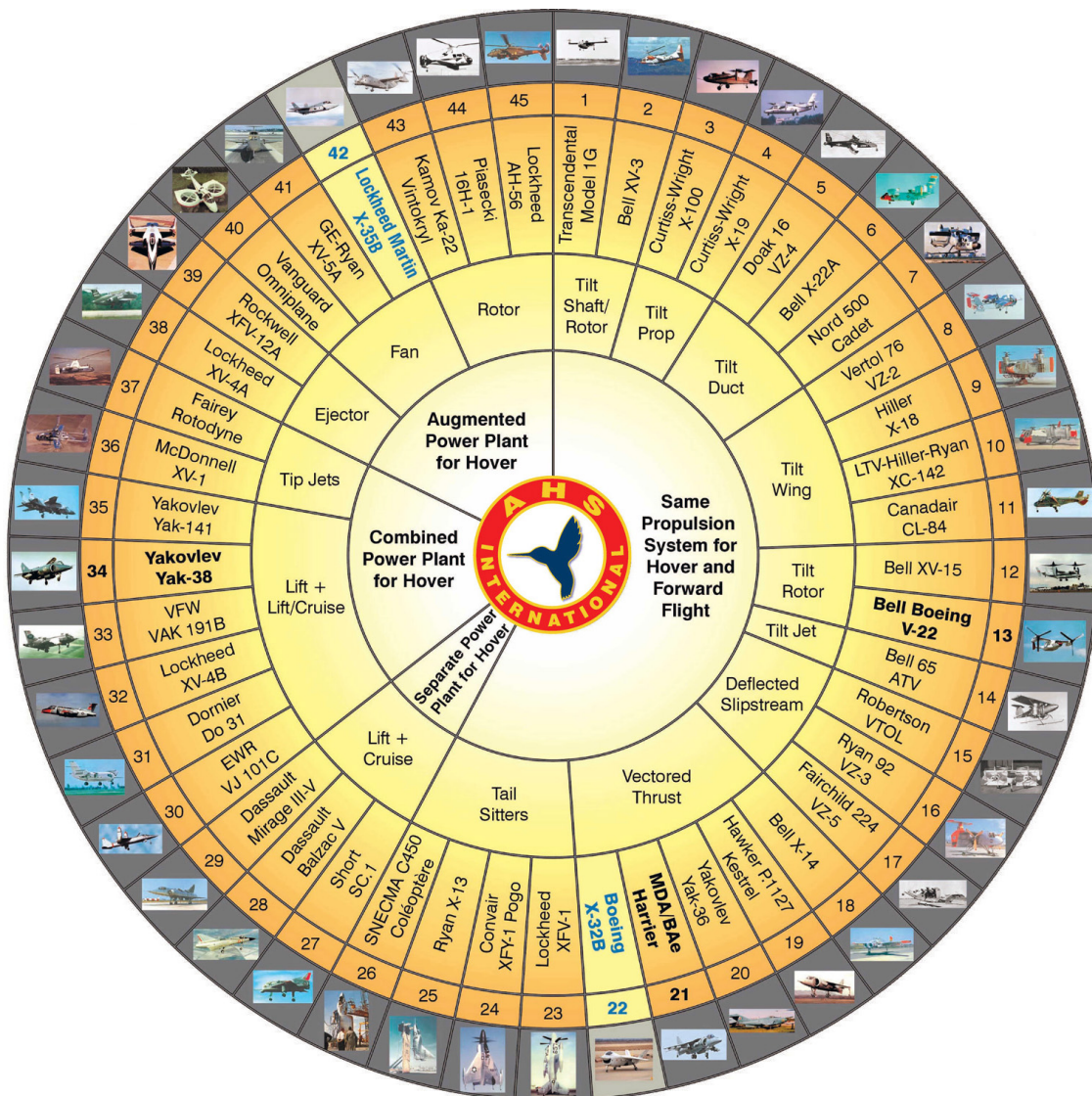


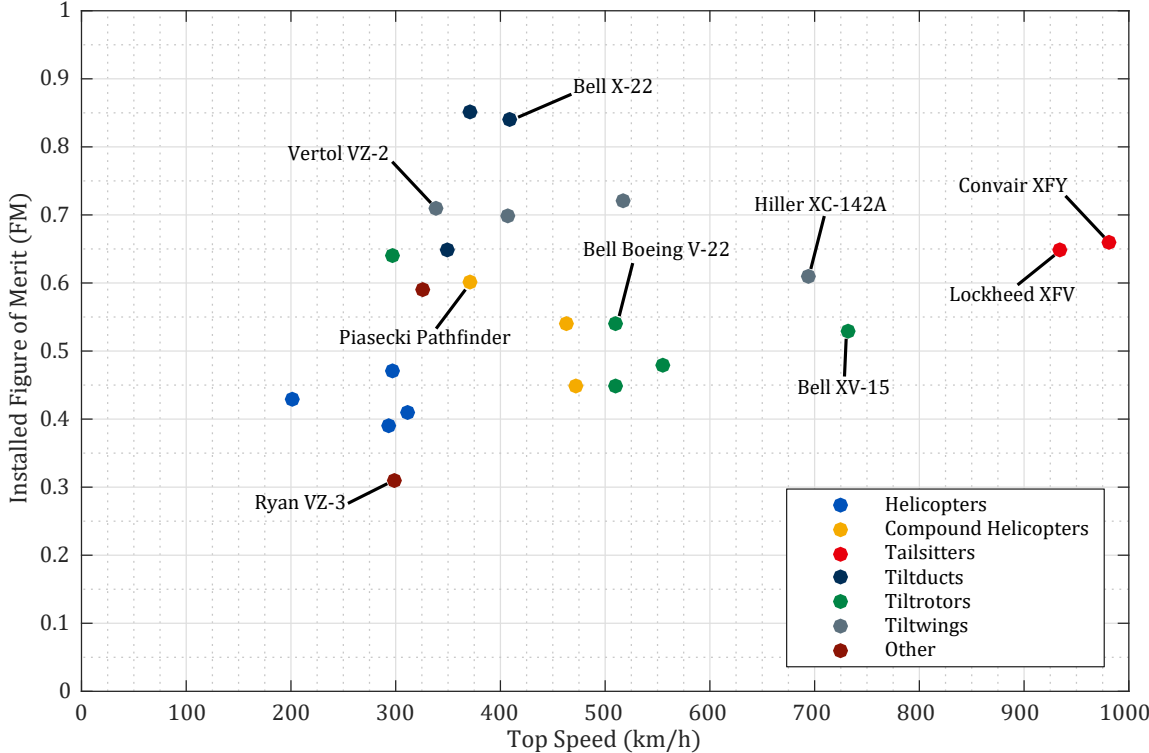
Fig. 1.33: VTOL aircraft and propulsion concepts.<sup>(51)</sup>

### 1.2.1 The XQ-139 Aircraft Family

Rotor figure of merit,  $FM$ , is a measure of rotor efficiency that compares real-world power requirements with the ideal power predicted by momentum theory for a given thrust, according to Equation 1.1.

$$P_{ideal} = \frac{T}{FM} \sqrt{\frac{T}{2\rho A}} \tag{1.1}$$

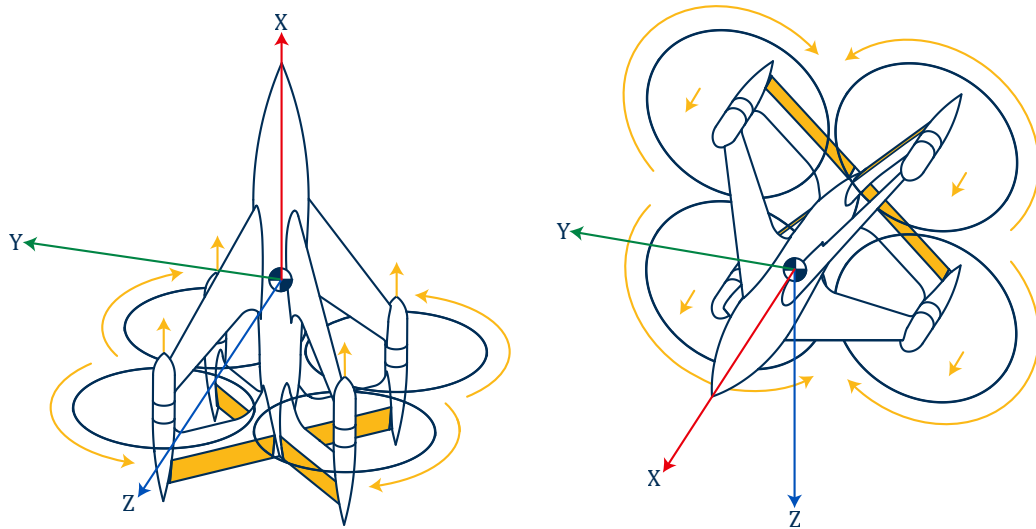
In Figure 1.34, a plot of figure of merit values versus top speed for a range of rotor-driven VTOL concepts, it can be seen that tailsitters occupy the region farthest from the origin, representing their capacity for dual-role performance.



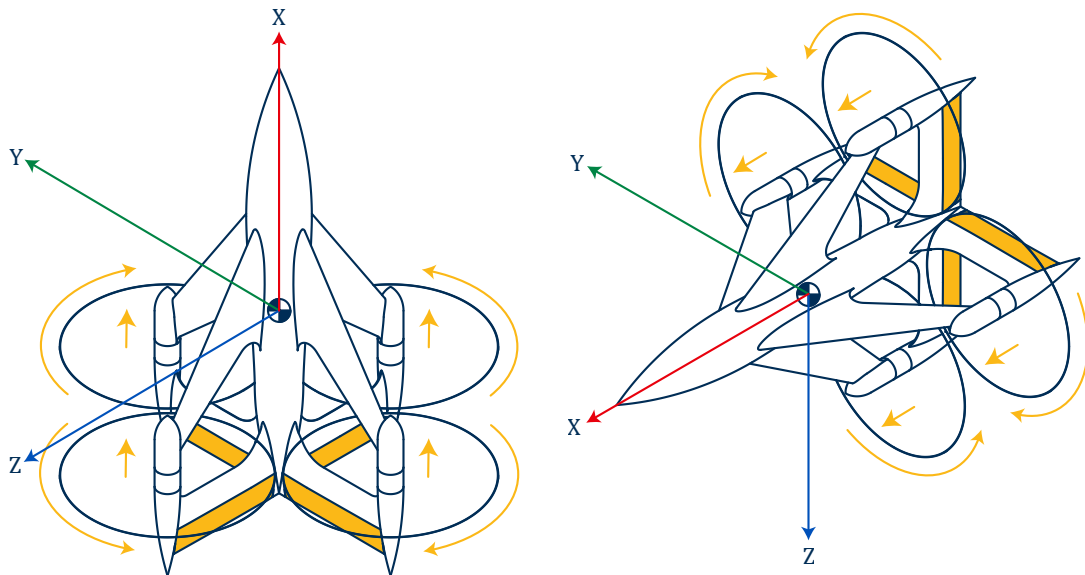
**Fig. 1.34:** Installed hover figures of merit vs. top speed for historical VTOL aircraft. <sup>(52-59)</sup>

The XQ-139 configuration consists of four rotors sandwiched between an X-wing and an X-tail. During flight, the aircraft can call upon 12 degrees of freedom for control, as shown in Figure 1.35. It can be designed to fly in either the “x” or “plus” orientation (Figures 1.35 and 1.36); each iteration has its own advantages. In the x-orientation, all

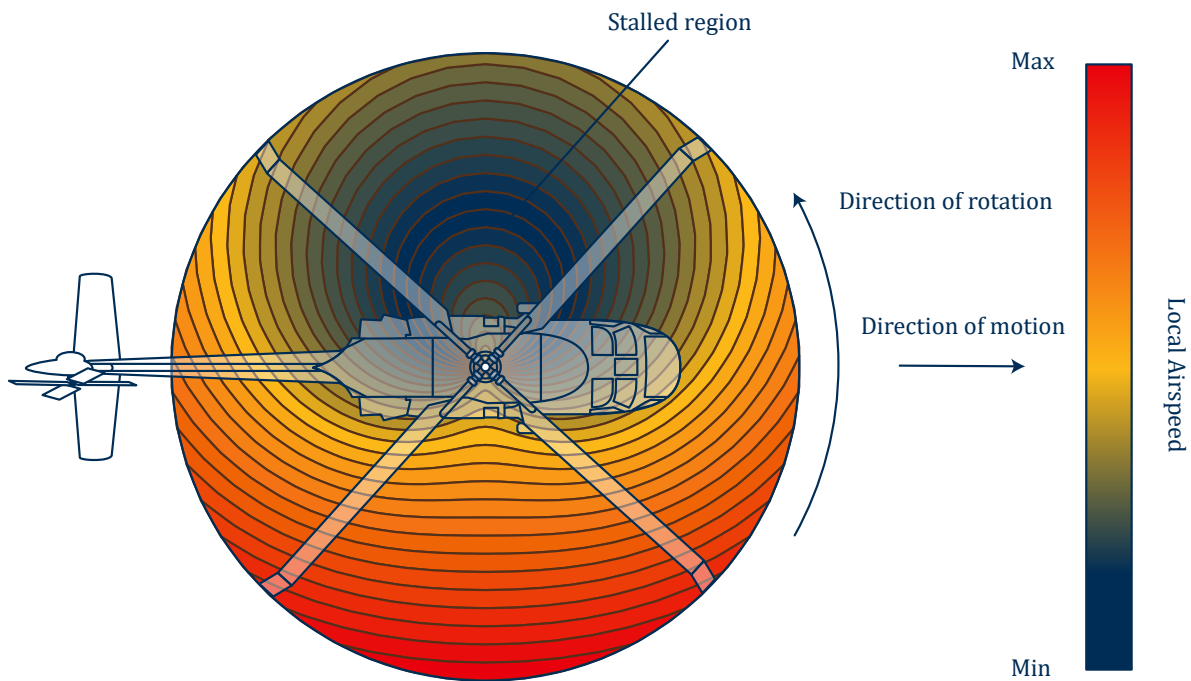
of the surfaces work to produce lift, but the aerodynamics and control scheme are more complex than for the plus-variant. The plus-orientation is simpler than the “x”, but the vertical surfaces do not contribute to the aircraft’s total lift. The aerodynamic forces may also be asymmetric due to the relative direction of rotor rotations during forward flight, when one rotor counters the wingtip vortices and the other amplifies them.



**Fig. 1.35:** Control degrees of freedom for the XQ-139 in the x-orientation.



**Fig. 1.36:** Control degrees of freedom for the XQ-139 in the plus-orientation.

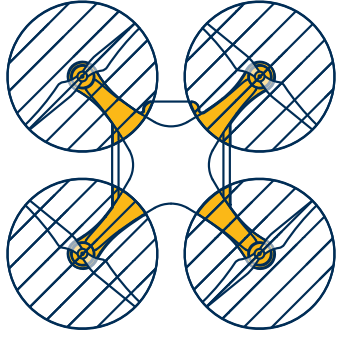
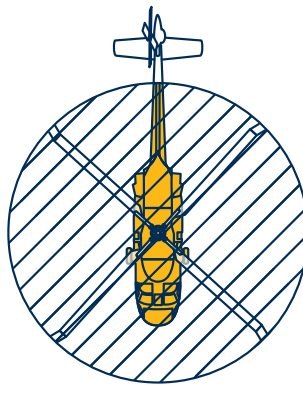
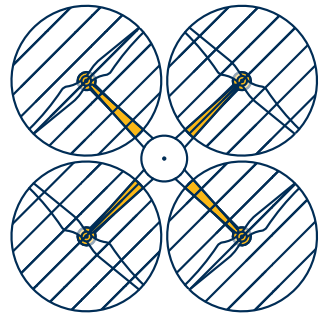








**Fig. 1.37:** Retreating blade stall.

In either case, the design's features coalesce to produce a VTOL aircraft capable of high-performance hovering and forward flight. The XQ-139 levers modern electronic control and targets unmanned mission profiles in order to circumvent the operational roadblocks that have plagued tailsitters in the past. Furthermore, it uses quadrotor propulsor architecture along with empennage control to facilitate efficient and agile hovering flight that expands upon the maneuvering capabilities of helicopters. This turns the tailsitter configuration into more than just a high-speed platform capable of vertical takeoffs and landings and instead into a true dual-role aircraft offering high performance in all flight phases.

Rotorcraft are limited in top speed by fuselage drag, lift-thrust coupling, and especially retreating blade stall (Figure 1.37). Retreating blade stall occurs when the retreating blades – blades moving in opposition to the direction of motion – exceed a critical angle of attack and stall. Up to the point of stall onset, cyclic control is used to compensate for the difference in relative airspeeds, and therefore lift, between the advancing and retreating halves of the rotor by increasing the angle of attack of the retreating side. However, at



	DJI Phantom 3	UH-60 Black Hawk	XQ-139 Concept
Vertical cross-flow drag area:			
Representative cross-section:			
Equivalent flat-plate drag:			

**Fig. 1.38:** Vertical cross-flow drag comparison for rotorcraft with matched disk areas.

maximum forward flight speeds, the retreating blade angle of attack cannot be increased without stalling. This is the primary limiter of helicopter high-speed performance. Because the XQ-139 transitions to fixed-wing flight for high-speed flight, it can exceed the maximum velocities and cruise efficiency of existing rotorcraft. This ability also allows the XQ-139 to cruise and dash at higher speeds than other fixed-wing aircraft, due to a lack of takeoff/landing-based constraints on wing area. Unlike previous VTOL designs, however, the XQ-139 also has several advantages over existing rotorcraft in hovering flight and low-speed maneuvers.

While hovering, the XQ-139 has the potential to achieve a higher system-level figure of merit than either helicopters or standard multi-rotor aircraft, for a number of reasons. First, the XQ-139 design minimizes the download force that results from rotor-induced airflow passing vertically over the fuselage. In helicopters, this typically increases hover power requirements by about 5%.<sup>(60)</sup> Meanwhile, multi-rotor aircraft generally position the largest fuselage cross-sectional area between the rotors, reducing the vertical drag

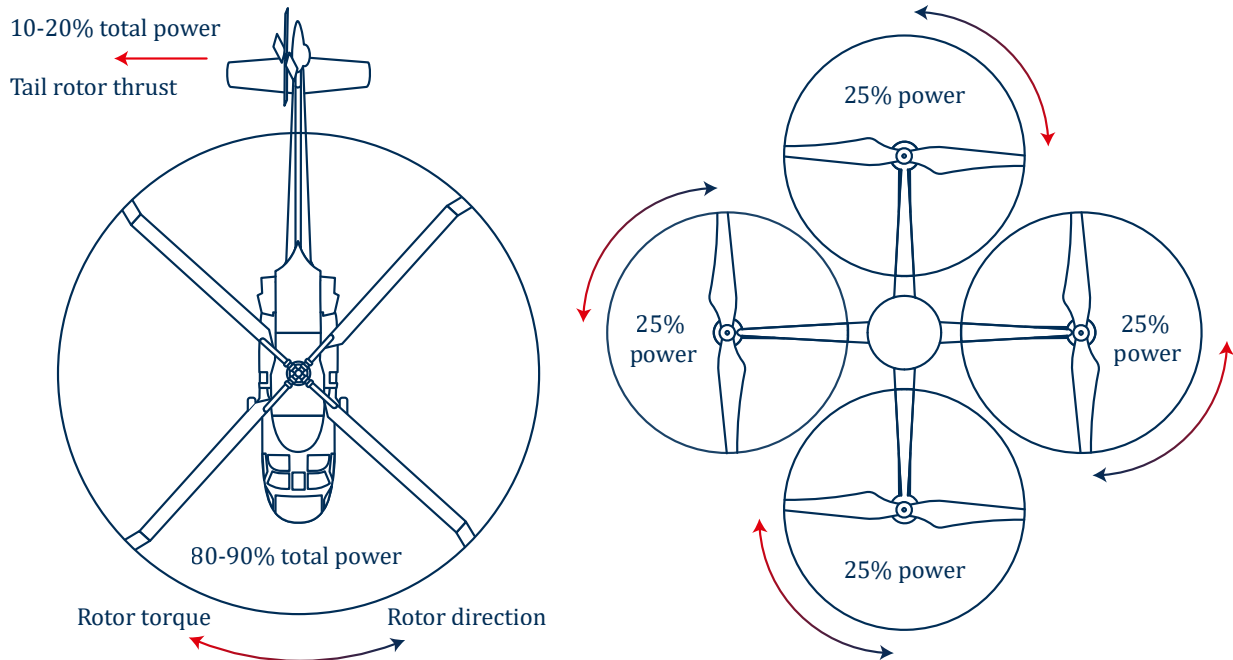


**Fig. 1.39:** Comparison of counter-torque strategy for helicopters and multi-rotor aircraft.<sup>(60)</sup>

over that region, but fail to streamline the arms onto which the rotor pivots are mounted. This results in drag force values that are one to two orders of magnitude higher than for streamlined airfoils of the same thickness.<sup>(61)</sup> Figure 1.38 shows a comparison of the typical planform views of a helicopter, quadcopter, and XQ-139-class aircraft, along with an estimate of the effects of vertical cross-flow drag on each aircraft. This is presented graphically as equivalent flat-plate drag area, which is the product of each cross-section's drag coefficient and the highlighted reference area. Current quadrotors especially could be better-designed with aerodynamics in mind, but they would still experience other limitations that the XQ-139 does not.

A second advantage that the XQ-139 holds over conventional helicopters with regards to hover efficiency is its lack of a tail rotor. Multi-rotor aircraft are able to counter the torque of each of their rotors by precisely matching each rotor's torque with that of a counter-rotating complement (Figure 1.39). In this way, the balanced thrust of every rotor is applied directly toward the task of providing lift or thrust for horizontal motion.

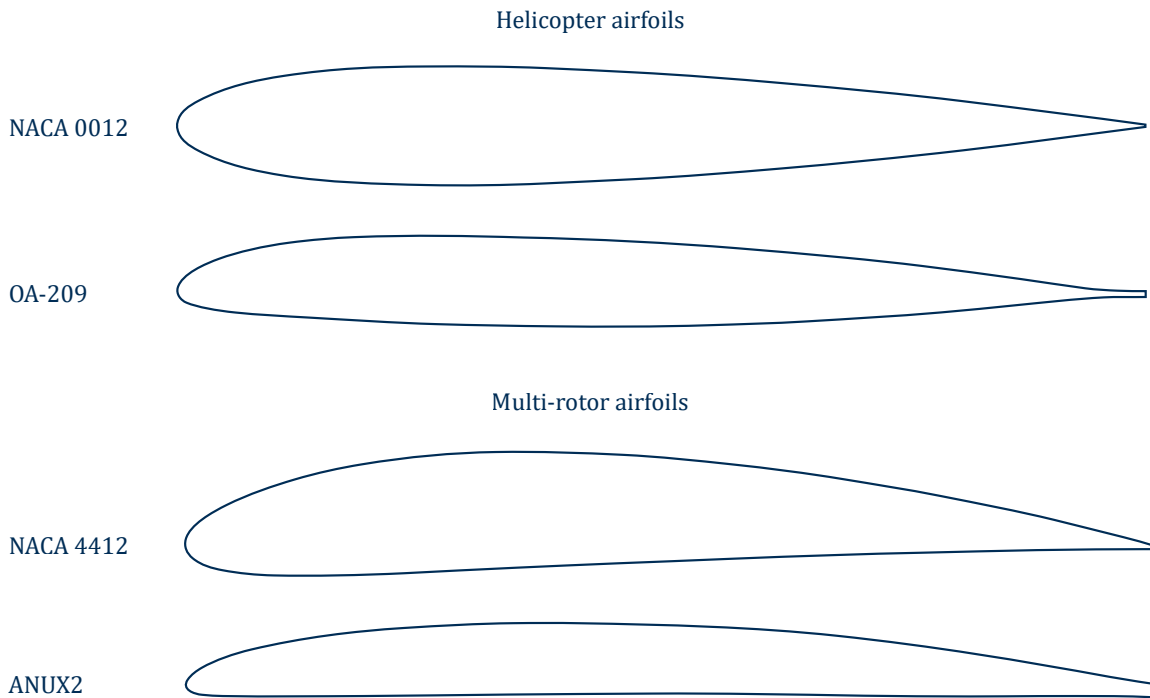


**Fig. 1.40:** Helicopter and multi-rotor airfoil sections.<sup>(60)(62)(63)</sup>

Conversely, a helicopter must direct 10-20% of its power to its tail rotor,<sup>(60)</sup> which is tasked primarily with countering the torque of the main rotor and also with yaw control, but serves no supportive or propulsive function.

Multi-rotor aircraft can also take advantage of high-performance airfoils that helicopters cannot.<sup>(63)</sup> Helicopter rotors are limited to airfoil sections that minimize the pitching moment of each rotor blade, as large pitching moments present serious structural and control related challenges.<sup>(64)</sup> Unfortunately, the cambered high-efficiency airfoils used for aircraft wings exhibit unacceptable pitching-moment characteristics. While modern materials and design techniques have expanded and improved the performance of helicopter rotors, these rotors cannot match the theoretical performance of blades designed for multi-rotor use. This is because multi-rotor aircraft use shorter blades with fixed or collective-only pitch variability and are not subject to helicopter design constraints. They can be designed using airfoils with higher lift-to-drag ratios and maximum lift coefficient values than can helicopter rotors that require both collective and cyclic pitch control. Fur-



**Fig. 1.41:** Multi-rotor blade manufactured with near-ideal taper and twist.<sup>(63)</sup>



**Fig. 1.42:** Typical helicopter rotor blade.<sup>(65)</sup>

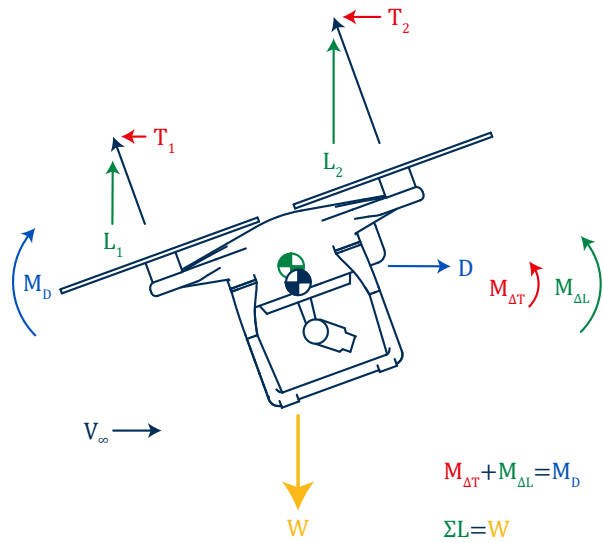
thermore, it is possible for multi-rotor blades to be designed with near-optimum taper and twist,<sup>(63)</sup> as given by Equations 1.2 and 1.3, where  $c(r)$  is the blade chord distribution with respect to the non-dimensionalized radius of the rotor  $r$ , and  $\theta(r)$  is the blade twist as a function of  $r$ .

$$c(r) = \frac{c_{tip}}{r} \quad (1.2)$$

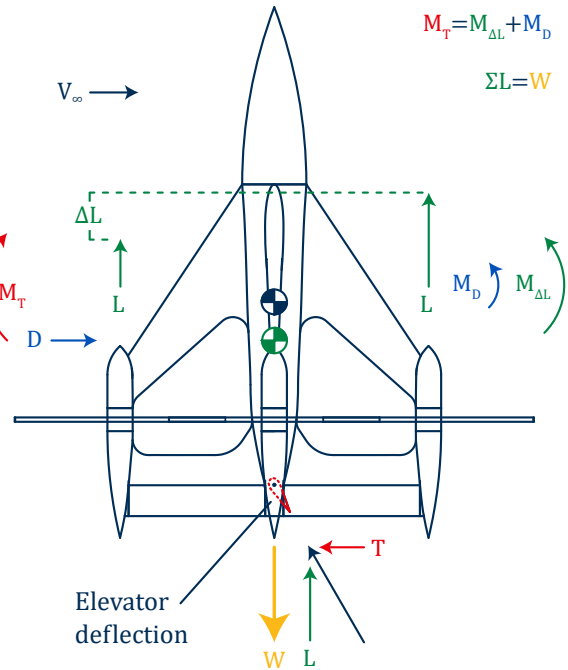
$$\theta(r) = \frac{\theta_{tip}}{r} \quad (1.3)$$

Figure 1.41 shows a multi-rotor blade that was manufactured to match these distributions, which are hyperbolic in nature. This contrasts with the typical helicopter rotor blade shown in Figure 1.42.

Finally, in non-electric XQ-139 variants, engine exhaust can be ejected directly into the center of the rotor wake to provide additional thrust and smooth the wake's transition to downstream conditions. This thrust increase raises the XQ-139's system-level figure of merit by as much as 5-10% for a turboprop engine.<sup>(66)</sup> Helicopters are unable



**Fig. 1.43:** Balance of forces and moments during standard multi-rotor translation.



**Fig. 1.44:** Balance of forces and moments during XQ-139 in-plane translation.

to make use of engine exhaust in this way, instead dissipating the remaining thrust using divergent ducting.<sup>(67)</sup>

In low-speed flight and hover conditions, the XQ-139 exhibits the ability to translate horizontally without the secondary rotations required by other rotorcraft. Not only does this feature provide a stable platform for surveillance, gunnery, or other mission-specific tasks, but it is particularly advantageous when maneuvering near walls and other obstacles. In those situations, tilting the aircraft while redirecting thrust for horizontal motion can cause recirculation zones, leading to loss of lift and collisions with the ground or other environmental features. The XQ-139 is able to decouple horizontal translation from rotational motion by combining variable rotor thrust with empennage control, as shown in Figure 1.44. To achieve in-plane translation, the elevator is used to direct rotor thrust at an angle, while the thrust of the fore and aft rotors (with respect to the direction of motion) are varied to counter the pitching moment generated by elevator deflection and provide the lift required to maintain flight altitude.

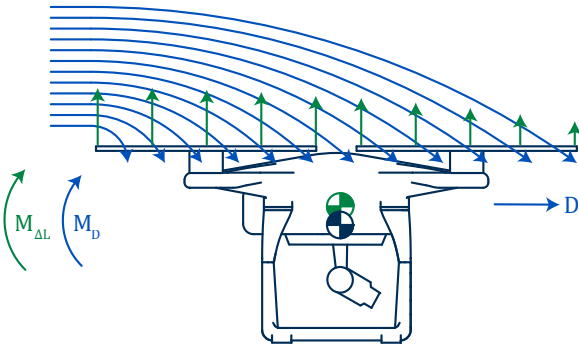


**Fig. 1.45:** Typical quadrotor gust response.

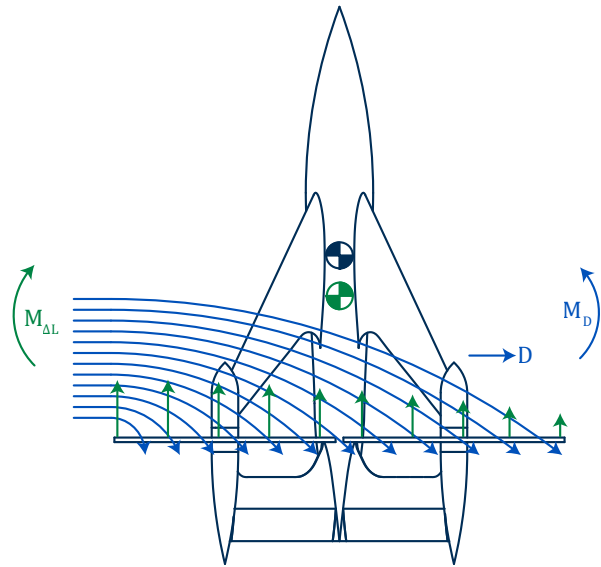


**Fig. 1.46:** XQ-139 gust response.

During forward flight, rotorcraft tend to develop a nose-up pitching moment as a result of the “transverse flow effect”.<sup>(68)</sup> This occurs because the air entering the rear of the rotor has a downward vertical component that decreases the angle of attack seen by the rotor blades (and therefore lift) leading to an unbalanced lift distribution that tends to destabilize the aircraft. Helicopters experience this effect differently due to their use of cyclic control, flapping blades, and tailplanes,<sup>(69)</sup> but fixed-pitch multi-rotor aircraft are particularly susceptible to this pitch-up effect at higher speeds where thrust variation is not an effective control strategy. A bigger concern, however, is the same pitch-up motion in response to wind gusts, which arise suddenly. Figure 1.45 demonstrates how the moments due to drag and nonuniform lift lead to pitch instability during gusty conditions. While the XQ-139’s rotors experience this effect as well, the aircraft’s aerodynamic center is located below its center of mass, causing it to pitch into the freestream – a stabilizing, rather than destabilizing, effect. This response is shown in Figure 1.46.

In summary, helicopters are currently the most successful option for missions requiring VTOL and hover performance, but the proposed configuration of the XQ-139 has the capacity to outperform helicopters in terms of hover performance, low-speed maneuverability, and cruise speed and efficiency.

## 1.2.2 Applications

The capabilities of the XQ-139 are relevant to a number of civilian applications, including remote sensing and ranged inspection. The design would be particularly suited to military uses, however, especially functioning as part of close air support (CAS) or close combat attack (CCA) operations.

During close air support, aircraft use their speed, range, and agility to aid ground units in a tactical capacity by detecting, attacking, and suppressing enemy threats.<sup>(70)</sup> CAS activities are directed by forward air control, which is tasked with coordination of CAS to increase the likelihood of mission success and limit the potential consequences of friendly or civilian deaths. CCA operations are similar, but aircraft are instead used as a primary weapon to attack enemy forces, rather than in a support role, and aircrews are responsible for their own fire.<sup>(71)</sup> Both CAS and CCA necessitate careful planning, communication, and execution to safely and effectively accomplish mission goals.

Unmanned XQ-139 variants could be used for a variety of CAS and CCA roles. Large armed aircraft could be purposed for attack, escort, and penetration missions, while smaller UAVS could be deployed directly by ground troops as organic air vehicles (OAVs) to provide immediate support in the form of surveillance/target designation, diversion, or suppressive fire.

In 2003, the U.S. Army Future Combat Systems (FCS) program set out to accelerate the integration of UAVs into Army operations. FCS defined four categories of unarmed OAVs, as shown in Table 1.1.<sup>(72)</sup> Each aircraft class was intended to provide surveillance, sensing, and targeting operational support at varying hierarchical levels, with characteristics meant to match each role.

**Table 1.1:** Future Combat Systems Proposed UAV Classes.

<b>Class</b>	<b>I</b>	<b>II</b>	<b>III</b>	<b>IV</b>
<b>Unit Size</b>	Platoon	Company	Battalion	Brigade
<b>Vehicle Mass</b>	5 to 10 lb	100 to 150 lb	300 to 500 lb	>3,000 lb
<b>Endurance</b>	50 minutes	2 hours	6 hours	24 hours
<b>Mission Radius</b>	8 km	16 km	40 km	75 km
<b>Transport</b>	1 Soldier	2 Soldier	2 Man Lift	Vehicle

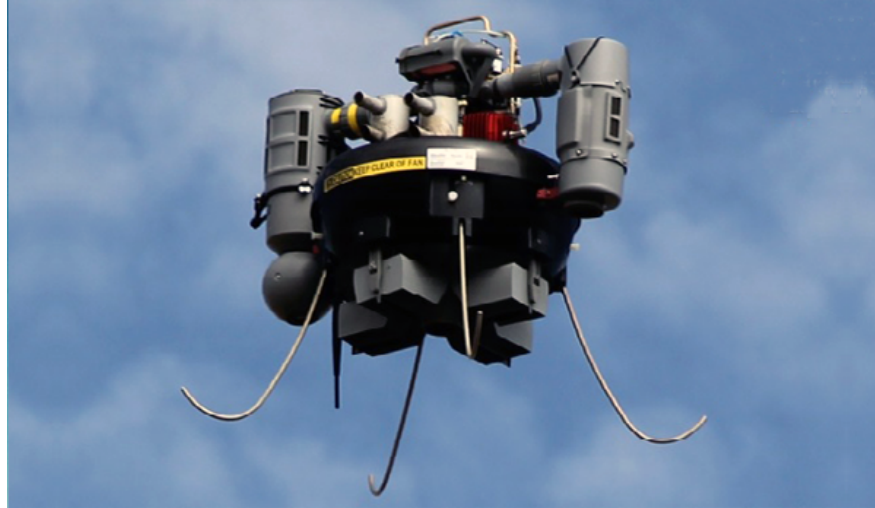


**Fig. 1.47:** Honeywell RQ-16a T-Hawk FCS Class I OAV.<sup>(73)</sup>

The FCS program aimed to award a manufacturing contract for one aircraft in each UAV class, but was dissolved in 2009 before final contracts were awarded. Only the Class I Honeywell RQ-16 T-Hawk (Figure 1.47) outlived the program. Still, the FCS model provides some guidance regarding the implementation of OAVs into military practices.

The remainder of this paper will explore the potential fit for the XQ-139 configuration into the U.S. military UAV framework. Chapter 2 discusses the theory and performance bounds related to the aircraft's design. The focus then shifts to the design, construction, and testing of a first-generation prototype of a Class I XQ-139 OAV, intended to perform CAS duties in close combat scenarios and demonstrate the capabilities of of the XQ-139 aircraft family.



*What can you conceive more silly and extravagant than to suppose a man racking his brains and studying night and day how to fly?*

— William Law, 1728<sup>(74)</sup>

## 2 THEORY AND PERFORMANCE BOUNDS

### Contents

---

<b>2.1 Configuration</b>	<b>25</b>
<b>2.2 Propulsion</b>	<b>27</b>
2.2.1 Battery-Electric Propulsion	27
2.2.2 Rotary Engine Propulsion	34
2.2.3 Turboshaft and Turboprop Propulsion	39
2.2.4 Hybrid-electric Propulsion	41
2.2.5 Rotor Performance Modeling	43
<b>2.3 Aerodynamics</b>	<b>49</b>
<b>2.4 Structures and Weights</b>	<b>53</b>
<b>2.5 Transition Strategy</b>	<b>55</b>
<b>2.6 Performance</b>	<b>57</b>

---

### 2.1 Configuration

The basic XQ-139 configuration was described in Section 1.2.1. Within the concept, however, there are a number of parameters that can be varied that affect the performance and role of the aircraft. Most of these features are aerodynamic, including wing sweep, taper, and separation angle, and are discussed in Section 2.3. Rotor overlap and variations in rotor size and system static margin are other notable factors that can produce alternative configurations, such as those shown in Figure 2.1. For the purposes of this study, aircraft were modeled with a wing separation angle of  $90^\circ$  and zero rotor overlap. These choices allow for analysis in both the x and plus orientation, simplify rotor performance modeling, and minimize the aircraft’s maximum footprint dimensions. Figure 2.2 shows a comparison of the takeoff/landing footprint of the standard XQ-139 variant versus those

of the Bell Boeing V-22 Osprey and the Sikorsky UH-60 Black Hawk helicopter, assuming matched rotor disk areas.

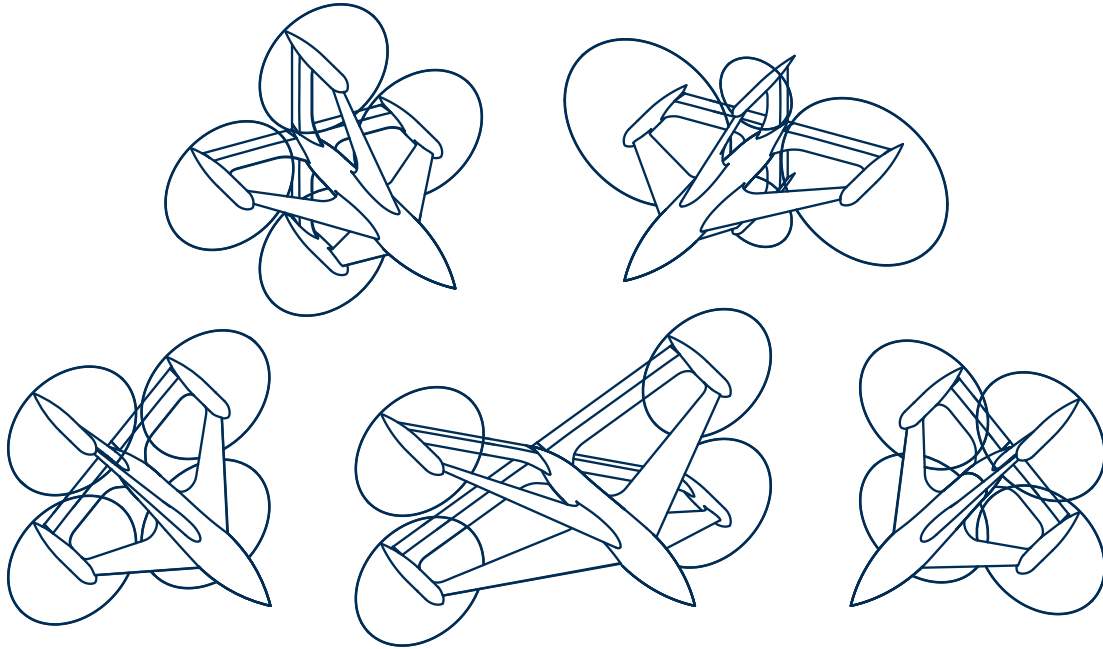


**Fig. 2.1:** XQ-139 configuration variants.

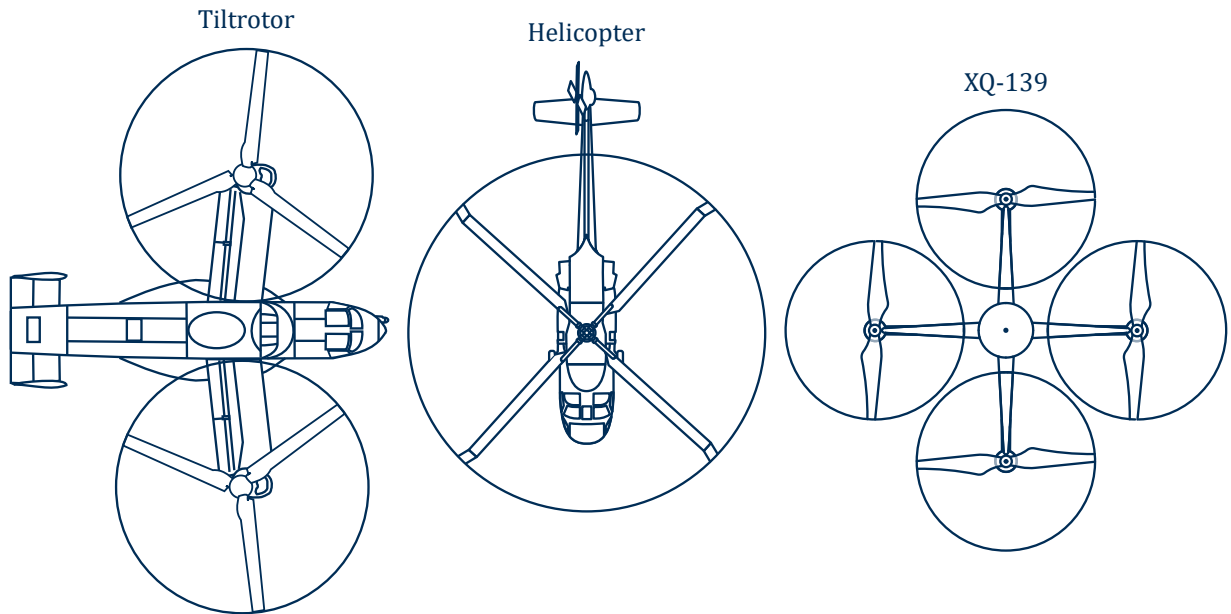


**Fig. 2.2:** Takeoff and landing footprint of representative VTOL aircraft for matched disk areas.

## 2.2 Propulsion

Four propulsion strategies were evaluated as part of this study: battery-electric, hybrid-electric, rotary engine, and turboshaft/turboprop engines. Each type of powerplant has advantages and disadvantages, and each occupies its own spot within the design space. Rotor performance was modeled using blade element momentum theory (BEMT), which is described in Section 2.2.5.

### 2.2.1 Battery-Electric Propulsion

Battery-electric aircraft are feasible at small scales, where internal combustion engines are unreliable, inefficient, and difficult to control. Electric motors offer high specific power, scalability, and efficiency and also produce low levels of heat, noise, and vibration. Figures 2.3 through Figure 2.6 demonstrate some of these advantages when compared to other propulsive options, based on data in Appendix B.<sup>(52, 75–87)</sup>

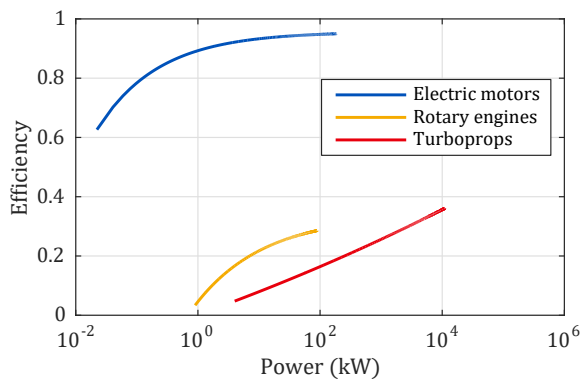


**Fig. 2.3:** Powerplant efficiency vs. rated power.

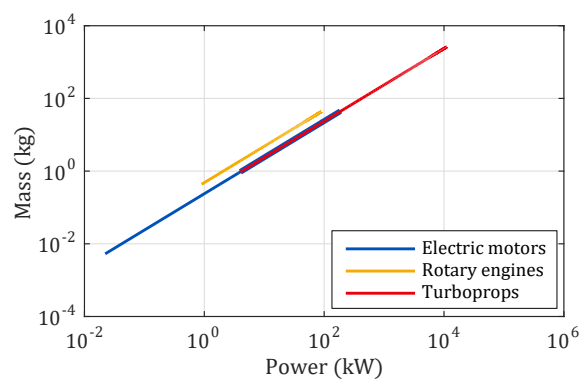


**Fig. 2.4:** Powerplant mass vs. rated power.

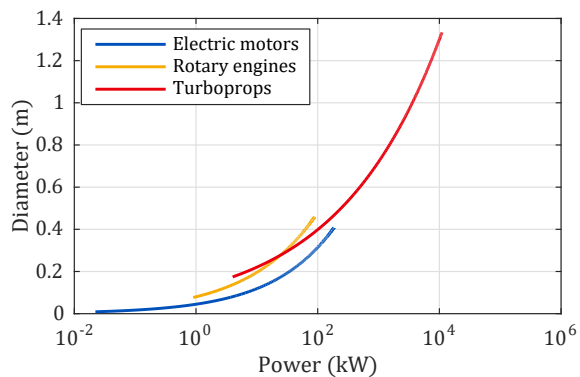


**Fig. 2.5:** Powerplant diameter vs. rated power.

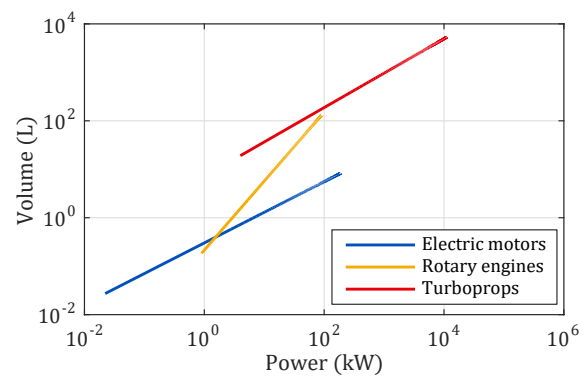


**Fig. 2.6:** Powerplant volume vs. rated power.

It can be seen that for a given power rating, high-performance electric motors are lighter, more compact, and more efficient than rotary or gas-turbine engines. Furthermore, they are simpler and more affordable than either engine type.

While electric motors compare favorably with other powerplants, the major shortcoming of battery-electric power for aircraft (and other vehicles) is the low specific energy of batteries when compared to hydrocarbons such as gasoline or diesel fuel. Gasoline and jet fuel have specific energies of roughly 12,000 Wh/kg,<sup>(88)</sup> whereas current lithium-ion batteries top out somewhere between 100 and 200 Wh/kg.<sup>(89)</sup> This number is reduced even further when the cells are incorporated into a vehicle battery pack, especially for larger vehicles where cooling, control, and safety components are required.

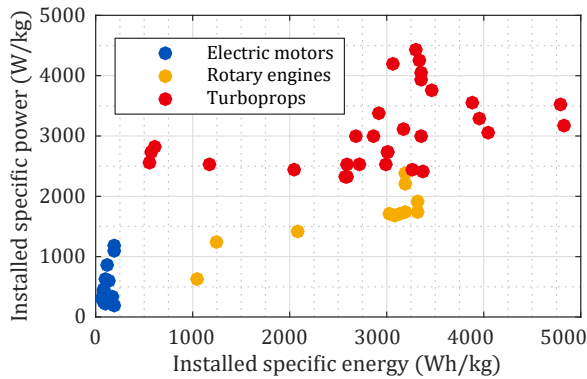


**Fig. 2.7:** Installed specific properties for considered propulsion systems.<sup>(52, 75–87, 90, 91)</sup>

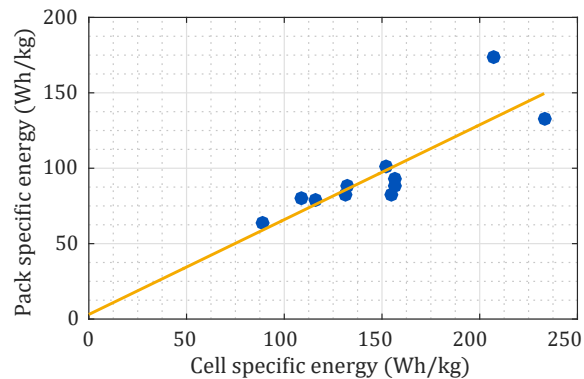


**Fig. 2.8:** Pack vs. cell-level specific energy relationship for mass estimates.<sup>(90, 91)</sup>

Figure 2.7 and Figure 2.8 illustrate the effects of installation on powerplant and battery specific properties. Figure 2.8 is based on pack and cell-level mass and energy content for consumer electric vehicles, as well as current manned electric aircraft. The linear fit shown in the figure suggests that a fully integrated battery pack typically weighs about fifty percent more than indicated by cell properties alone. The curve and data can be used for pack mass estimates during the preliminary design process for electric vehicles.

Even the specific power advantage of electric motors is offset by the fact that motors cannot produce any amount of power without a battery pack or generator that can supply the required electrical input. This leads to installed specific power values that are significantly lower than motor-only trends indicate. Even after accounting for the inefficiencies



**Fig. 2.9:** Airbus E-Fan.<sup>(92)</sup>



**Fig. 2.10:** Joby Aviation S2 concept.<sup>(93)</sup>

inherent in internal combustion engine (ICE) operations, roughly 15 to 30 times the mass is required to store an equivalent amount of energy using batteries rather than liquid fuel. This extra mass has significant implications for aircraft performance, where weight is a driving factor. Still, the efficiency and per-unit cost effectiveness of electric power mean that the benefits of electric propulsion often outweigh its drawbacks for small unmanned aircraft, and the technology is even being evaluated for larger aircraft with specialized applications, like the Airbus E-Fan (Figure 2.9) and Joby Aviation S2 (Figure 2.10).

### Electric Motors

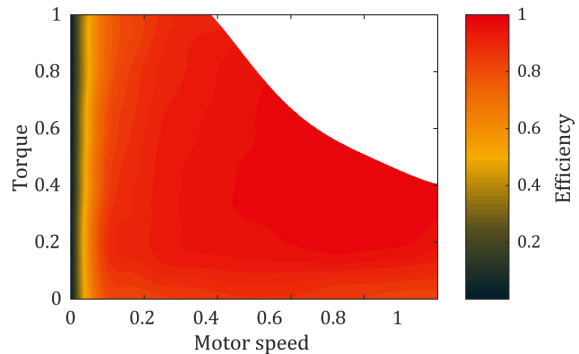
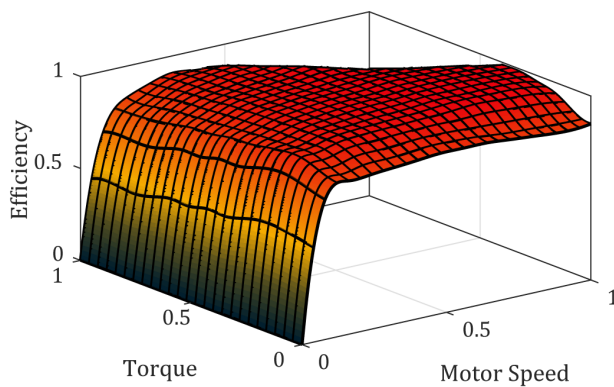


**Fig. 2.11:** 3D normalized motor efficiency map. **Fig. 2.12:** 2D normalized motor efficiency map.

There are several types of electric motors, including brushed and unbrushed direct current (DC) motors, alternating current (AC) inductive motors, and AC permanent magnet motors. Brushless DC and AC permanent magnet motors offer the highest specific

power, efficiency, and power density of all motor types, making them suitable for aerial applications. For smaller aircraft, brushless DC motors are the standard choice. This is due to the low cost of their controllers versus those of AC motors. At larger scales, the minor gains in efficiency due to a switch to AC motors is enough to offset the cost of the more expensive controllers required for their use.

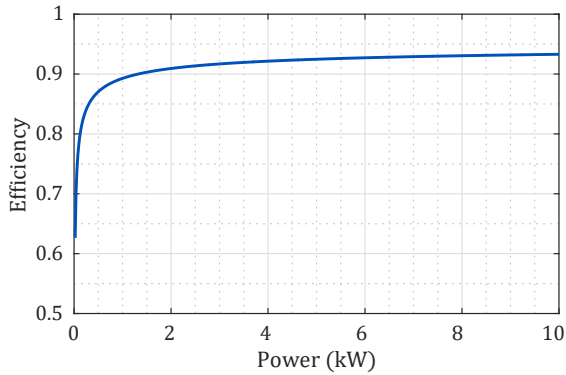


**Fig. 2.13:** Motor efficiency vs. rated power.<sup>(94)</sup>

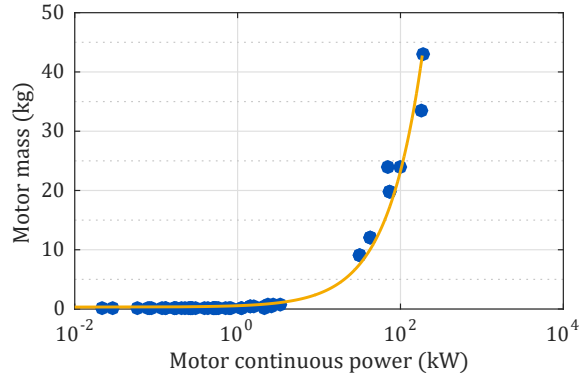


**Fig. 2.14:** Motor mass vs. rated power.

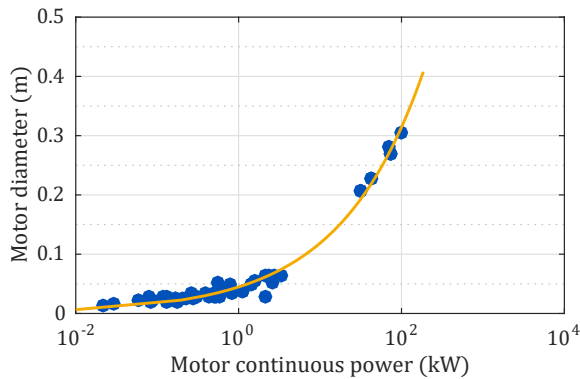


**Fig. 2.15:** Motor diameter vs. rated power.

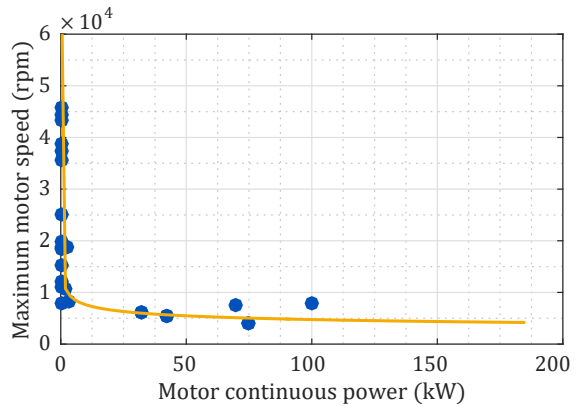


**Fig. 2.16:** Peak motor speed vs. rated power.

For sizing purposes, a representative efficiency map for a brushless direct current motor (BLDC) was constructed based on example specifications provided by BLDC motor manufacturers.<sup>(95)</sup> The peak efficiency was scaled using Equation 2.1 – an empirical expression reported in Reference (94) – and torque and motor speed trends were derived from motor data in Appendix B. Figure 2.11 and Figure 2.12 show the unscaled map when plotted in two and three dimensions. A MATLAB optimizer was used to select operating

points across a range of aircraft installed powers, and motor torque and speed outputs were matched with the corresponding requirements, as determined by the rotor performance module. Figures 2.13 through Figure 2.16 present motor performance and geometric scaling trends used in the model.

Each of the curves plotted in Figures 2.13–2.16 was used during aircraft sizing and performance studies, using Equation 2.1–Equation 2.4, where  $P$  is the maximum continuous power requirement, and the motor efficiency  $\eta$ , mass  $m$ , diameter  $D$ , and motor speed  $RPM$  are dependent variables.

$$\eta = 0.957 - 0.0638P^{-0.432} \quad (2.1) \qquad m = 0.232P \quad (2.2)$$

$$D = 0.0459P^{0.402} \quad (2.3) \qquad RPM = 12201P^{-0.205} \quad (2.4)$$

## Batteries

Lithium-ion batteries (a broad family composed of different chemistries) are the most prevalent batteries used for electrically-powered aerial vehicles. The reasons for this can be clearly seen from Figure 2.17, which plots the peak specific energy and power for a range of battery chemistries.<sup>(96–111)</sup>

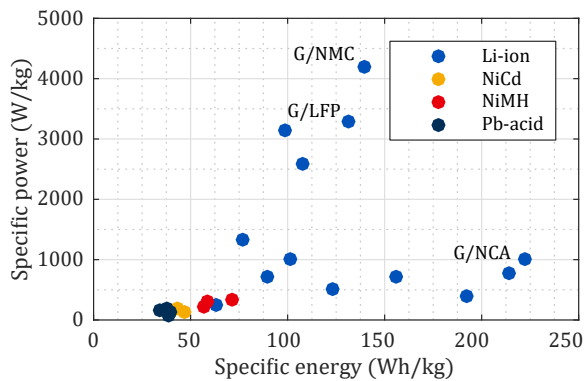


**Fig. 2.17:** Battery specific properties.

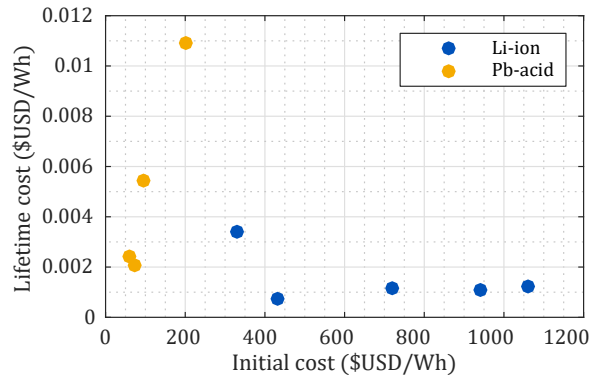


**Fig. 2.18:** Lifetime vs. initial battery costs.

Figure 2.18 compares the lifetime and initial costs for a set of lithium-ion batteries with those of lead-acid batteries, which represent the most affordable rechargeable battery chemistry. While lead-acid batteries would not be chosen to power an aircraft due to their

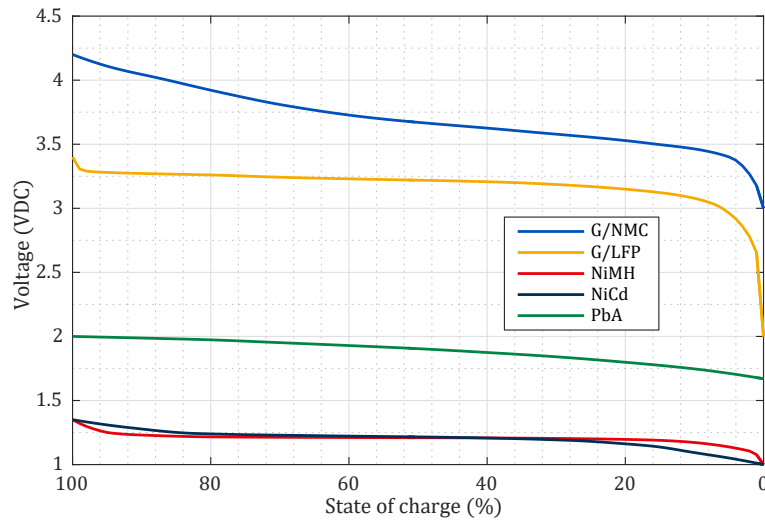


**Fig. 2.19:** Discharge curves for various battery chemistries.

poor specific properties, it can be seen that even the apparent cost advantage of lead-acid batteries vanishes when considered on a per-cycle basis.

Other advantages of lithium-ion batteries include their ability to maintain a relatively flat voltage discharge curve across a range of discharge current loads and their high cell voltage when compared to other battery types. Figure 2.19 shows example discharge profiles for a pair of lithium-ion chemistries, as well as representative discharge curves for lead-acid, NiCd, and NiMH batteries.

Despite their considerable advantages, lithium-ion batteries are not without drawbacks. They have a high unit cost and require specialized controllers to ensure safety and battery performance. They are also much more difficult to recycle than many other cell types. This is due to the wide range of chemistries and components used to manufacture lithium-ion cells. A subset of cells from within this range was evaluated as part of the model; their characteristics are listed in Table 2.1.

Because of the high-power requirements associated with hovering flight, the lithium iron phosphate (LFP) batteries from A123 and Kokam's lithium-nickel-manganese-cobalt oxide (NMC) batteries were the obvious choices for larger scale iterations of the XQ-139. The Kokam batteries offer the best specific properties and cycle life of any of the listed cells and, as a result, were used as the basis for the analysis of electric and hybrid XQ-139



**Table 2.1:** Current-market lithium-ion batteries and specific properties.<sup>(96–104)</sup>

Maker	Chemistry	Spec. Power (W/kg)	Spec. Energy (Wh/kg)	Energy Density (Wh/l)	Cycle Life
A123	G/LFP	3300	131	247	5,000
Altairnano	LTO/NCO	1333	77	168	16,000
Kokam	G/NMC	4200	140	258	7000
Kokam	G/NMC	385	192	408	2,000
Leclanche	LTO/NCO	250	63	145	15,000
Leclanche	G/NMC	730	156	337	4,500
Panasonic	G/NCA	774	214	577	500
Phostech	G/LFP	3150	99	189	4000
Toshiba	LTO/NMC	720	90	177	10,000
Valence	G/LFMP	1010	101	227	4,500

variants. Manufacturer information was incorporated into a MATLAB battery module to calculate the battery’s instantaneous power output and state of charge (SOC).

The model prescribed a shaped discharge curve to approximate NMC discharge characteristics, and accounted for load-specific effects, including the phenomena of capacity offset and voltage depression. Together, these effects alter the level of power that is immediately available for propulsion, and limit the total amount of energy that can be delivered by the battery pack to the rotors. Both effects are amplified at high discharge C-rates, a measure of current normalized versus the battery’s charge capacity in amp-hours.

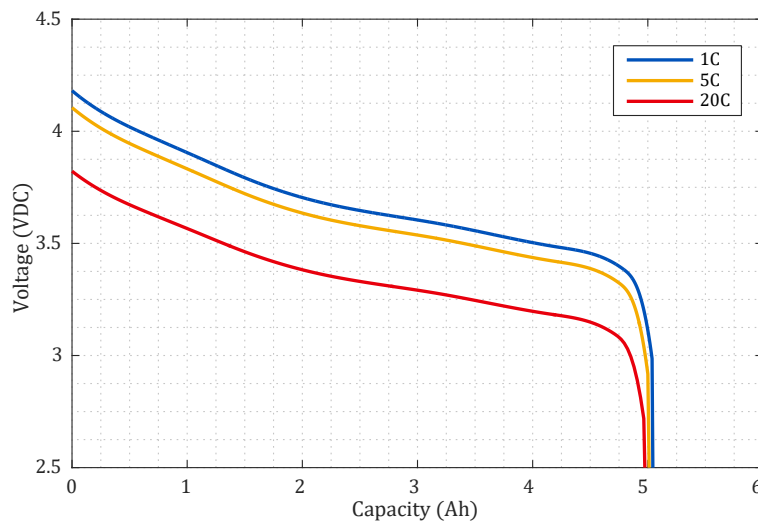


**Fig. 2.20:** G/NMC discharge curves for battery model.

Cell properties were input into the model, and coefficients were estimated for Equation 2.5, which simulates the effective current draw and instantaneous capacity offset of a battery as a function of actual output current and operating temperature.<sup>(112)</sup> Input values are nondimensionalized with respect to a reference current ( $I_{ref}$ ) of 1 A and a reference temperature ( $T_{ref}$ ) of 298 K, and the constants  $\gamma$ ,  $\chi$ , and  $\delta$  are determined experimentally.

$$\Delta C = \gamma \left( \frac{I_t}{I_{ref}} \right)^\chi \left( \frac{T_{ref}}{T} \right)^\delta \quad (2.5)$$

Voltage depression was modeled using a linear approximation, and values for  $\gamma$ ,  $\chi$ , and  $\delta$  were incorporated into the MATLAB battery model to match the discharge curves provided by cell manufacturers. The model-output discharge curves are displayed in Figure 2.20, and show how both cell capacity and voltage are affected by the discharge C-rate.

### 2.2.2 Rotary Engine Propulsion



**Fig. 2.21:** CybAero Vantage UAV.<sup>(113)</sup>



**Fig. 2.22:** E-Go light sport aircraft.<sup>(114)</sup>

Rotary engines are another propulsive option for the XQ-139 configuration. While relatively uncommon on manned aircraft where piston and gas turbine engines have overriding advantages in terms of efficiency or power, rotary engines have been frequently applied to UAVs such as the RQ-7 Shadow (Figure 1.11) and the CybAero Vantage (Figure 2.21). They have also been used in small manned aircraft, like the E-Go microlight (Figure 2.22).

This is due primarily to the high specific power and compact form factor of rotary engines; their cylindrical shape makes them particularly well-suited for the XQ-139 design, where other engine types would bring increase the aircraft's weight, wetted area, and/or excrescence drag. Figure 2.23 compares rotary engine size to that of a similarly-powered piston engine.

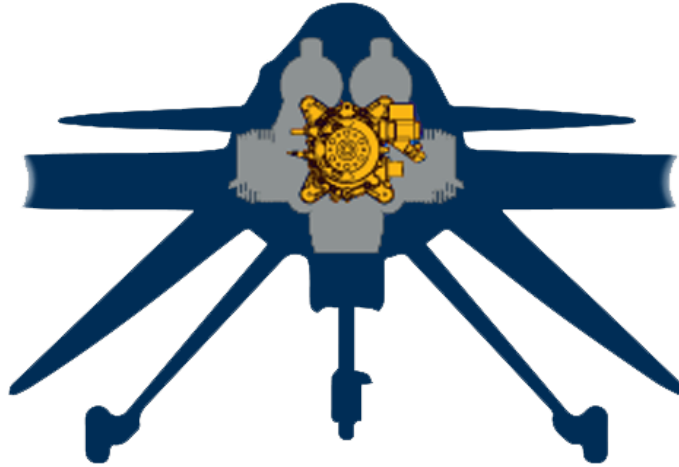


**Fig. 2.23:** Relative rotary and piston engine size comparison. <sup>(115)</sup>

As with electric motors in Section 2.2.1, manufacturer data (reported in Appendix B) were used to investigate rotary engine scaling trends. These results are presented in Figures 2.26–2.29, and Equations 2.6–2.9 describe the plotted trends with expressions similar to those in Section 2.2.1. The variables match those in Equations 2.1–Equation 2.4, with the exception of Equation 2.6, which predicts the specific fuel consumption (SFC) for scaled rotary engines.

Figure 2.24 and Figure 2.25 display the SFC map used in the performance model. It can be seen that the shape of the 3D surface plot in Figure 2.24 is different than that of the motor efficiency map in Figure 2.11. This is because specific fuel consumption is related inversely to energetic efficiency. It should also be noted that whereas efficiency varied most with speed for electric motors, torque requirements are associated with the greatest changes in rotary engine SFC.

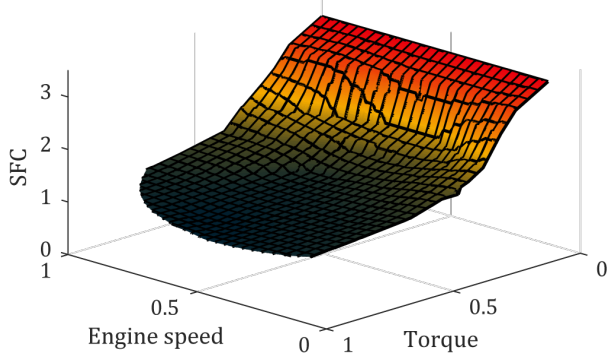


**Fig. 2.24:** Normalized rotary engine SFC map.

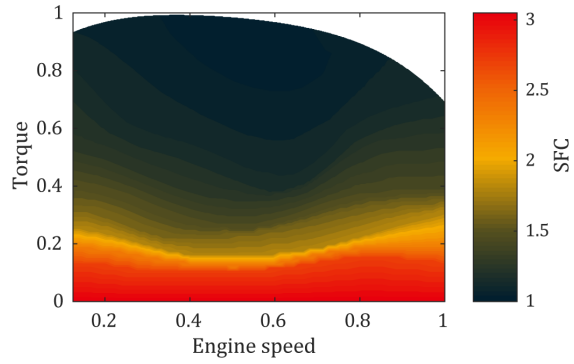


**Fig. 2.25:** Rotary engine SFC contours.

$$SFC = 0.890P^{-0.941} + 0.296 \quad (2.6)$$

$$m = 0.477P \quad (2.7)$$

$$D = 0.08P^{0.389} \quad (2.8)$$

$$RPM = 12660P^{-0.137} \quad (2.9)$$

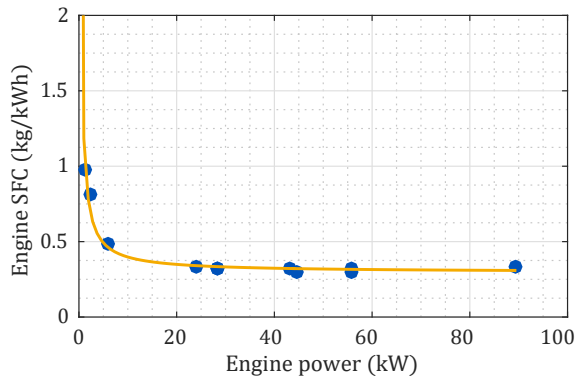


**Fig. 2.26:** Rotary engine SFC vs. rated power.

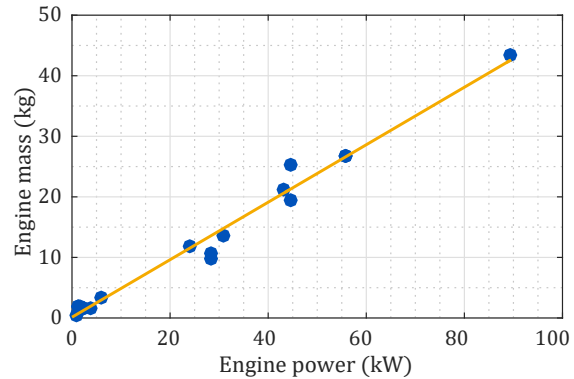


**Fig. 2.27:** Rotary engine mass vs. rated power.

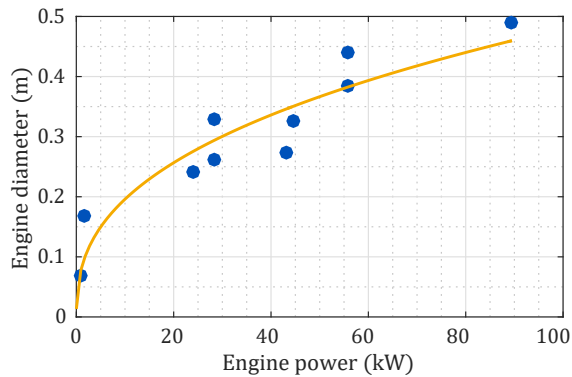


**Fig. 2.28:** Engine diameter vs. rated power.

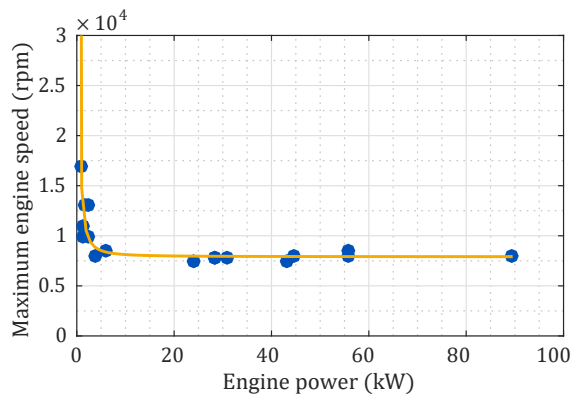


**Fig. 2.29:** Peak engine speed vs. rated power.

A critical difference between electric motors and fuel-burning engines is that while motor performance is independent of altitude, engine performance is not. For naturally aspirated engines, power output depends on the density and mixture ratio of the fuel-air combination. Each of these variables is at least partially dependent on intake atmospheric properties, which vary with altitude. Equation 2.10<sup>(116)</sup> approximates the impact of altitude and air density  $\rho$  on the power output  $P_{alt}$  of a naturally aspirated engine, using sea level as the reference elevation.

$$P_{alt} = P_{SL} \left[ 1.132 \left( \frac{\rho}{\rho_{ref}} \right) - 0.132 \right] \quad (2.10)$$

To improve engine performance at altitude, the pressure and density of air moving through the engine can be artificially increased using forced induction devices such as turbochargers and superchargers. The two can also be combined for the same purpose.

When evaluating rotary engines for this study, engine performance at altitude was assumed to be normalized to sea level conditions via use of a supercharger. Above a certain critical altitude  $h_{crit}$ , taken to be 5000 meters,<sup>(116, 117)</sup> engine performance was allowed drop off in accordance with Equation 2.10 using the air density at an altitude  $(h - h_{crit})$  rather than at the true altitude  $h$ .

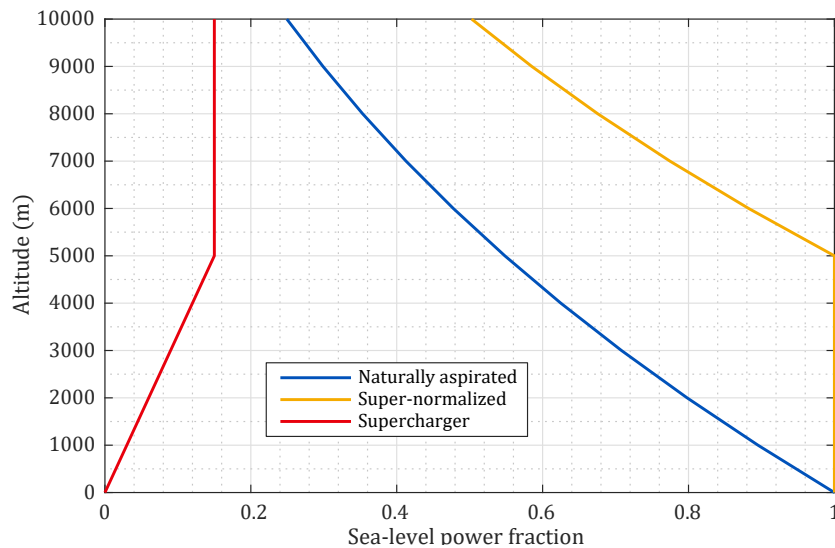


**Fig. 2.30:** Altitude effects on engine output power and supercharger power consumption.

A linear approximation was used to estimate the additional power fraction required to drive the supercharger at altitudes greater than zero. This fraction ranged from zero at sea level to fifteen percent at and above the critical altitude.<sup>(117, 118)</sup> Figure 2.30 depicts the altitude-driven fractional approximation of engine power output and supercharger power consumption that was used in the model.

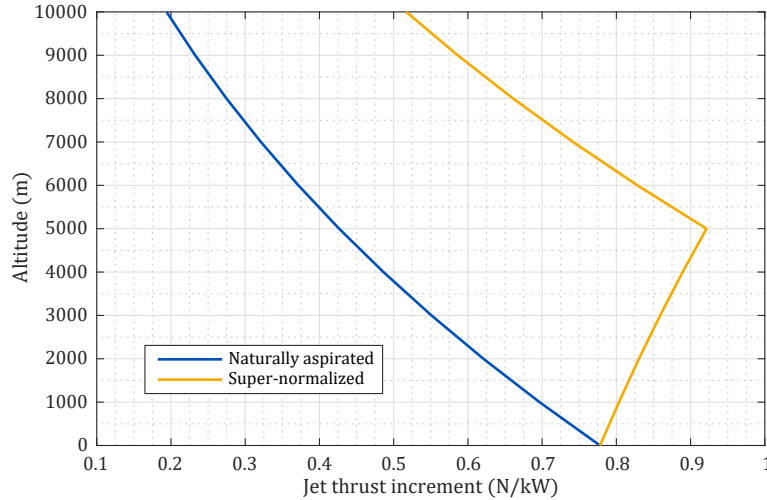


**Fig. 2.31:** Altitude effects on exhaust jet thrust increment.

As a final consideration for rotary engine propulsion, the additional thrust increment due to directed exhaust-jet expulsion was modeled using Equation 2.11, where the incremental thrust  $\Delta T_{jet}$  is given in newtons, based on power  $P$  in kilowatts.<sup>(119)</sup>  $\Delta T_{jet}$  depends on the ratio between the engine operating pressure  $p$  and the ambient atmospheric pressure  $p_{amb}$  and therefore varies with altitude.

$$\Delta T_{jet} = 0.778P \left( \frac{p_{amb}}{p} \right)^{-0.269} \quad (2.11)$$

The pressure ratio  $\frac{p_{amb}}{p}$  is approximately equal to one for naturally aspirated engines. When coupled with Equation 2.11, the thrust per unit power can be related to altitude, as shown in Figure 2.31. For a turbo/super-normalized engine,  $\frac{p_{amb}}{p}$  climbs until the critical altitude is reached. Then the jet-exhaust thrust increment decreases in the same fashion as the naturally aspirated case.

The concept of using the exhaust jet thrust to increase engine power output was evaluated most heavily during the 1940s,<sup>(119, 120)</sup> prior to the rise of the gas turbine engine, but the method is particularly germane to the design of the XQ-139, since its configuration provides a clear opportunity to improve hover performance using thrust generated by the exhaust stream.

### 2.2.3 Turboshaft and Turboprop Propulsion

Turboshaft engines, which use a gas turbine to generate shaft power, are used on many large-scale rotorcraft because of their high power-to-weight ratios. In this application, they differ from turboprop engines mainly in that instead of driving a propeller (via a reduction gearbox), they reorient the direction of torque application to drive the helicopter's rotor. Another functional difference is that while helicopter turboshaft engines vent excess exhaust pressure to the atmosphere, turboprops use an exhaust jet to augment the total thrust produced by the rotor/engine combination. This leads to an oft-reported equivalent power rating, typically given in terms of equivalent horsepower (ehp) or equivalent kilowatts (ekW).

The percentage of total thrust produced by this method is optimized during engine design to produce the desired performance. While plotting reported equivalent power versus shaft power for the set of turboprop engines listed in Appendix B.3 suggests a consistent ratio of roughly 1.06, this ratio varies with altitude and airspeed. At high Mach numbers, jet thrust can make up more than half of the total thrust. The ratio of jet thrust to total thrust was approximated using Equation 2.12, which was based on data from References (121)-(122), and a three-dimensional interpolant was used to model the variation in total thrust with respect to the same variables. As mentioned in Section 1.2, this equivalent power can be used to incrementally enhance the XQ-139's system-level hover performance.

$$\frac{T_{jet}}{T_{total}} = e^{(-5.722e-05)h+5.48(M-1)} \quad (2.12)$$

Since the horizontal and hovering flight modes for the XQ-139 can have significantly different power requirements, part-load curves for industrial gas turbines were used to estimate turboprop/turboshaft efficiency for variations in torque and engine speed. <sup>(partload)</sup> General scaling trends are presented in Figures 2.32- 2.35, and the corresponding fitted expressions are given as Equations 2.13- 2.16

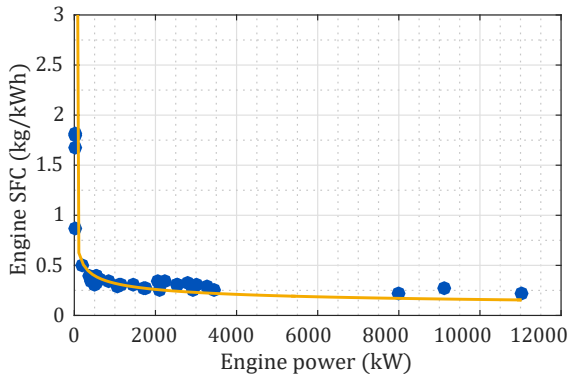


**Fig. 2.32:** Turboprop SFC vs. power.

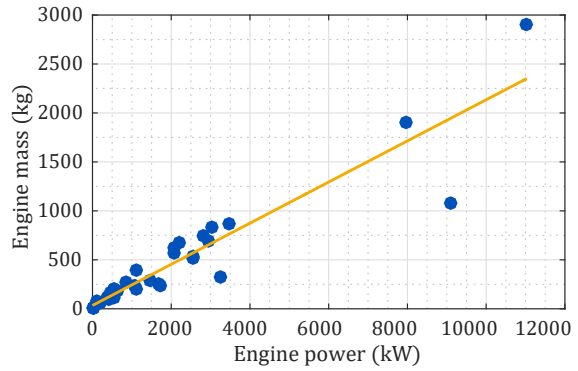


**Fig. 2.33:** Turboprop mass vs. power.

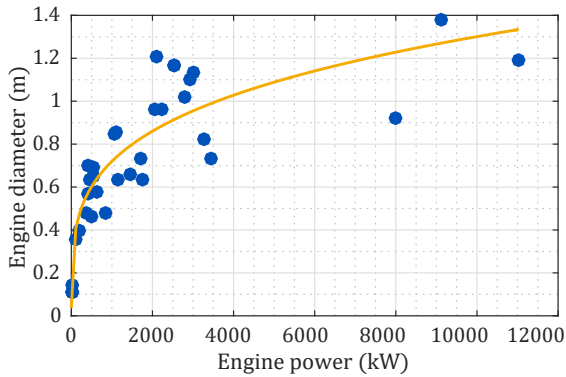


**Fig. 2.34:** Turboprop diameter vs. power.

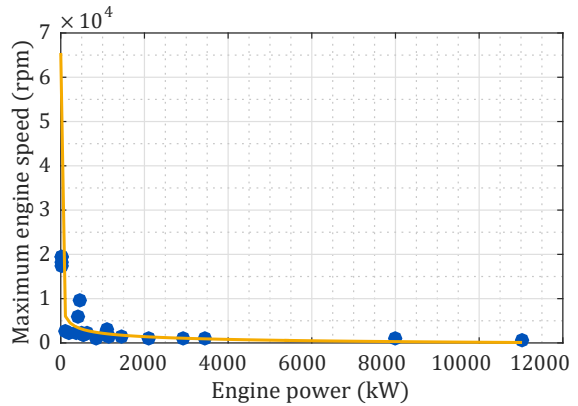


**Fig. 2.35:** Turboprop output speed vs. power.

$$SFC = 3.131P^{-0.458} + 0.186 \quad (2.13)$$

$$m = 0.217P \quad (2.14)$$

$$D = 0.122P^{0.257} \quad (2.15)$$

$$RPM = 35884P^{-0.428} \quad (2.16)$$





**Fig. 2.36:** NASA GL-10 prototype.<sup>(123)</sup>



**Fig. 2.37:** Horizon X3 hybrid concept.<sup>(124)</sup>

## 2.2.4 Hybrid-electric Propulsion

A number of recent aircraft concepts have explored hybrid propulsion, including NASA's GL-10 UAV prototype (Figure 2.36) and the X3 light sport aircraft, which is being developed by Horizon Aircraft (Figure 2.37).

Hybrid propulsion systems couple electric motors with internal combustion engine power in an attempt to capitalize on the advantages of each type of powerplant. Broadly, hybrid propulsion architectures can be categorized as series-hybrid and parallel-hybrid systems.

Series-hybrid vehicles are simple, using only electric motors for direct propulsion. As a result, the engine is used to charge the battery pack and power the motors while operating at its most efficient setpoint, opening the door for novel aircraft configurations based on distributed electric propulsion. Distributed electric propulsion, like that explored by NASA's battery-electric LeapTech concept (Figure 2.38), makes use of the largely scale-free performance of electric motors to induce airflow across an aircraft's span. This allows for reductions in total wing area and improves low-speed flight characteristics.

For series-hybrid automobiles, a battery pack is generally required to provide extra power during acceleration since typical operating power requirements are well below peak levels. However, battery packs sized using maximum power and longevity criteria can make up a significant fraction of a vehicle's mass. Series-hybrid vehicles typically require a larger generator and larger motors than parallel systems. This leads to a heavier system that has serious implications on vehicle performance, especially for aircraft.



**Fig. 2.38:** NASA LEAPTech concept.

The LightningStrike UAV concept from Aurora Flight Sciences eliminates the need for a battery pack by directly powering its electric ducted fans using a set of generators run by a turboshaft engine.<sup>(125)</sup> Since cruise power consumption is lower than the maximum power required during hovering operations and with no battery to provide the additional hover power, the engine must operate at a suboptimal setpoint during the cruise condition. Nonetheless, efficiency gains can still be made by maximizing the size of the engine, thereby minimizing its best SFC value.

Unlike series hybrids, parallel-hybrid systems can use either engine power or motor power (or a combination of the two) to meet propulsive requirements. In general, parallel-hybrid vehicles require a smaller battery pack and motor set than series-hybrid configurations and gain most of their efficiency by operating an engine that is smaller than peak loads would otherwise dictate. A specific advantage of a parallel arrangement, in the case of a multi-rotor aircraft such as the XQ-139, is the ability to use the high-torque and rapid response of electric motors for variable-speed and variable-torque maneuvers. These maneuvers would be more complex and limited in effectiveness for engine-only aircraft, especially at larger scales where torque requirements would be significant.

In the case of the XQ-139 aircraft family, it is anticipated that there exists a range of aircraft sizes where hybrid-propulsion (particularly the series architecture) enables per-

formance that exceeds that of battery-electric aircraft and where the sole use of internal combustion engines is unduly complex or inefficient.

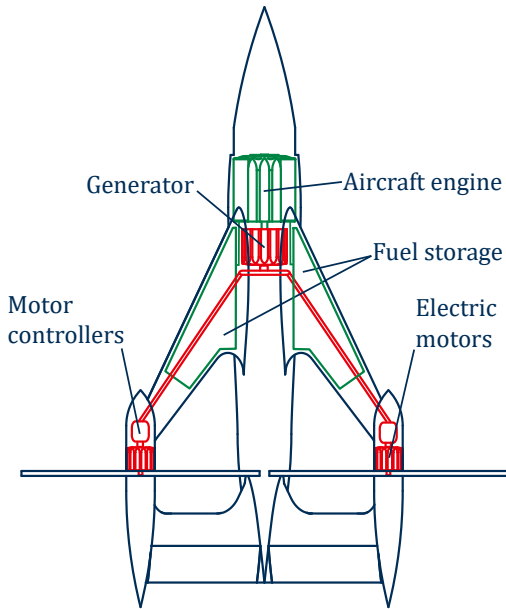


**Fig. 2.39:** Series hybrid architecture.

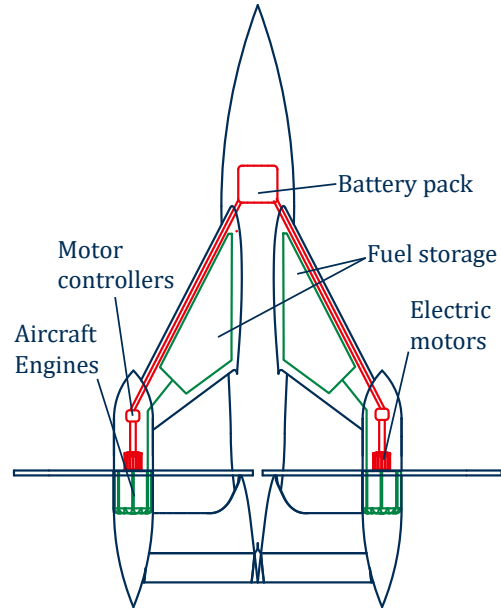


**Fig. 2.40:** Parallel hybrid architecture.

Series and parallel hybrid systems using both rotary and turboshaft engines were evaluated as part of the XQ-139 design space. For sizing purposes, the series design was conceived as an engine and generator pair capable of providing a set of four motors with a constant output power matching peak requirements. The hybrid arrangement was envisioned as a set of four engines sized for hover, with four motors sized to provide the remaining power margin for transition and peak power operations. Representations of each these configurations are shown in Figure 2.39 and Figure 2.40.

### 2.2.5 Rotor Performance Modeling

Rotor performance was predicted using a combined blade element-momentum theory MATLAB module. The module was used to size the rotor and assign blade geometry, as well as to determine rotor power and collective pitch requirements for a given thrust output and airspeed.

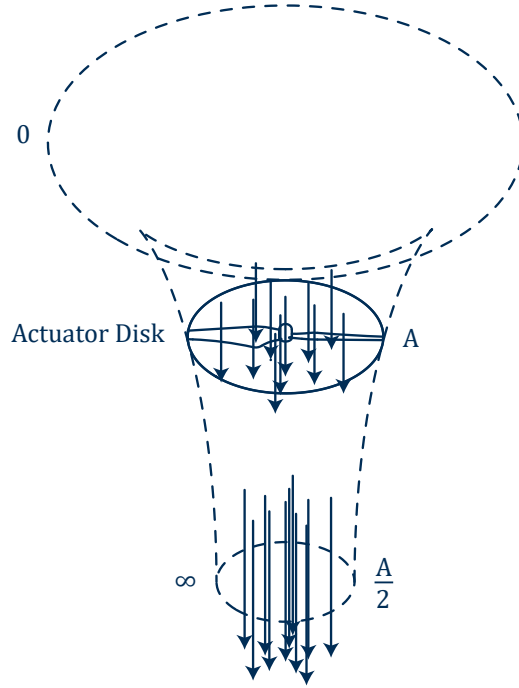


**Fig. 2.41:** Control volume for ideal rotor momentum theory.

Momentum theory describes the ideal performance of a propeller or helicopter rotor when treated as an infinitely thin “actuator disk”. In the ideal state, a constant velocity airflow is induced through the disk area, as shown in Figure 2.41. At far-wake conditions, the rotor slipstream contracts to half of the rotor disk area to accommodate the increased velocity of the airflow under mass conservation assumptions. Enforcement of mass, energy, and momentum conservation laws leads to Equation 2.17, which describes the rotor’s induced velocity in terms of the rotor thrust  $T$ , the density of air  $\rho$ , and  $A$ , the area of the rotor actuator disk. Multiplying this expression by the rotor’s output thrust, the rotor’s ideal power requirement can be found using Equation 2.18.

$$v_i = \sqrt{\frac{T}{2\rho A}} \quad (2.17)$$

$$P_{req} = \frac{T^{3/2}}{\sqrt{2\rho A}} \quad (2.18)$$

Blade element theory represents the blades of a rotor as collections of independent 2D airfoil sections whose aerodynamic forces can be determined from the local flow con-

ditions defined in Figure 2.42. Total rotor moments and forces are calculated by the spanwise integration of blade elemental values.

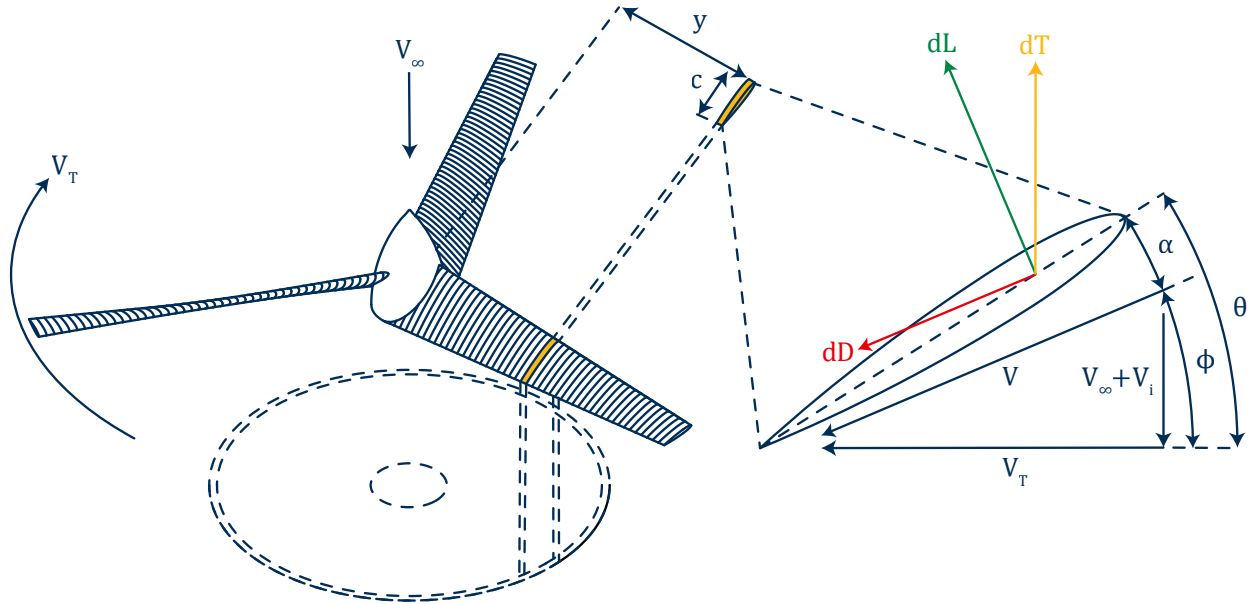


**Fig. 2.42:** Definition of 2D blade element parameters.

During rotation, each element sweeps out an annular region, as shown in Figure 2.42. To compute the elemental aerodynamic force components, the local induced velocity is found by applying the Equation 2.17 to each annulus. These induced velocities dictate the local momentum inflow at the rotor plane. Typically, inflow is nondimensionalized as the inflow ratio  $\lambda$ , given in Equation 2.19, where  $V_\infty$  is the freestream velocity, and  $\Omega R$  is the tangential tip speed based on rotor rotational velocity  $\Omega$  and radius  $R$ .

$$\lambda = \frac{V_\infty + v_i}{\Omega R} \quad (2.19)$$

The magnitude of the local flow velocity for each annulus is given by Equation 2.20, where the local tangential velocity  $V_T = \Omega y$  and  $y$  is the distance from the rotor center to blade element (see Figure 2.42). The design helical tip-speed, calculated using Equation 2.20 for the outermost blade element, was restricted to a Mach number  $M$  of 0.8 for sizing purposes to limit the effects of transonic aerodynamics.

$$V = \sqrt{(V_i + V_\infty)^2 + (V_T)^2} \quad (2.20)$$

Given a blade twist distribution, local angles of attack can be calculated using Equation 2.21, where  $\phi$  is the local inflow angle (Equation 2.22),  $\theta$  is the local blade pitch angle, and  $\theta_c$  is the collective pitch angle.

$$\alpha = \theta + \theta_c - \phi \quad (2.21)$$

$$\phi = \tan^{-1} \left( \frac{V_i + V_\infty}{V_T} \right) \quad (2.22)$$

From there, elemental lift and drag increments can be calculated using Equation 2.23 and Equation 2.24, based on the 2D aerodynamic properties of local blade cross-sections. Thrust, torque, and power values for each element follow these computations. Inflow and thrust values predicted by blade element theory can be iteratively matched with those determined using momentum theory to produce a higher fidelity method known as blade element momentum theory.

$$dL = \frac{\rho V^2 C_l c}{2} dy \quad (2.23)$$

$$dD = \frac{\rho V^2 C_d c}{2} dy \quad (2.24)$$

While blade element momentum theory is not as accurate as more advanced methods such as prescribed-wake models and computational fluid dynamics (CFD), complicated effects such as hub/tip losses and swirl losses can be simply approximated using Equations 2.25-2.28. Equation 2.27 is the Prandtl tip-loss function  $F$ , which is based on the hub and tip-loss parameters  $f_h$  and  $f_t$ . The number of rotor blades is denoted by  $N_b$  and  $r$  is the radial position, normalized by the rotor radius  $R$ . Equation 2.28 yields the swirl factor  $a'$ , which can be used to determine the local swirl velocity profile (Equation 2.29).<sup>(60)</sup>

$$f_h = \frac{N_b r}{2(1 - r)\phi} \quad (2.25)$$

$$f_t = \frac{N_b(1-r)}{2r\phi} \quad (2.26)$$

$$F = \frac{2 \cos^{-1}(e^{-f_h f_t})}{\pi} \quad (2.27)$$

$$a' = \frac{1}{2} - \frac{1}{2} \sqrt{\frac{1 - 4\lambda_i^2}{r^2}} \quad (2.28)$$

$$V_{swirl} = a' y \Omega \quad (2.29)$$

Including  $F$  and  $a'$  in the calculations for elemental thrust  $dT$ , torque  $dQ$ , and power  $dP$  results in Equations 2.30-2.32, which can be nondimensionalized according to Equations 2.33-2.35.

$$dT = FN_b(dL \cos(\phi) - dD \sin(\phi)) \quad (2.30)$$

$$dQ = (N_b(dL \sin(\phi) + dD \cos(\phi))y)(1 + a') \quad (2.31)$$

$$dP = (N_b(dL \sin(\phi) + dD \cos(\phi))\Omega * y)(1 + a') \quad (2.32)$$

$$dCT = \frac{dT}{\rho AV_{tip}^2} \quad (2.33)$$

$$dCQ = \frac{dQ}{\rho AV_{tip}^2 R_{rot}} \quad (2.34)$$

$$dCP = \frac{dP}{\rho AV_{tip}^3} \quad (2.35)$$

Summing the element-specific values given by Equations 2.30-2.35, the total rotor thrust  $T$ , torque  $Q$ , and power  $P$  requirements can be determined, along with common performance metrics such as the rotor figure of merit  $FM$  and propulsive efficiency  $\eta_p$  (Equation 2.36).

$$\eta_p = TV_\infty/P \quad (2.36)$$

While symmetric or near-symmetric airfoils have historically been typical for helicopters, convertible aircraft have a wider range of available options. The Bell XV-15, an experimental tiltrotor aircraft, used the highly cambered NACA 64XX family of airfoils.<sup>(126)</sup> For the present study, rotor performance was evaluated using NACA 44XX airfoil properties. This airfoil family is commonly used by hobby propeller manufacturer Advanced Precision Composites for both fixed-wing and multi-rotor aircraft designs.<sup>(127)</sup>

The XQ-139's rotor sizing trends were determined using the approach given in Reference (128). An ideal (constant) nominal inflow ratio  $\lambda_0$ , defined as the local inflow ratio  $\lambda_i$  divided by  $\cos(\phi)$ , was assumed over the rotor disk area. Then Equation 2.22 and Equation 2.37 were used to back out a matching chord and twist distribution for a given diameter  $D$ , blade number  $N_b$ , and freestream velocity  $V_\infty$ , based on rotor projected (weighted) solidity values. These three parameters were varied to produce a rotor design that was optimized for some velocity greater than zero when driven by the maximum installed power, with an ideal root chord matching the side length of an inscribed regular polygon of  $N_b$  sides.

$$c_{ideal}(r) = \frac{8\pi Rr^2}{C_l N_b} \left[ \frac{\lambda_0(\lambda_\infty + \lambda_0)}{[(r^2 + \lambda_\infty(\lambda_\infty + \lambda_0))\sqrt{(\lambda_\infty + \lambda_0)^2 + r^2}]} \right] \quad (2.37)$$

The number of blades that produced the highest hover figure of merit varied with aircraft installed power and rotor Reynolds number  $RE$ , from three at an installed power of 100 W to greater than ten at larger scales. Diameter and figure of merit trends are reported in Figures 2.43-2.44. The model did not account for variations in spanwise velocity, blade flexure, vibration, or other nonlinear aerodynamic effects, and the resulting performance predictions are intended to represent an upper bound on rotor performance for the scaled design.



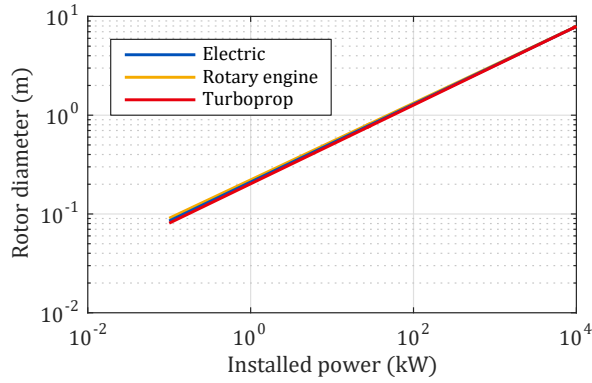


**Fig. 2.43:** Rotor diameter scaling trends for the XQ-139 concept.

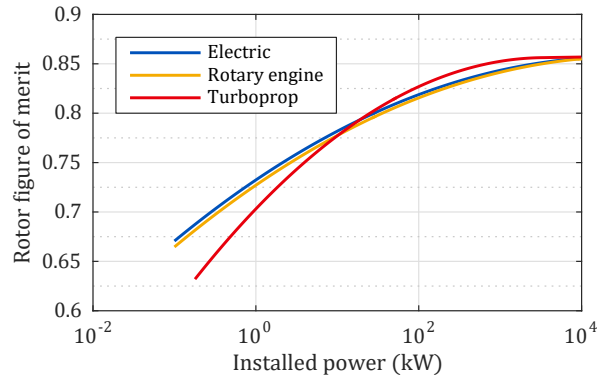


**Fig. 2.44:** Maximum rotor figure of merit scaling trends for the XQ-139 concept.

## 2.3 Aerodynamics

The XQ-139 has been designed as a zero/zero/zero (relative wing, tail, and thrust angles) aircraft with symmetric wing and tail airfoil sections. For the considered wing separation angle of 90 degrees, the aircraft is quasi-axisymmetric. This gives the XQ-139 consistent performance and greater flexibility during maneuvers and has implications for manufacturing ease and cost.

To predict three-dimensional aerodynamic performance based on airfoil test data, an aerodynamics module was created. The module output trimmed, aircraft-level aerodynamic coefficients from inputs including wing/tail aspect ratios, sweep, and taper. An optimization algorithm was used to select these variables as well as airfoil thickness in such a way as to maximize endurance, range, and cruising airspeed.

To choose an airfoil thickness for different aircraft scales, MATLAB was coupled with Mark Drela's XFOIL program.<sup>(129)</sup> Sweeping through a range of thicknesses, the module selected whichever NACA o0XX airfoil produced the highest L/D value for the expected cruise Reynolds number. For reference, Figure 2.45 depicts a contour plot of the 2D lift-to-drag ratio as a function of Reynolds number and airfoil thickness, alongside a similar plot in Figure 2.46 that shows the angle of attack at which this maximum lift/drag value occurs. This same strategy was used to map other critical points on the airfoil lift and drag curves, including the minimum drag coefficient, maximum lift coefficient (Figures 2.47-2.48), and their corresponding angles of attack.

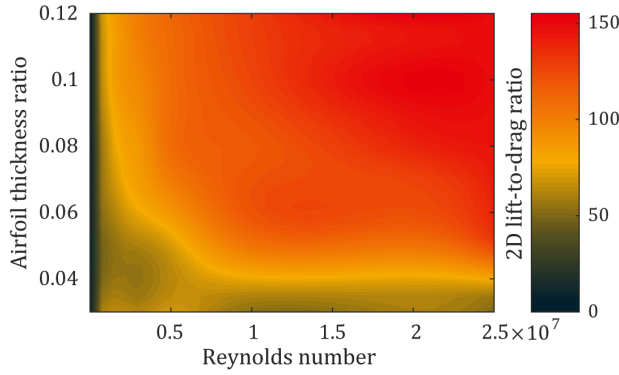


**Fig. 2.45:** Maximum 2D lift-to-drag ratio for NACA ooXX airfoil space.

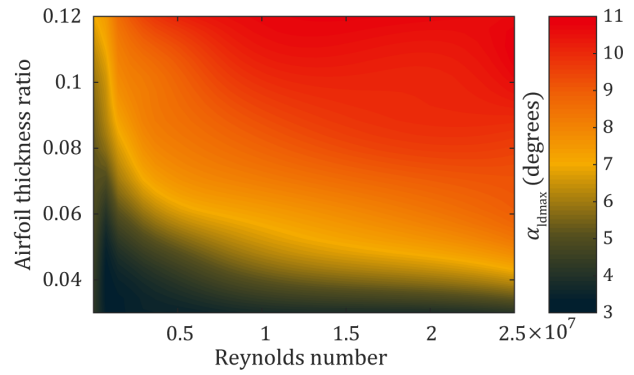


**Fig. 2.46:** Angle of attack at maximum 2D lift-to-drag ratio for NACA ooXX airfoil space.

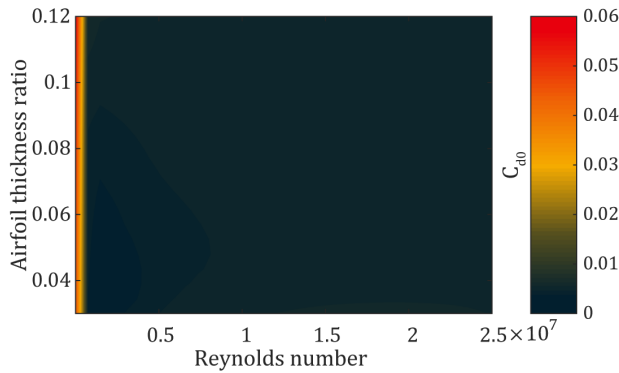


**Fig. 2.47:** Zero-lift drag coefficient for NACA ooXX airfoil space.

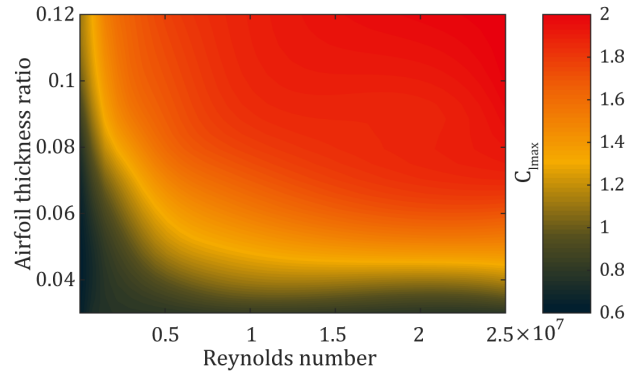


**Fig. 2.48:** Maximum 2D lift coefficient for NACA ooXX airfoil space.

These critical points were used to construct 2D lift curves that were then converted for use in 3D aircraft-level calculations using Equations 2.38-2.40, where  $C_{L\alpha}$  is the 3D lift curve slope,  $A$  is the wing aspect ratio,  $\Lambda$  is the wing sweep angle, and  $S_{exposed}/S_{ref}$  is the ratio between the exposed wing area and the planform reference area.<sup>(121)</sup> The fuselage lift factor  $F$  is given by Equation 2.39, where  $d$  is the fuselage diameter and  $b$  is the aircraft wingspan, and Equation 2.40 adjusts the wing aspect ratio to account for the endplate effects that accompany the wingtip-mounted propulsors. For aircraft in the x-orientation, two-dimensional lift and drag coefficients were transformed to account for the 45-degree wing dihedral  $\Gamma$ , according to Equations 2.41-2.43.

$$C_{L\alpha} = \frac{2\pi A}{2 + \sqrt{4 + \frac{4\pi^2 A^2}{c_{l\alpha}^2} \frac{1 + \tan^2 \Lambda}{1 - M^2}}} \frac{S_{exposed}}{S_{ref}} F \quad (2.38)$$

$$F = 1.07(1 + d/b)^2 \quad (2.39)$$

$$A_{eff} = A(1 + 1.9d/b)^2 \quad (2.40)$$

$$\alpha_{airfoil} = \cos^{-1} \left( \frac{\cos \alpha}{\sqrt{1 - \sin^2 \alpha \sin^2 \Gamma}} \right) \quad (2.41)$$

$$C_{l,3D} = \frac{C_l(\alpha_{airfoil}) \cos \Gamma}{\sqrt{1 - \sin^2 \alpha \sin^2 \Gamma}} \quad (2.42)$$

$$C_{d,3D} = \frac{C_d(\alpha_{airfoil})}{\sqrt{1 - \sin^2 \alpha \sin^2 \Gamma}} \quad (2.43)$$

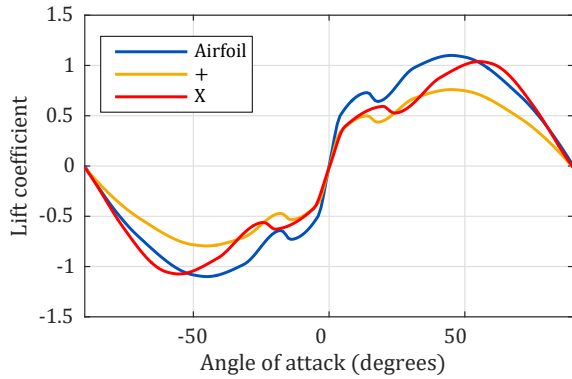
Aircraft drag values were determined using the drag build-up methods from Reference (121) and 2D airfoil drag curves. Flow in the post-stall regime was assumed to follow the flat-plate-like trends reported in Reference (130) which were used to calibrate the  $C_{D90}$  methods of Reference (131) (Equations 2.44-2.45).

$$C_L = C_{D90} \sin \alpha \cos \alpha \quad (2.44)$$

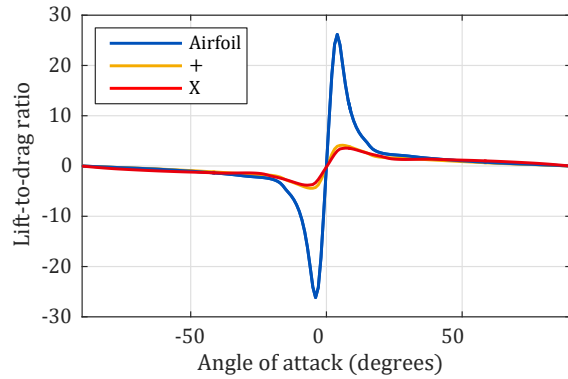
$$C_D = C_{D90} \sin^2 \alpha \quad (2.45)$$

Figure 2.49 and Figure 2.50 show a set of sample  $C_L$  and  $L/D$  curves for a small-scale XQ-139 variant with 100 W installed power. It can be seen that 3D effects result in decreased lift and a significant increase in drag levels that lead to diminished lift-to-drag ratios when compared to 2D airfoil values. A comparison of  $L/D$  values for the plus and x wing-only configurations were similar to the theoretical and wind-tunnel results given for a variable-dihedral x-wing aircraft in References (132)-(133). The results indicate slightly decreased maximum and low-angle-of-attack  $L/D$  values, but better performance at high

angles of attack for the x-configuration when compared to the plus-orientation. For the scaling study, the main wing and tailplane were taken to be rectangular geometries with equivalent reference areas, and MultiSurface Aerodynamics, a commercial vortex-lattice code from Hanley Innovations, <sup>(134)</sup> was used to estimate the wing interference effects on the lift and drag forces acting on the aircraft empennage.



**Fig. 2.49:** XQ-139 2D and 3D lift coefficients for A=6 and RE=50,000.



**Fig. 2.50:** XQ-139 2D and 3D lift-to-drag ratios for an A=6 and RE=50,000.

Interactions between the rotors and lifting surfaces were not included in the model, but would have an effect on performance. Of particular interest would be the interaction of the rotors with the wing-tip vortices and the subsequent effects on aerodynamic performance. For the x configuration, two rotors would counter wingtip vortices, while two would augment them. In the plus orientation, one wingtip vortex would be countered, while one would be augmented, leading to an imbalance in wing aerodynamic forces that might affect aircraft control and performance.

During performance analysis, the possibility of deactivating one or two rotors during cruise was considered since hover requirements ensure that the XQ-139 is overpowered during horizontal flight. Aerodynamic studies indicated, however, that the drag force on a feathered rotor would outweigh the efficiency gains achieved by operating active engines at a higher (more efficient) power setting. Figure 2.51 plots the estimated cruise drag coefficient of a feathered rotor with respect to rotor disk area. It is likely that this drag coefficient could be decreased by using less-than-optimal rotor geometry, but this

would be accompanied by diminished rotor performance; these tradeoffs were not evaluated as part of the study.

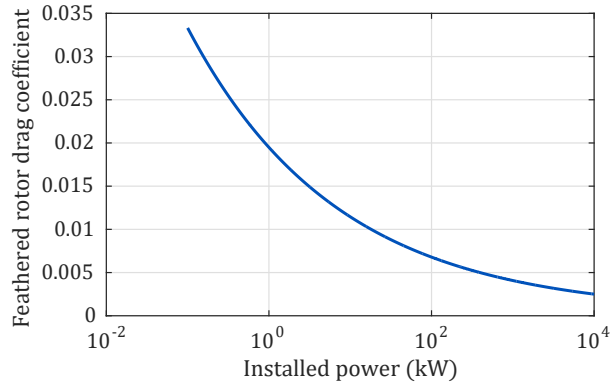


**Fig. 2.51:** Feathered rotor drag coefficient for model-optimized rotors.

## 2.4 Structures and Weights

Manned aircraft are subject to structural design requirements that are dictated by regulatory agencies such as the Federal Aviation Administration (FAA) in the U.S. and the European Aviation Safety Agency (EASA) in Europe. Limits for aircraft design load factors (lift divided by aircraft weight) are prescribed on the basis of aircraft type, size, and purpose by these authorities. Load factors can be calculated for a range of maneuvers, with a steady, level turn being the most common application. Table 2.2 lists the FAA limit load factors for different aircraft classes.

**Table 2.2:** FAA limit load factor requirements by aircraft category<sup>(135–138)</sup>

<b>Regulation</b>	<b>Category</b>	<b>Limit load factors</b>
<b>Part 23</b>	Normal and commuter airplanes	-1.52 to +3.8
	Utility airplanes	-1.76 to +4.4
	Acrobatic airplanes	-3.0 to +6.0
<b>Part 25</b>	Transport airplanes	-1 to +2.5
<b>Part 27</b>	Normal rotorcraft	-1 to +3.5
<b>Part 29</b>	Transport rotorcraft	-1 to +3.5

Versions of the XQ-139 could feasibly fit into each of the categories described in Table 2.2, and such regulations might be used to inform design decisions. Currently, UAV

design practices are not detailed under existing regulations, and there have been suggestions of reducing design safety factors for military UAS.<sup>(139)</sup> For applications that do not require high levels of maneuverability, this serves to reduce the aircraft structural mass, leaving a greater mass fraction available for fuel and cargo. As a bounding condition during the scaling study, a minimum limit load factor  $N_z = 2.0$  was applied.

The XQ-139 design is quasi-axisymmetric, with a multiplicity of large simple components. As a result, composite construction is likely a good option from the standpoints of both performance and manufacturing cost. Equation 2.46<sup>(140)</sup> was used to predict the mass of the vertical and horizontal wing/tail structures for composite materials, based on the limit load factor  $N_z$  and wing dimensions such as wingspan  $b$ , reference area  $S_{ref}$ , sweep angle  $\Lambda$ , and taper ratio  $\lambda$ . Material density  $\rho_{wing}$  and allowable stress  $\sigma_{allow}$  values for carbon fiber reinforced plastic were used, and  $\rho_{wing,Al}$  and  $\sigma_{allow,Al}$  represent the values associated with 7075-T6 aluminum construction. To estimate the remaining structural mass, methods from Reference (121) and Reference (141) were compared. Both methods resulted in empty mass fractions (empty mass divided by takeoff mass) that were below expectations based on historical data for general aviation aircraft in Reference (116). Consequently, a fixed increment of 0.17 was added to the final empty mass fraction to preserve scaling trends while better matching values seen in real aircraft. It might be expected that the XQ-139 could achieve even more favorable empty mass fractions than used in the model, but a more detailed study would be needed to justify this hypothesis. Powerplant mass was determined from the scaling studies in Sections 2.2.1-2.2.4, then multiplied by 1.2 for electric motors and 1.4 for engines to account for installation. Remaining weights were estimated from the approximate empty weight buildup factors given in Reference (121).

$$m_{wing} = \left( 0.56 \frac{\rho_{wing,Al}}{\sigma_{allow,Al}} + \frac{\rho_{wing}}{\sigma_{allow}} \right) \frac{b^3 N_z W}{8 S_{ref} \left( \frac{5}{6} t/c \right) \cos^2 \Lambda} \frac{2}{3} \frac{1 + 2\lambda}{1 + \lambda} + (3.60 \text{ kg/m}^3) S_{wet} \quad (2.46)$$

It can be seen from Equation 2.46 that a high-aspect ratio wing weighs more than a low-aspect wing with the same planform area. However, a high-aspect ratio wing is more aerodynamically efficient than a low-aspect ratio wing. Therefore, there is a tradeoff

between aerodynamic efficiency and structural weight since both factors play significant roles in aircraft performance. XQ-139 empty mass fraction trends for the studied powerplant types are shown in Figure 2.52. Variations are dependent on the geometric and mass differences of each powerplant type and the changing aerodynamic requirements as scale increases or decreases.

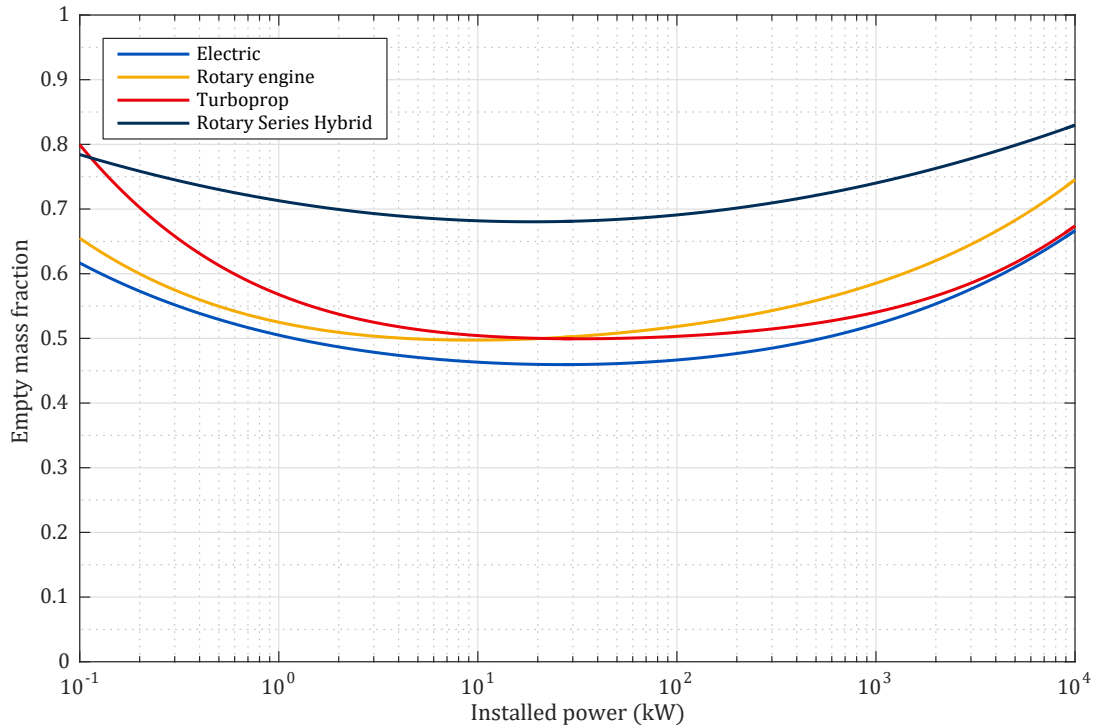


**Fig. 2.52:** XQ-139 empty mass fraction scaling trends as modeled.

## 2.5 Transition Strategy

Detailed stability and control analysis of the XQ-139 was not undertaken as part of this study. The governing theories and control strategies are well-understood and match those used for fixed-wing and multi-rotor aircraft. Still, specialized control problems dealing with gust stability and transition between flight modes are targets of future research.

The transition strategies that minimize total energy and power requirements are shown in Figures 2.53-2.54.<sup>(45)</sup> The transition from hover to forward flight follows a procedure

devised by Ernst Heinkel during World War II.<sup>(142)</sup> The process begins with an acceleration to the minimum power condition in multi-rotor (low-speed) flight mode at  $V_{mpLS}$ . This maximizes the excess power available for a vertical climb. The XQ-139 then climbs to build up its potential energy before entering a powered dive, surpassing its stall-speed  $V_{stall}$ , and leveling out for forward flight. The horizontal-to-hover exit transition, developed by Dr. Ron Barrett, reverses the process, with the XQ-139 performing a low-power, low-g, pullup maneuver into a zoom climb until the rate of climb (RC) equals zero before descending slowly to avoid vortex-ring and windmill brake state instabilities. If rapid transitions are required, the aircraft can make use of a parachute or be fitted with airbrakes to minimize the required kinetic energy bleed.

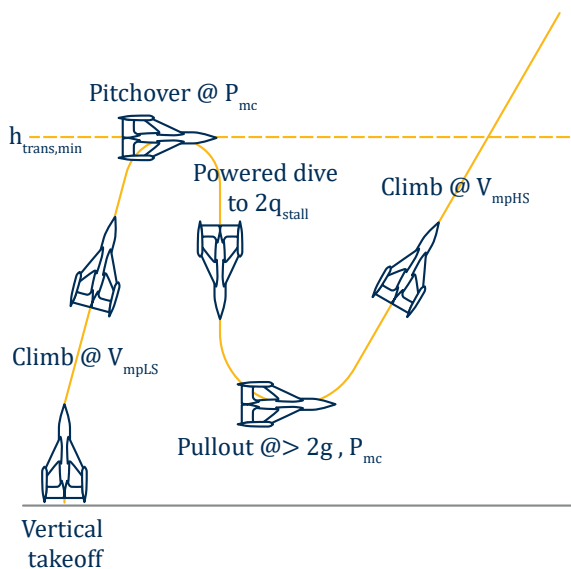


**Fig. 2.53:** XQ-139 entry transition.

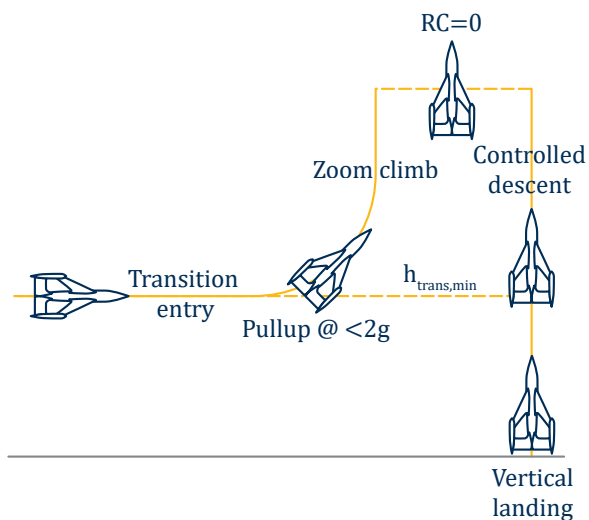


**Fig. 2.54:** XQ-139 exit transition.

Figure 2.53 depicts a high-performance transition that is appropriate for unmanned aircraft without cargo low-g requirements. Manned variants or aircraft carrying sensitive cargo can transition by pitching over from the vertical-takeoff orientation while accelerating at  $1g$ . This strategy expends more energy and requires more time to transition than the high-performance transition. Tests undertaken as part of the XQ-138 program indicate that a thrust margin of 30% or greater is desirable for transition,<sup>(45)</sup> and a 33% margin was used for the scaling study to accommodate this requirement and to enable engine-out VTOL operations, much like the Bell X-22A.<sup>(59)</sup>



## 2.6 Performance

The major advantage of the XQ-139 configuration is its ability to efficiently operate at high-speeds from a VTOL platform, and design optimization for the sizing study was carried out to capitalize on this advantage. While cruising, the XQ-139 performs like a standard fixed-wing aircraft. As a result, performance metrics such as cruise endurance and range can be calculated using Equation 2.47-2.48. For a propeller-driven aircraft, the speed that maximizes endurance is also the speed that minimizes power requirements  $V_{mp}$ . Maximum range can be achieved at the speed that yields the highest lift-to-drag ratio, which coincides with the minimum thrust condition.

$$E = \int_{W_f}^{W_i} \frac{\eta_p}{SFC} \frac{L}{DV} \frac{dW}{W} \quad (2.47)$$

$$R = \int_{W_f}^{W_i} \frac{\eta_p}{SFC} \frac{L}{D} \frac{dW}{W} \quad (2.48)$$

With this understanding, it is possible to optimize the design for either endurance or range according to instantaneous power and thrust requirements. While either approach is viable and would be well-suited for certain mission requirements, targeting cruise speed performance would better amplify the advantages of the XQ-139 concept.

Standardly, the optimum cruise condition for an aircraft is taken to occur at “Carson’s speed”, which minimizes the fuel flow per unit airspeed and corresponds to the minimum value of  $T/V$ .<sup>(143)</sup> This value, however, is of greatest use from an operational standpoint, when determining an aircraft’s proper cruise speed, and not necessarily for design. This is because increases in cruise speed primarily come from a reduction of wetted wing area. Side effects include decreased volume for fuel storage and greater structural requirements that affect the aircraft’s useable mass fraction.

For the current study, scaled designs were optimized by sizing each aircraft so that the parameter  $T_C/W_{use}V_C$  was at a minimum. This represents the goal of moving the largest amount of useful mass (in the form of fuel or payload) as fast as possible with the smallest propulsive force and provides an objective value with which to compare alternative designs

or aircraft. Once the design is set, an aircraft's design cruise speed matches Carson's speed. Figure 2.55 plots  $T_C/W_{use}V_C$  for a range of VTOL and conventional aircraft. It can be seen that the XQ-139 outperforms its VTOL competitors with performance on par with dedicated fixed-wing transport aircraft.

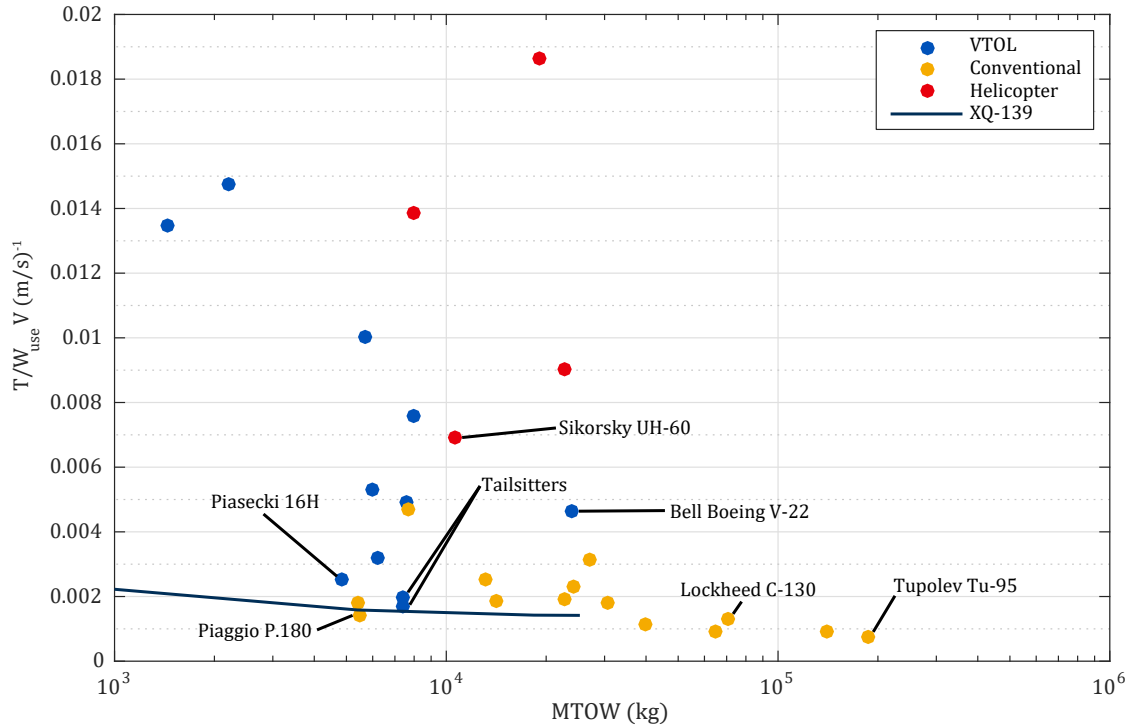


**Fig. 2.55:** Comparison of  $T/(W_{use} V_C)$  for XQ-139 and other aircraft options.

Figures 2.56-2.61 plot trends for important variables used in the scaling study, and Figures 2.62-2.65 present the results of the scaling performance study itself. FCS UAV classes are denoted by the green regions for reference, based on mass, as presented in Table 1.1. The four lines for each powerplant indicate calculations performed for payload-to-useful-load ratios  $m_{pay}/m_{use}$  of 0%, 25%, 50%, and 75%. In 2.64, it can be seen that each of the plotted propulsion strategies performs best at different scales. Turboprops are the best option for most of the Class IV range, while aircraft sized from Class II to the low end of Class IV are best served by rotary engines. The rotary series hybrid shows up as the best option in for aircraft just outside Class I up through Class II. Comparing Figure 2.65

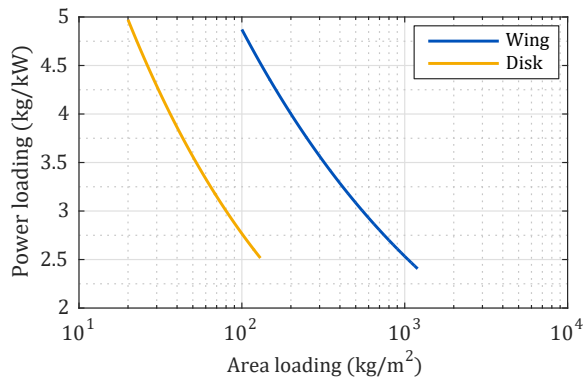


**Fig. 2.56:** Sizing trends for XQ-139 design.

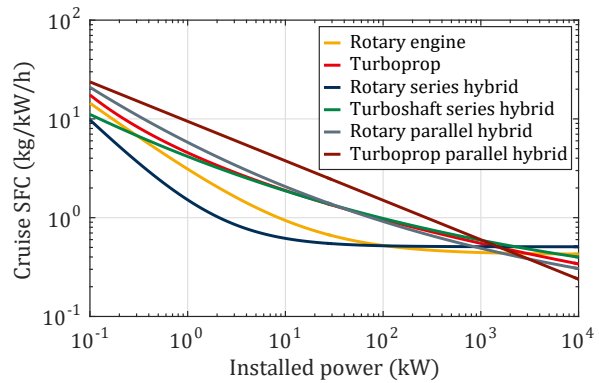


**Fig. 2.57:** XQ-139 cruise SFC scaling trends.

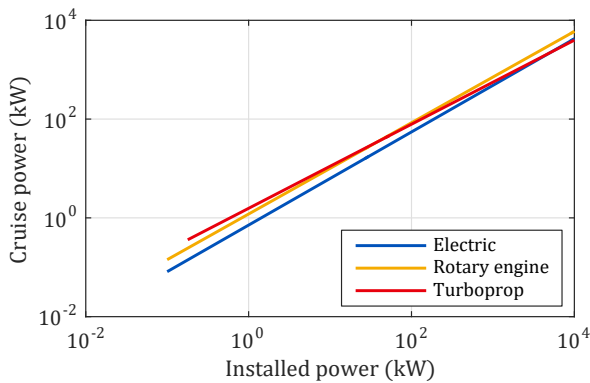


**Fig. 2.58:** XQ-139 cruise power scaling trends.

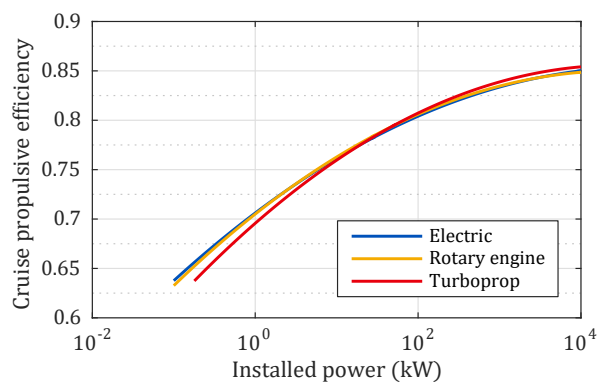


**Fig. 2.59:** Cruise efficiency scaling trends.

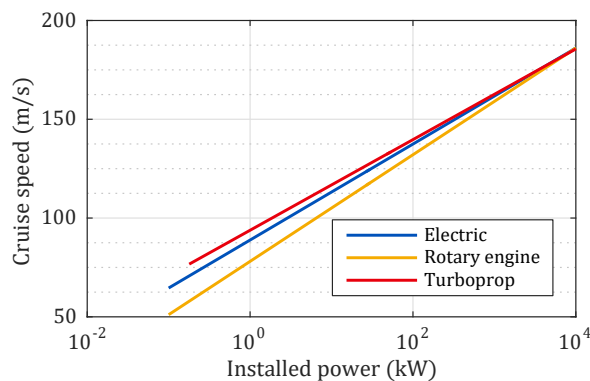


**Fig. 2.60:** XQ-139 cruise speed scaling trends.

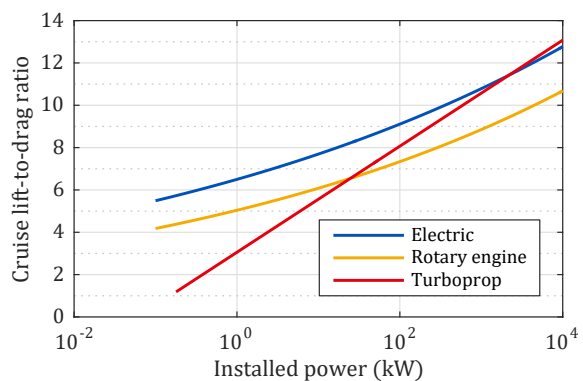


**Fig. 2.61:** XQ-139 cruise L/D scaling trends.

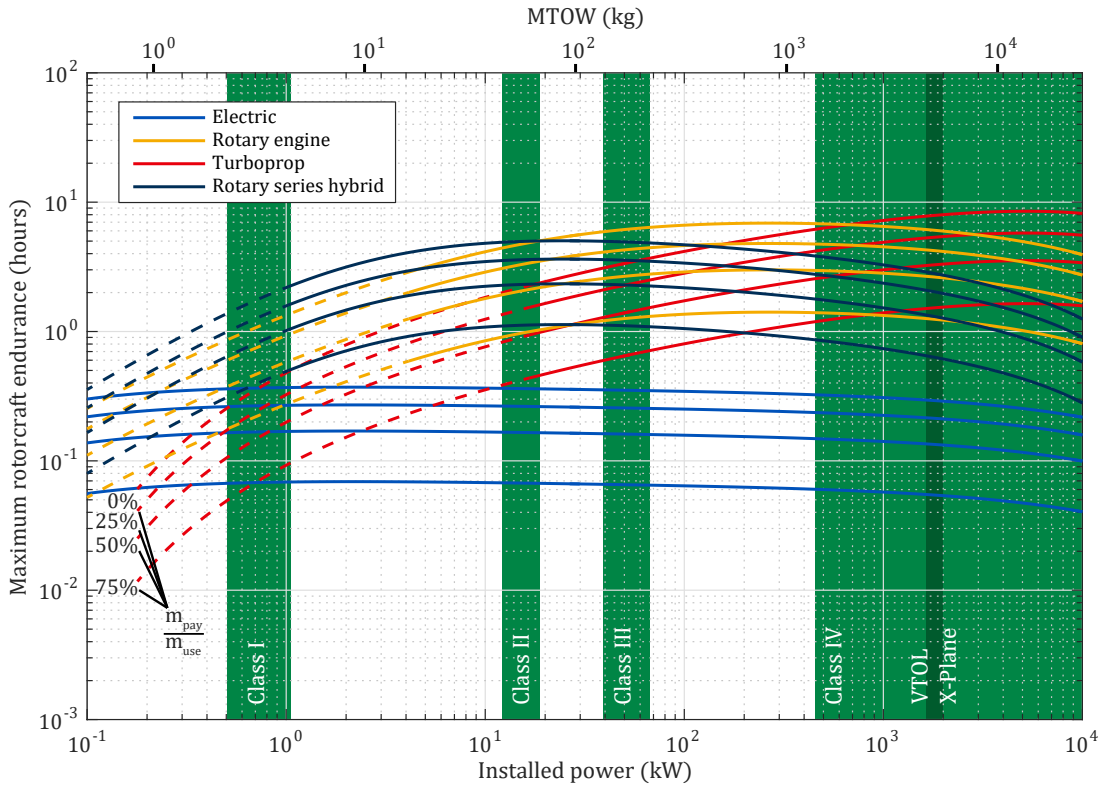


**Fig. 2.62:** XQ-139 rotorcraft endurance scaling trends

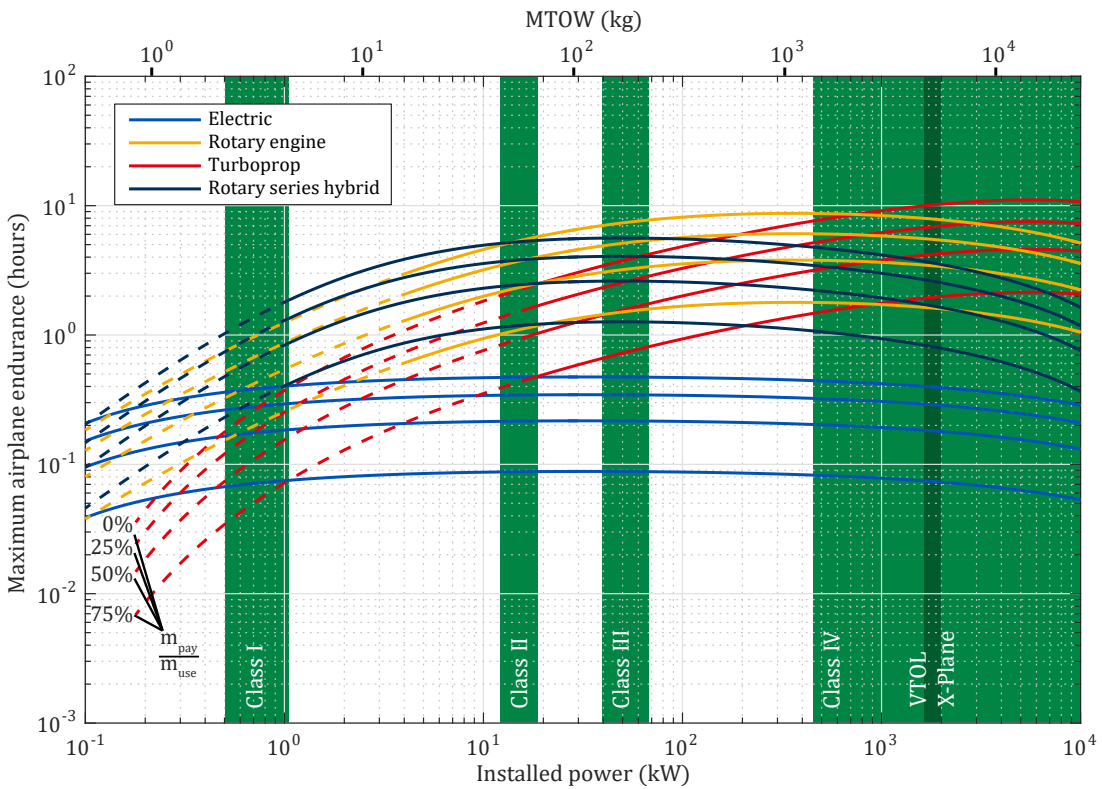


**Fig. 2.63:** XQ-139 maximum endurance scaling trends.

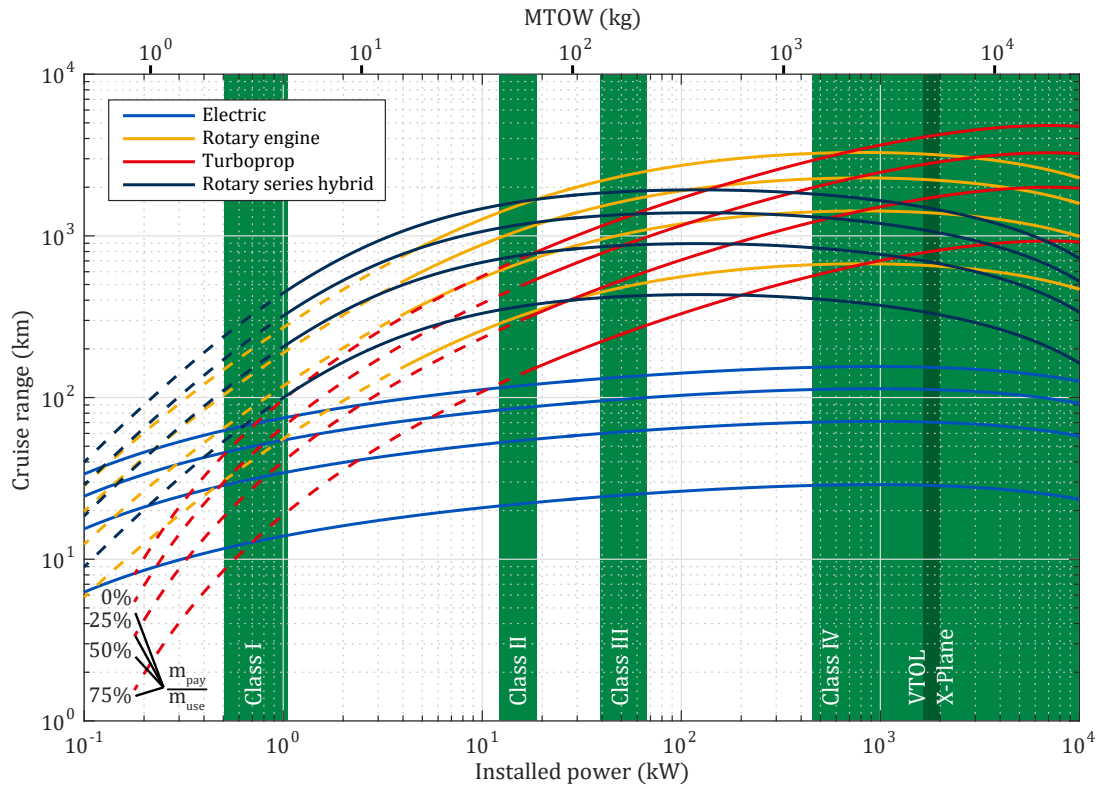


**Fig. 2.64:** XQ-139 cruise range scaling trends.

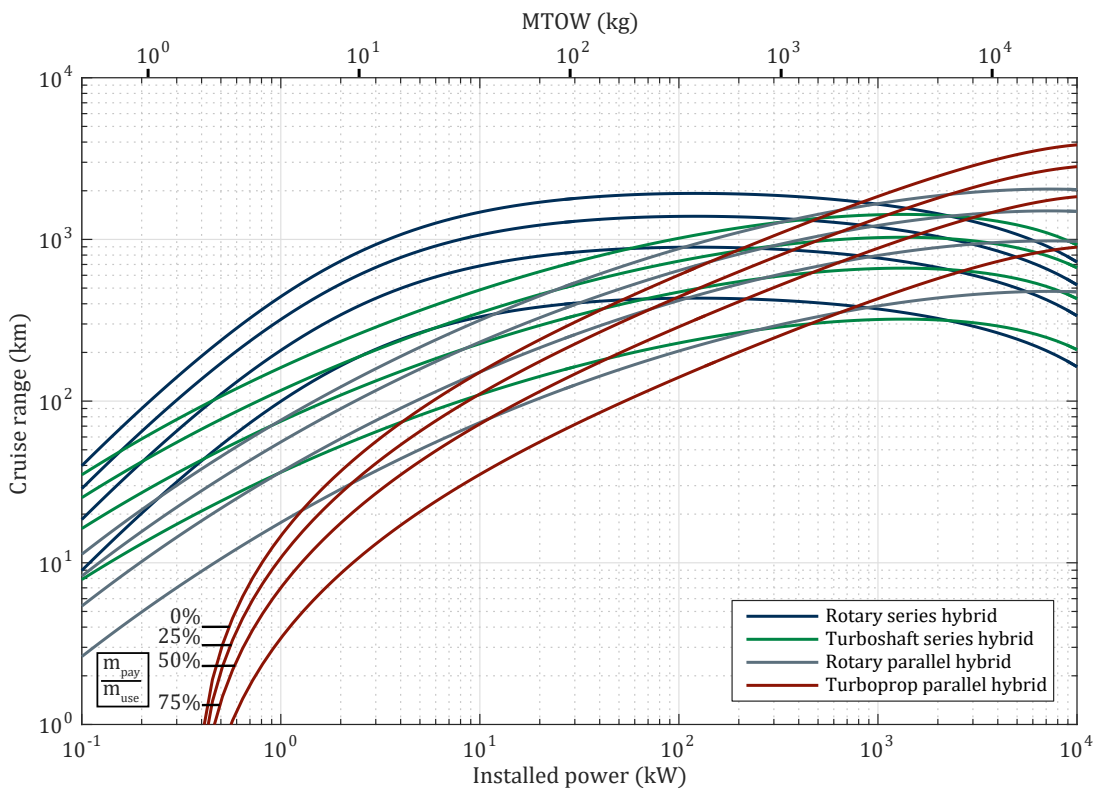


**Fig. 2.65:** Cruise range scaling trends for XQ-139 hybrid propulsion.

with Figures 2.63-2.64 demonstrates that the rotary series hybrid is the only hybrid option that outperforms electric, rotary engine, or turboprop designs in the considered range of aircraft sizes. It was found that performance differences between the x and plus orientations were comparable at high speeds, but that the x-configuration was superior for low speed, high-alpha horizontal flight, where it allowed for a 5-15% reduction in minimum flight speed. This matches the findings in Reference (132) that an x-wing configuration improves endurance when compared to a monowing aircraft, but not necessarily range.

While the plots show trends throughout the studied range, designs should account for current technological limits. For example, while the rotary series hybrid design outperforms all other options over the lower half of the scale, an examination of existing powerplants in Appendix B.2 suggests that rotary engines that deliver less than 1 kW are not currently feasible. Electric power should therefore be considered as the only option up to the 1 kW total power requirement. The dashed lines in Figures 2.62-2.65 represent results that are unlikely to be achieved with current technology, but may be viewed as projections for future micro-engine systems. At this point, however, there seem to be no foreseeable advantages when compared to electric propulsion at the lower end of the scale.

Using the results of the scaling study, quick assessments can be made with regard to aircraft sizing, propulsive strategy, and aircraft performance. Equation 2.49 gives an estimate of minimum XQ-139 installed power requirements, based on MTOW in kilograms.

$$P_{inst} = 0.2153m^{1.060} \tag{2.49}$$

Table 2.3 lists the estimated specifications for an example set of XQ-139 UAS.

**Table 2.3:** Example XQ-139 UAS.

<b>Class</b>	<b>I</b>	<b>II</b>	<b>III</b>	<b>IV</b>
<b>Propulsion</b>	Electric	Hybrid	Rotary	Turboprop
<b>Installed Power</b>	1 kW	14 kW	58 kW	1750 kW
<b>Footprint</b>	0.2 m <sup>2</sup>	1.4 m <sup>2</sup>	4.6 m <sup>2</sup>	63 m <sup>2</sup>
<b>MTOW</b>	4 kg	60 kg	200 kg	4500 kg
<b>Empty weight</b>	2 kg	39 kg	102 kg	2520 kg
<b>Payload</b>	0.5 kg	5 kg	25 kg	500 kg
<b>Cruise speed</b>	320 km/h	420 km/h	450 km/h	605 km/h
<b>Endurance</b>	0.29 h	3.8 h	5.2 h	6.8 h
<b>Range</b>	55 km	1100 km	1650 km	2700 km

*First rule of engineering; beware prototypes.  
Along with, avoid anything made by an  
engineer who doesn't have all his own fingers.*

— Simon Green, *Spirits From Beyond*, 2013<sup>(144)</sup>

## 3 XQ-139B DESIGN AND CONSTRUCTION

### Contents

---

<b>3.1 Sizing</b> . . . . .	<b>64</b>
<b>3.2 Propulsion</b> . . . . .	<b>65</b>
<b>3.3 Electronics</b> . . . . .	<b>65</b>
<b>3.4 Structures</b> . . . . .	<b>67</b>
<b>3.5 Summary</b> . . . . .	<b>69</b>

---



**Fig. 3.1:** XQ-139A prototype.



**Fig. 3.2:** XQ-139B design.

Previously, small versions of the XQ-139 configuration have been constructed, including the XQ-139A, shown in Figure 3.1. The XQ-139B (Figure 3.2) was created to develop and demonstrate the capabilities of the XQ-139 configuration at the largest scale yet. The

aircraft was designed to include control surfaces, unlike previous builds of the XQ-139A, and was sized to carry a <1-kg payload such as a gimbal-mounted camera or a small gun. While variable-pitch propellers will eventually be necessary for the XQ-139B to maximize its forward-flight performance, the current aircraft was fitted with 12x6 rotors from APC for preliminary hover-mode flight testing.

### 3.1 Sizing

The XQ-139B was sized around the E-flite Power 10 brushless DC motor, shown in Figure 3.3.<sup>(145)</sup> Each motor offers up to 450 W of power, which is roughly an order of magnitude more power than the Turnigy 1811 motors used for the XQ-139A. DriveCalc software<sup>(146)</sup> was used to match the motor with APC's 12x6 E-series propellers. A square cross-section was chosen for the fuselage to minimize its wetted area while housing rectangular components like the control board and batteries, and the wingspan was set by the rotor diameter. Since the XQ-139B is an early-generation demonstrator, the wing and tail were designed with lower aspect ratios than a high-speed production aircraft might employ. This enables reduced horizontal flight speeds where aircraft behavior can most easily be observed during the refinement process. In the plus-orientation, the wing and empennage each have approximately 360 cm<sup>2</sup> of exposed area.



**Fig. 3.3:** E-flite Power 10 brushless DC motor.



## 3.2 Propulsion

Components of the XQ-139B's propulsion system are highlighted in the CAD graphic in Figure 3.5. Four E-flite Power 10 brushless DC motors were chosen for propulsion of the XQ-139B. Each was paired with a fixed-pitch APC 12x6 propeller (Figure 3.4) and an E-flite 40-amp ESC for preliminary testing. While the APC propellers provide large amounts of static thrust, their pitch speed is only 70 km/h. Therefore, a variable-pitch system must be installed in the future to explore the full scope of the XQ-139B's advantages.

DriveCalc predicts up to 1.6 kg of thrust for each motor/prop combination. This is expected to yield a thrust-to-weight ratio in excess of 1.5. Four 2200mAh Turnigy battery packs have initially been specified to power the aircraft, but may be replaced by a single large battery pack in the future.



**Fig. 3.4:** APC 12X6E propeller.<sup>(147)</sup>



**Fig. 3.5:** XQ-139B propulsion system.

## 3.3 Electronics

The XQ-139B's electronics package includes the components of the electric propulsion system, as well as an SP Racing F3 Deluxe control board, a Spektrum AR610 Receiver, and four Hitec HS-55 servos for control surface actuation (Figures 3.6-3.8).



**Fig. 3.6:** SP Racing F3 Deluxe.

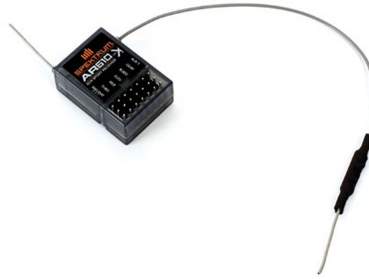


**Fig. 3.7:** Spektrum AR610.



**Fig. 3.8:** Hitec HS-55.

For stability purposes, the batteries are located in the aircraft nose, as shown in Figure 3.9. Wiring for the propulsion system has been routed from the main electronics bay through an internal sleeve in the wing to the ESCs, which are located in the “power pods” at the wingtips (Figure 3.10). While the motors are well-cooled in flight, overheating might be a concern for the closed-in speed controllers, and must be monitored. Servo wiring passes through the fuselage to where the servos are mounted at the base of the aircraft, as seen in Figure 3.11.



**Fig. 3.9:** Nose-mounted electronics bay.

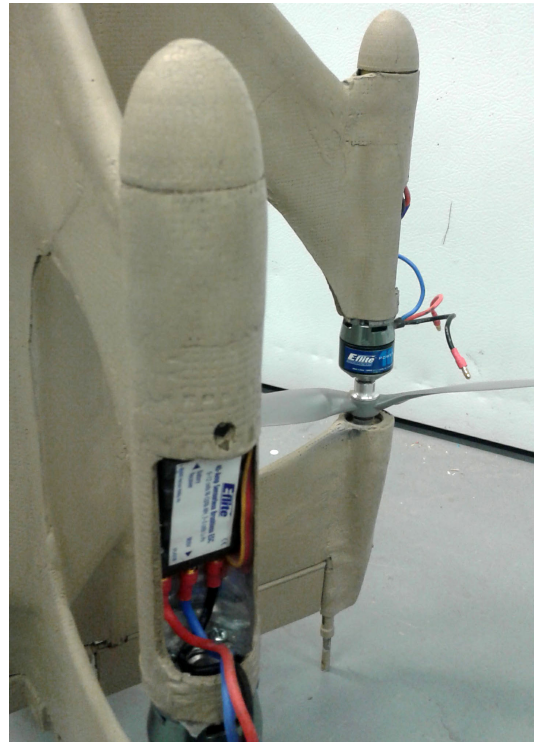


**Fig. 3.10:** ESC installation.









**Fig. 3.11:** Servos installed for control surface actuation.

### 3.4 Structures

Figure 3.12 gives an overview of the structural makeup of the XQ-139B. Carbon fiber quadrants were laid up on the tooling shown in Figure 3.13, then joined around aluminum canisters that served as motor mounts and housing for the ESCs. 8-mm carbon tubes were implanted within each leading edge, and 5-mm crosstubes were added to stiffen the empennage.

Rigid expanding foam was then injected into the wings to form a light but stiff sandwich structure, and a layer of carbon fiber cloth was cured over a depron core to stiffen the fuselage without sacrificing internal volume. The nose was manufactured out of vacuum-formed polycarbonate, which was meant to be both invisible to radio waves and easily rebuilt if damaged. The nose mold is shown in Figure 3.14. As can be seen in Figure 3.11, aluminum shock-absorbers were implanted at the rear of the empennage to protect the carbon airframe from impacts during the landing process.

- |   |                        |   |                |
|---|------------------------|---|----------------|
|  | Carbon-depron sandwich |  | 3D-printed PLA |
|  | Foam-core carbon fiber |  | Carbon tube    |
|  | Polycarbonate          |  | Aluminum       |

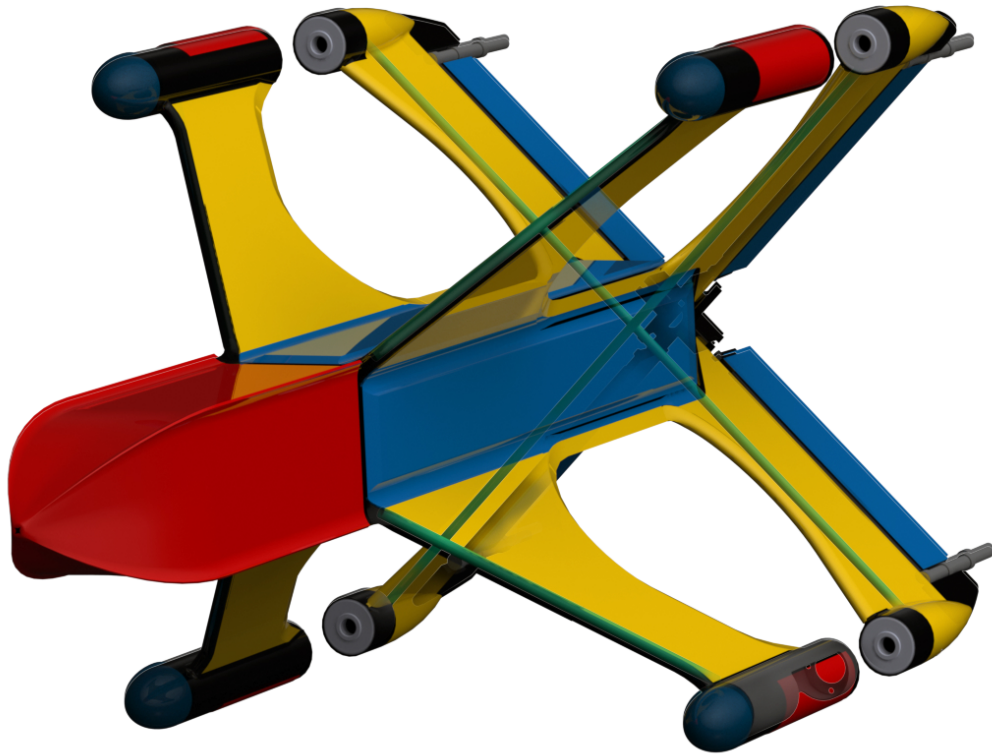


**Fig. 3.12:** XQ-139 structural makeup.



**Fig. 3.13:** XQ-139B main quadrant tool.

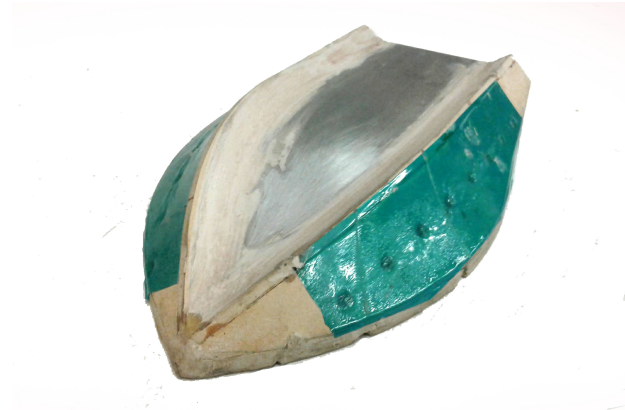


**Fig. 3.14:** XQ-139B nose tool.

### 3.5 Summary

Figure 3.15 shows the completed prototype. The aircraft is 84 cm tall, weighs 2.7 kg (including batteries) and is expected to be able to lift 1.5 kg of payload using 1.4 kW of onboard power. It has a 48-cm wingspan and a 0.6-m<sup>2</sup> takeoff and landing footprint. Future test results will quantify its true performance capabilities.

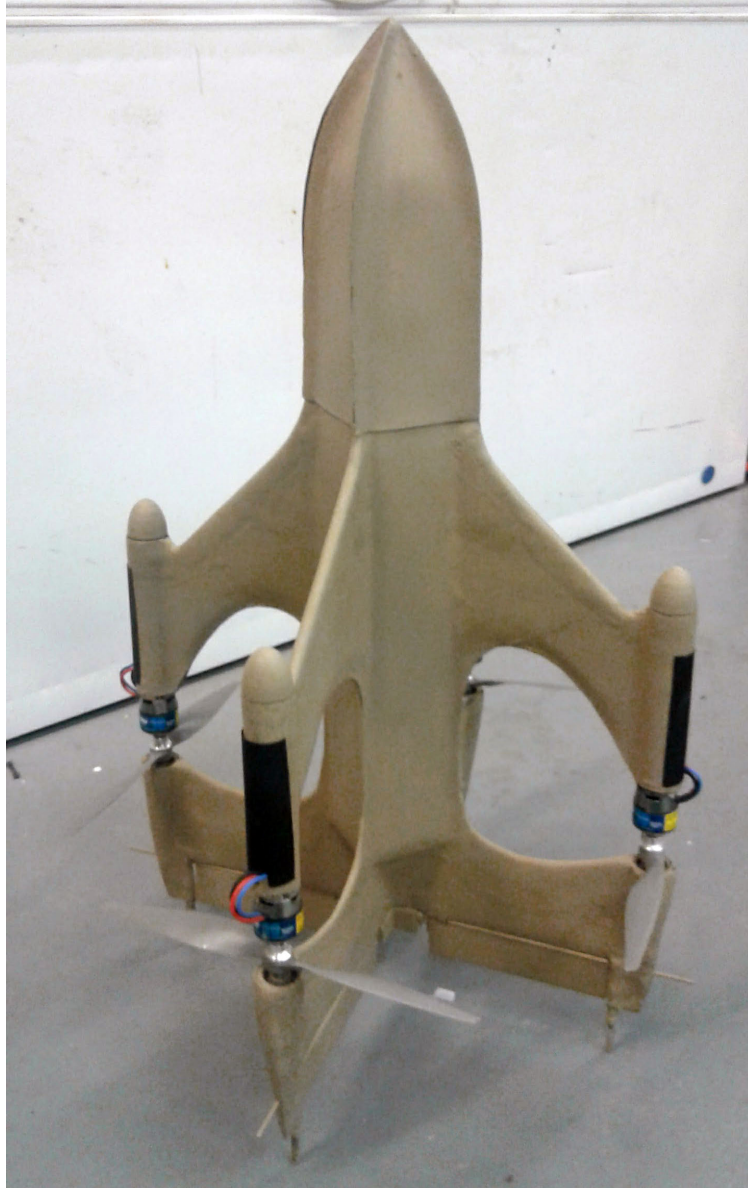


**Fig. 3.15:** XQ-139B prototype.

*At that time [1909] the chief engineer was almost always the chief test pilot as well. That had the fortunate result of eliminating poor engineering early in aviation.*

---

— Igor Sikorsky<sup>(149)</sup>

## 4 TESTING AND RESULTS

A Turnigy H.A.L. (Heavy Aerial Lift) quadcopter frame<sup>(148)</sup> was purchased for the purpose of comparative hover testing versus the XQ-139B. The H.A.L. frame was assembled, and the same propulsion system as the XQ-139B was installed, as shown in Figures 4.1.

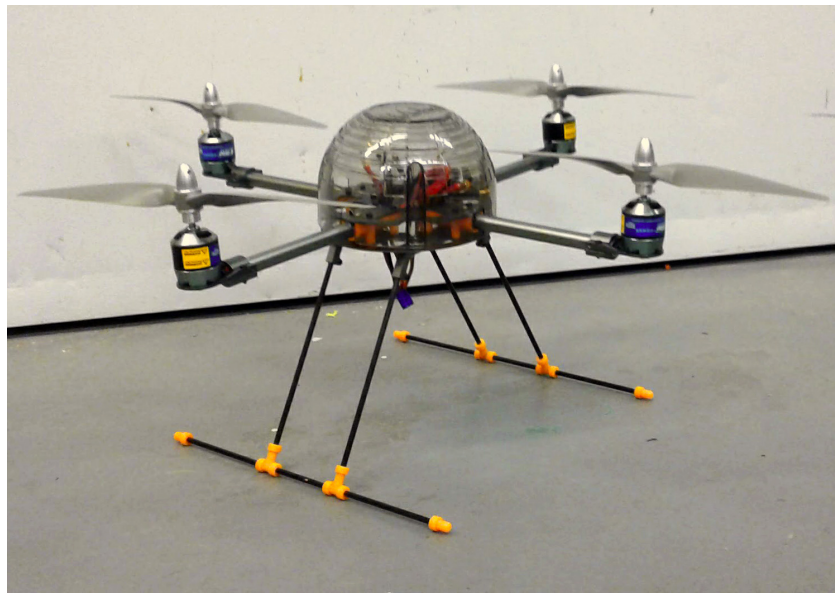


**Fig. 4.1:** Turnigy H.A.L. for comparative testing.

While transition and horizontal flight tests are important to demonstrate the true advantages of the XQ-139 design, only one airframe was constructed as part of this thesis. Therefore, testing was limited to ensure the XQ-139B's survival.

A major point of comparison between the two aircraft is efficiency in hover, where the vertically-oriented wings of the XQ-139B would be expected to offer increased performance. To test this hypothesis in a controlled fashion, both the XQ-139B and the H.A.L.

unit were fixed in a stationary position, and one rotor for each was isolated and operated using a variable DC power supply, as shown in Figure 4.2 and Figure 4.5.



**Fig. 4.2:** H.A.L. frame constrained for efficiency testing.

Test voltage was set at 11.1 VDC to match the voltage supplied by each aircraft's on-board battery pack, and the live motor was throttled using a portable servo controller. At each throttle setting, voltage and current were read, and a strobe tachometer was used to determine the rotational speed of the rotor.

While the XQ-139B was expected to outperform the H.A.L. quadcopter, the size of the streamlining effect was unknown. However, test results showed a consistent and measurable difference between the two aircraft in terms of power required to sustain a given rotor speed (Figure 4.3). Because the test was conducted with fixed-pitch rotors, rotor thrust is strongly linked to rotor speed. Using the DriveCalc software, thrust values were matched to test speeds for an estimation of the installed figure of merit for each aircraft. The results of this approach are shown in Figure 4.4.

It can be seen that the test results concur with the motor/rotor trends predicted by DriveCalc. Most importantly, the XQ-139 is seen to offer superior hover performance than the quadcopter based on the H.A.L. frame, producing higher loaded rotor speeds with approximately 5% less power. The predicted figure of merit improvements in Figure 4.4

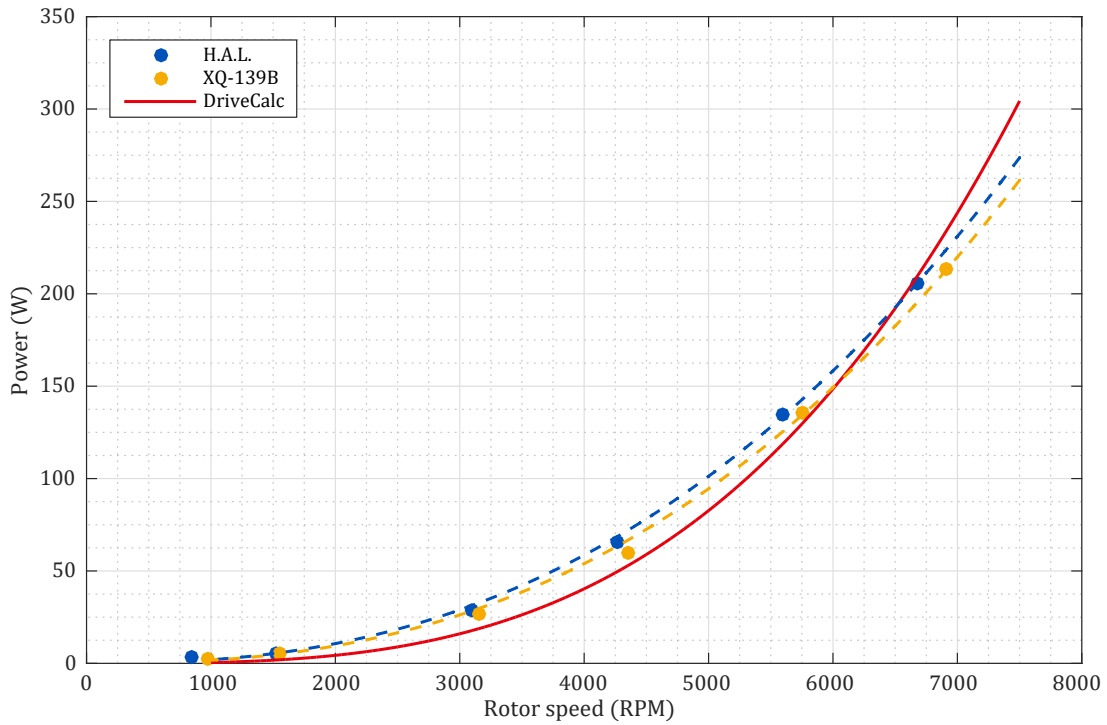


**Fig. 4.3:** Electrical power draw versus rotor speed test results.

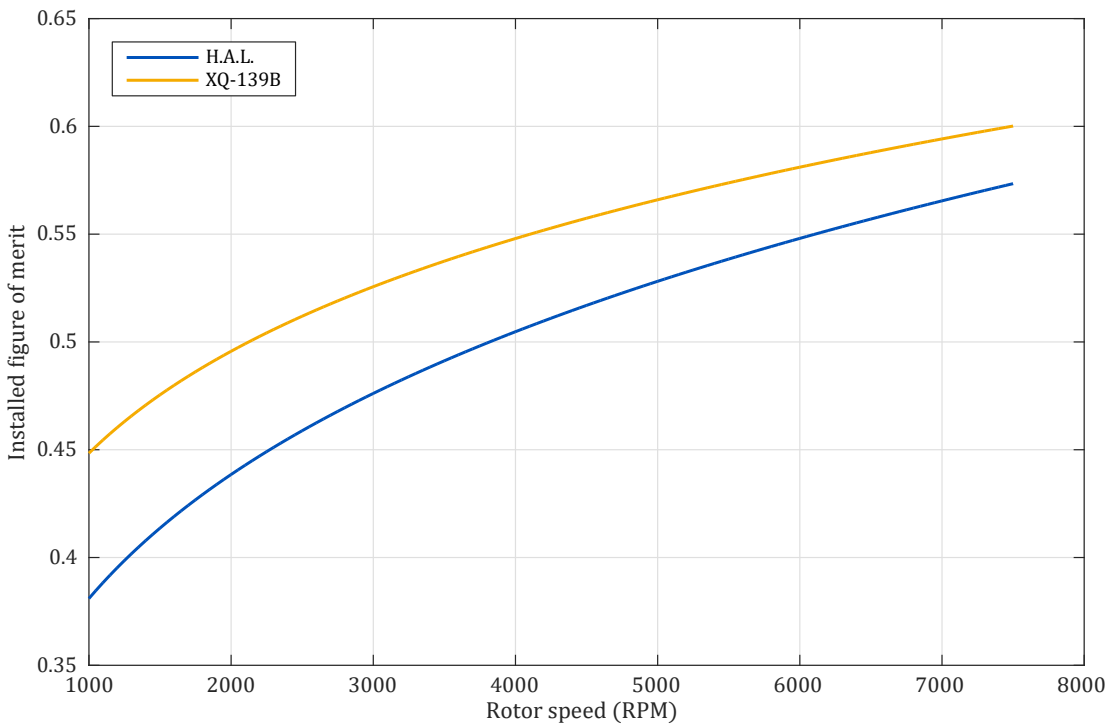


**Fig. 4.4:** Comparison of estimated [installed] figures of merit.



are impressive, but validation from actual flight test data is needed to confirm the results. Preparations for these tests are underway and will occur in the near future.



**Fig. 4.5:** XQ-139B constrained for efficiency testing.

*O to speed where there is space  
enough and air enough at last!*

---

—Walt Whitman, *One Hour to  
Madness and Joy*, 1860<sup>(150)</sup>

## 5 CONCLUSIONS AND FUTURE WORK

### Contents

---

<b>5.1 Conclusions</b> . . . . .	<b>74</b>
<b>5.2 Future Work</b> . . . . .	<b>75</b>

---

### 5.1 Conclusions

The XQ-139’s range and endurance performance was evaluated for installed power levels ranging from 100 W to 10,000 kW. It was found to produce higher cruise speeds throughout the studied scale range than traditional rotorcraft. Most notably, the configuration was shown to minimize the thrust required to transport a useful mass at a given speed relative to other VTOL options (Figure 2.55), performing on par with military transport aircraft. This is a new performance capability in the realm of VTOL UAS.

Additionally, it was found that there were distinct bands within the design space where each of the considered propulsive options (battery-electric, series hybrid, rotary engine, and turboprop) were best-suited for performance. Battery-electric propulsion was determined to be the most feasible choice up to an installed power level of around 1 kW. From 1 kW to 15 kW, the rotary series hybrid option performed best. Between 15 kW and 600 kW, rotary engine propulsion offered superior range and endurance, and beyond 600 kW, turboprops produced the highest levels of performance.

A prototype, the XQ-139B, was designed and constructed. A stationary test compared the installed efficiency of the aircraft with that of a quadcopter based on a stock frame and using the same propulsion system. It was found that the XQ-139B was approximately

5% more efficient in a steady hover-type scenario than the quadcopter to which it was compared.

## 5.2 Future Work

Future work includes hover, translational, and transitioned flight testing, as well as wind tunnel testing and automation of transition maneuvers. Experimental optimization of various designs and the addition of variable-pitch rotors will enable the exploration of the performance bounds discussed in this paper.

Enable 3D View

# **Appendices**

## A FIGURE OF MERIT DATA FOR VTOL AIRCRAFT

**Table A.1:** Figure of merit data for VTOL aircraft

<b>Aircraft</b>	<b>Rotor</b>	<b>P (kW)</b>	<b>m(kg)</b>	<b>T (N)</b>	<b>A (m<sup>2</sup>)</b>	<b>V (km/h)</b>	<b>FM</b>
AgustaWestland AW609	Open	2,894	7,600	74,556	98.0	509	0.45
AgustaWestland AW139	Open	2,284	7,000	68,670	149.6	311	0.41
Bell Boeing V-22 Osprey	Open	9,172	23,859	234,059	211.4	509	0.54
Bell X-22	Ducted	3,728	8,003	88,160	14.3	409	0.84
Bell XV-15	Open	2,312	6,000	65,316	91.2	556	0.48
Bell XV-3	Open	336	2,218	21,759	90.7	296	0.64
Boeing AH-64 Apache	Open	2,818	8,000	78,992	168.1	293	0.39
Boeing CH-47	Open	7,058	22,680	242,543	526.0	297	0.47
Canadair CL-84	Open	2,200	5,710	56,015	28.6	517	0.72
Convair XFY	Coaxial	3,803	7,370	75,727	18.7	982	0.66
Curtiss-Wright X-19	Open	2,559	6,196	60,783	49.3	732	0.53
Doak VZ-4	Ducted	750	1,451	16,723	2.3	370	0.85
Eurocopter X-3	Open	1,693	5,200	56,113	124.7	473	0.45
Hiller X-18	Coaxial	8,200	14,969	146,846	29.0	407	0.66
Hiller XC-142A	Open	8,504	16,900	165,789	69.4	695	0.61
Lockheed XFY	Coaxial	3,896	7,358	75,791	18.7	933	0.65
McDonnell XV-1	Open	391	1,940	20,935	69.4	326	0.59
Nord 500 Cadet	Ducted	472	1,200	11,772	3.5	350	0.65
Piasecki 16H Pathfinder	Open	930	4,865	47,726	141.0	370	0.60
Ryan VZ-3	Open	750	1,179	11,566	11.8	298	0.31
Sikorsky Skycrane	Open	7,110	19,050	205,569	378.4	202	0.43
Sikorsky X2	Open	1,340	3,600	40,260	50.9	463	0.54
Vertol VZ-2	Open	522	1,678	16,461	13.2	339	0.71

## B AVIATION POWERPLANT SCALING TRENDS

### Contents

---

<b>B.1 Data for Electric Motor Scaling Trends . . . . .</b>	<b>78</b>
<b>B.2 Data for Rotary Engine Scaling Trends . . . . .</b>	<b>80</b>
<b>B.3 Data for Turboprops and Turboshaft Scaling Trends . . . . .</b>	<b>81</b>

---

### B.1 Data for Electric Motor Scaling Trends

**Table B.1:** Data for electric motor scaling trends

<b>Motor</b>	<b>L(m)</b>	<b>D (m)</b>	<b>m (kg)</b>	<b>P<sub>max</sub> (kW)</b>	<b>P<sub>cont</sub> (kW)</b>	<b>RPM</b>
Eflite Park 180	0.020	0.016	0.009	0.036	0.030	25,080
Electrifly GPMG5110	0.030	0.012	0.016	0.050	0.022	45,621
Eflite Park 250	0.023	0.022	0.014	0.067	0.059	18,480
Eflite Park 300	0.022	0.028	0.024	0.100	0.078	15,318
Eflite Park 280	0.026	0.022	0.021	0.111	0.089	19,980
Eflite Park 370	0.030	0.020	0.048	0.132	0.084	43,200
Eflite Park 340		0.028	0.027	0.155	0.128	18,870
Eflite Park 400	0.029	0.028	0.056	0.156	0.120	11,040
Eflite Park 450	0.033	0.028	0.072	0.216	2.152	10,680
Electrifly GPM5155	0.033	0.024	0.067	0.220	0.167	
Eflite Park 400	0.040	0.020	0.068	0.240	0.180	44,400
Align 250MX	0.022	0.026	0.034	0.250	0.166	37,440
Electrifly GPMG5140	0.040	0.020	0.065	0.275	0.133	38,850
Electrifly GPM5165	0.033	0.024	0.067	0.310	0.200	
Electrifly GPM5170	0.033	0.024	0.067	0.330	0.222	
Eflite Park 480	0.033	0.035	0.087	0.336	0.264	12,240
Electrifly GPM5190	0.035	0.028	0.094	0.460	0.259	
Electrifly GPM5200	0.035	0.028	0.094	0.500	0.244	
Eflite Pr 10	0.043	0.035	0.122	0.504	0.384	7,800

Electrifly GPM5195	0.035	0.028	0.094	0.555	0.278	
Electrifly GPM5185	0.045	0.024	0.101	0.555	0.278	
Electrifly GPM5210	0.045	0.028	0.133	0.590	0.311	
Eflite Pr 15	0.050	0.035	0.152	0.605	0.490	
Align RCM-BL4213	0.033	0.052	0.185	0.733	0.555	
Eflite Pr 25	0.054	0.035	0.190	0.739	0.538	
Align 460MX	0.039	0.029	0.087	0.755	0.511	35,520
Electrifly GPM5225	0.056	0.028	0.166	0.830	0.426	
Electrifly GPM5215	0.045	0.028	0.133	0.925	0.518	
Eflite Pr 25 BL	0.054	0.035	0.183	0.974	0.840	
Eflite Pr 32	0.050	0.042	0.200	1.01	0.706	
Electrifly GPM5220	0.045	0.028	0.133	1.04	0.592	
Eflite Pr 46	0.055	0.050	0.290	1.06	0.768	
Eflite Pr 52		0.050	0.346	1.67	1.443	
Eflite Pr 60	0.062	0.050	0.380	1.78	1.443	
Electrifly GPM5290	0.050	0.036	0.243	1.85	1.110	
Electrifly GPM5315	0.056	0.036	0.283	2.00	1.110	
Eflite Pr 90	0.052	0.056	0.450	2.03	1.560	
Eflite Pr 110	0.054	0.063	0.490	2.50	2.112	
Eflite Pr 160	0.064	0.063	0.650	3.00	2.304	
Eflite Pr 180	0.082	0.064	0.642	3.40	2.763	
Align 730MX	0.056	0.052	0.380	4.33	2.553	18,870
EMAX GT5345	0.082	0.063	0.850	5.18	3.330	8,140
Eflite Pr 360	0.130	0.090	1.240	6.66		
EMRAX 207 HV	0.085	0.207	9.100	80.0	32	6,000
EMRAX 207 LV	0.085	0.207	9.100	80.0	32	6,000
Siemens DA-36		0.260	13.000	80.0		
EMRAX 228 HV	0.086	0.228	12.000	100	42	5,500
EMRAX 228 LV	0.086	0.228	12.000	100	42	5,500
EMRAX 268 HV	0.091	0.268	19.900	160	75	4,000
EMRAX 268 LV	0.091	0.268	19.900	160	75	4,000
YASA P400	0.080	0.305	24.000	160	100	8,000
YASA 400	0.075	0.280	24.000	165	70	7,500
Siemens SP260D	0.300	0.418	50.000	261		
Remy HVH250-090	0.147	0.242	33.500	297	176	10,600
Remy HVH250-115	0.180	0.242	43.000	305	185	10,600

## B.2 Data for Rotary Engine Scaling Trends

**Table B.2:** Data for rotary engine scaling trends

<b>Engine</b>	<b>L (m)</b>	<b>D (m)</b>	<b>m (kg)</b>	<b>P (kW)</b>	<b>RPM</b>	<b>SFC (kg/kWh)</b>
O.S. 49-PI Wankel	0.035	0.069	0.335	0.947	17,000	
Nitto NRG-20EP			1.8	1.34	10,000	
Nitto NRG-20EH			1.8	1.34	11,000	0.972
LiquidPiston X Mini	0.137	0.168	1.81	1.49	13,000	
Nitto NR-20EP			1.47	2.24	10,000	
Nitto NR-20EH			1.49	2.24	13,000	0.814
Cubewano Sonic 30			1.5	3.72	8,000	
Cubewano Sonic 35			3.5	5.96	8,500	0.487
Rotron 300 EFI	0.268	0.240	11.9	23.9	7,500	0.328
UEL AR 731	0.600	0.328	9.9	28.3	7,800	0.316
UEL AR 741	0.600	0.262	10.7	28.3	7,800	0.316
Meggitt Whirlwind			13.5	30.9	7,800	
Austro AE50R			24.5	40.4	7,750	
Rotron 600 LCR	0.420	0.274	21.2	43.3	7,500	0.322
UEL AR 801	0.305	0.325	19.5	44.7	8,000	0.304
UEL AR 801R			25.4	44.7		
UEL AR 612	0.535	0.385	26.8	55.9	8,500	0.304
UEL AR 682	0.609	0.440	26.8	55.9	8,000	0.316
UEL AR 682R	0.680	0.490	43.4	89.5	8,000	0.335



### B.3 Data for Turboprops and Turboshaft Scaling Trends

**Table B.3:** Data for turboprops and turboshaft scaling trends

<b>Engine</b>	<b>L (m)</b>	<b>D (m)</b>	<b>m (kg)</b>	<b>P (kW)</b>	<b>RPM</b>	<b>SFC (kg/kWh)</b>
Jakadofsky RS	0.260	0.113	1.30	4.00	17,400	1.823
Jakadofsky Pro	0.260	0.113	1.40	4.60	18,200	1.796
Jakadofsky Pro 5000	0.260	0.113	1.50	5.10	19,300	1.670
Jakadofsky Pro X	0.300	0.141	3.30	10.0	19,300	0.875
Innodyn 165TE	0.762	0.356	85.3	123	2,750	
PBS TP100	0.887	0.398	61.6	180	2,158	0.499
P & W Canada PT6A-6	1.575	0.483	123	373	2,200	0.394
Ivchenko-Progress AI-450	1.108	0.702	130	396	6,000	0.375
Turbomeca Arrius 1A	0.793	0.568	101	408		0.350
Rolls-Royce Model 250 C40B	1.040	0.638	127	457	9,598	0.380
Turbomeca Astazou X	1.912	0.460	163	477	2,400	0.312
GE Aviation Czech M601D	1.658	0.650	193	540	1,900	0.398
Turbomeca Arrius 2B1	0.947	0.692	111	560		0.333
GE Aviation Czech M601T	1.675	0.650	202	560	1,900	0.395
GE H80	1.670	0.580	177	634	2,080	0.356
P & W Canada PT6A-50	2.133	0.483	275	835	1,210	0.341
Omsk MKB TVD-20	1.900	0.850	240	1081	1,700	0.295
Omsk MKB TVD-20V	1.850	0.855	210	1119	3,115	0.308
P & W Canada PW118	2.057	0.635	391	1127	1,300	0.303
Honeywell TPE331-14GR/HR	1.333	0.660	287	1,462	1,552	0.305
Turbomeca RTM 322 Mk 250	1.171	0.736	256	1,694		0.269
General Electric CT7-6D	1.224	0.635	229	1,734		0.277
Rolls-Royce Dart Mk 542	2.527	0.963	628	2,051		0.338
Ivchenko-Progress TV3-117	2.954	1.209	570	2,089	1,200	0.252
Rolls-Royce Dart Mk 201	2.527	0.963	675	2,215		0.338
GE T64-IHI-10J	2.793	1.167	520	2,535		0.304
GE T64/P4D	2.793	1.167	538	2,535		0.304
Rolls-Royce Allison T56-A-7	3.686	1.016	746	2,800		0.321
P & W Canada PW150A	2.423	1.105	690	2,942	1,020	0.263
Rolls-Royce Allison T56-A-15	3.716	1.133	838	3,028		0.305
GE T64-GE-416	2.006	0.825	327	3,266		0.286
Rolls-Royce AE 2100D3	3.150	0.729	873	3,458	1,100	0.258
Europrop TP400-D6	3.500	0.925	1895	7,979	842	0.213
Ivchenko-Progress D-136	3.715	1.382	1077	9,098		0.265
Kuznetsov NK-12M	4.785	1.190	2,900	11,025	730	0.212

## C MISCELLANEOUS BATTERY DATA

**Table C.1:** Vehicle cell and pack-level battery data

Vehicle	Cell		Installed		
	Chemistry	$E_{\text{spec}}$ (Wh/kg)	$E_{\text{spec}}$ (Wh/kg)	$P_{\text{spec}}$ (W/kg)	Pack Mass Ratio
Honda Fit	LTO-NMC	89	63	317	1.40
Coda EV	G/LFP	116	78	243	1.48
Mitsubishi i-Miev	G/LMO-NMC	109	80	304	1.36
VW e-Up			81	324	
Nissan Leaf	G/LMO-NCA	155	82	312	1.89
Chevy Spark, 2013	G/LFP	131	83	380	1.58
Ford Focus EV			84	420	
Fiat 500	G/NMC-LMO	132	88	458	1.50
Chevy Spark, 2015	G/NMC-LMO	157	88	466	1.78
Renault Kangoo			92	212	
Renault Zoe	G/NMC-LMO	157	93	288	1.69
BMW i3			94	630	
Daimler Smart	G/NMC	152	101	313	1.50
Tesla Model S	G/NCA	233	133	333	1.75
Electric Cri Cri			125	852	
Pipistrel WattsUp			135	607	
Airbus E-fan	G/NMC	207	174	337	1.19
Airbus E-Genius			187	183	

## D DATA FOR CARSON CRUISE EFFICIENCY COMPARISON

**Table D.1:** Data for Carson cruise efficiency comparison

<b>Aircraft</b>	<b>Type</b>	<b>m (kg)</b>	<b>m<sub>empty</sub> (kg)</b>	<b>P (kW)</b>	<b>V (km/h)</b>
AgustaWestland AW-139	Helicopter	7000	3622	2250	309
Boeing AH-64 Apache	Helicopter	8000	5165	2089	265
Boeing CH-47	Helicopter	22680	11148	6668	291
Sikorsky Skycrane	Helicopter	19050	8724	4137	169
Sikorsky UH-60 Black Hawk	Helicopter	10660	4819	2368	278
Piasecki 16H Pathfinder	Compound	4865	2165	400	280
Convair XFY	Tailsitter	7370	5310	1095	648
Lockheed XFV	Tailsitter	7358	5261	1370	659
Bell X-22	Tiltduct	8003	4753	2187	343
Doak VZ-4	Tiltduct	1451	1043	329	282
Curtiss-Wright X-19	Tiltprop	6196	4425	1802	650
AgustaWestland AW609	Tiltrotor	7600	4755	2446	482
Bell Boeing V-22 Osprey	Tiltrotor	23859	15032	6173	446
Bell XV-15	Tiltrotor	6000	4574	1035	425
Bell XV-3	Tiltrotor	2218	1907	250	269
Canadair CL-84	Tiltwing	5710	3818	1822	485
Hiller XC-142A	Tiltwing	16900	10270	2520	463
Airbus A400M Atlas	Fixed-wing	141000	76500	27769	782
Alenia C-27J Spartan	Fixed-wing	30500	17000	6301	583
Antonov An-32	Fixed-wing	27000	16800	5341	470
Antonov An-8	Fixed-wing	40000	21250	3708	480
Canadair CC-109	Fixed-wing	24130	14666	4420	519
Embraer Super Tucano	Fixed-wing	5400	3200	825	520
Embraer/FMA CBA 123	Fixed-wing	7711	6230	1695	569
Lockheed C-130 Hercules	Fixed-wing	70300	34400	10424	541
Lockheed P-3 Orion	Fixed-wing	64400	35000	7522	607
Piaggio P.180 Avanti	Fixed-wing	5488	3799	633	589
Saab 2000	Fixed-wing	22800	13800	5722	666
Saab 340	Fixed-wing	13155	8140	2099	467
Sukhoi Su-80	Fixed-wing	14200	8350	1995	494
Tupolev Tu-95	Fixed-wing	188000	91000	27468	710

## E INTERNATIONAL STANDARD ATMOSPHERE

**Table E.1:** International Standard Atmosphere

<b>Altitude</b>	<b>Temperature</b>	<b>Pressure</b>	<b>Density</b>	<b>Speed of sound</b>	<b>Viscosity</b>
(m)	(Kelvin)	(pascal)	(kg/m <sup>3</sup> )	(m/s)	(Pa-s)
0	288.15	101325	1.225	340.294	1.81206E-05
1000	281.65	89874.6	1.11164	336.434	1.77943E-05
2000	275.15	79495.2	1.00649	332.529	1.74645E-05
3000	268.65	70108.5	0.909122	328.578	1.71311E-05
4000	262.15	61640.2	0.819129	324.579	0.000016794
5000	255.65	54019.9	0.736116	320.529	1.64531E-05
6000	249.15	47181	0.659697	316.428	1.61084E-05
7000	242.65	41060.7	0.589501	312.274	1.57596E-05
8000	236.15	35599.8	0.525168	308.063	1.54068E-05
9000	229.65	30742.5	0.466348	303.793	1.50498E-05
10000	223.15	26436.3	0.412707	299.463	1.46884E-05
11000	216.65	22632.1	0.363918	295.07	1.43226E-05
12000	216.65	19330.4	0.310828	295.07	1.43226E-05
13000	216.65	16510.4	0.265483	295.07	1.43226E-05
14000	216.65	14101.8	0.226753	295.07	1.43226E-05
15000	216.65	12044.6	0.193674	295.07	1.43226E-05
16000	216.65	10287.5	0.16542	295.07	1.43226E-05
17000	216.65	8786.68	0.141288	295.07	1.43226E-05
18000	216.65	7504.84	0.120676	295.07	1.43226E-05
19000	216.65	6410.01	0.103071	295.07	1.43226E-05
20000	216.65	5474.89	0.0880349	295.07	1.43226E-05
21000	217.65	4677.89	0.0748737	295.75	1.43792E-05
22000	218.65	3999.79	0.0637273	296.428	1.44357E-05
23000	219.65	3422.43	0.0542803	297.105	0.000014492
24000	220.65	2930.49	0.0462674	297.781	1.45483E-05
25000	221.65	2511.02	0.0394658	298.455	1.46044E-05

## REFERENCES

1. Anon., General Atomics Aeronautical Systems, *USAF MQ-9 Reaper*, (<http://www.ga-asi.com/predator-b>).
2. Anon., AeroVironment, Inc, *Raven*, ([https://www.avinc.com/images/uploads/product\\_docs/USAF\\_Raven\\_FactSheet\\_2.pdf](https://www.avinc.com/images/uploads/product_docs/USAF_Raven_FactSheet_2.pdf)).
3. Anon., National Agricultural Aviation Association, *Yamaha RMAX Aerial Application UAV Approval*, 2015, (<http://www.agaviation.org/rmax>).
4. Verne, J., *The clipper of the clouds* (Sampson Low, Marston, Searle, Rivington, 1887).
5. Canis, B., *Unmanned Aircraft Systems (UAS): Commercial Outlook for a New Industry* (United States Congress, 2015).
6. Anon., Deloitte Touche Tohmatsu Limited, *Deloitte*, (<http://www2.deloitte.com/global/en/pages/technology-media-and-telecommunications/articles/tmt-pred-drones-high-profile-and-niche.html>) (2015).
7. Carlson, W. B., *Tesla: Inventor of the Electrical Age* (Princeton University Press, 2013).
8. Tesla, N., *Method of and apparatus for controlling mechanism of moving vessels or vehicles*, Nov. 1898.
9. Rengel, A., *Privacy in the 21st Century* (Brill, 2013).
10. Hare, T. V., *Aerial Target*, (<http://fly.historicwings.com/2013/08/the-first-drone/>).
11. Anon., Monash University, *Kettering Aerial Torpedo 'Bug' ready for launch*, ([http://www.ctie.monash.edu.au/hargrave/rpav\\_usa.html](http://www.ctie.monash.edu.au/hargrave/rpav_usa.html)).
12. Hare, P. R., *The Royal Aircraft Factory* (Putnam Aeronautical, 1990).
13. Newcome, L., *Unmanned Aviation: A Brief History of Unmanned Aerial Vehicles* (American Institute of Aeronautics and Astronautics, 2004).
14. Keane, J. F., Carr, S. S., *Johns Hopkins APL Technical Digest* **32**, ([http://www.jhuapl.edu/techdigest/td/td3203/32\\_03-keane.pdf](http://www.jhuapl.edu/techdigest/td/td3203/32_03-keane.pdf)) (2013).
15. *OQ-2A Launch (detail)*, ([http://www.ctie.monash.edu.au/hargrave/rpav\\_radioplane3.html](http://www.ctie.monash.edu.au/hargrave/rpav_radioplane3.html)).
16. *The Ruhrstahl SD 1400 'Fritz X' Air-to-Ship, Wireless Guided, Gliding Bomb*, ([http://www.ctie.monash.edu.au/hargrave/rpav\\_germany\\_hr.html](http://www.ctie.monash.edu.au/hargrave/rpav_germany_hr.html)).
17. Piehler, G., *Encyclopedia of Military Science* (SAGE Publications, 2013).

18. Ordway, F. I., Wakeford, R. C., *Radioplane MQM-57A*, (<http://www.designation-systems.net/dusrm/m-57.html>).
19. Anon., Northrop Grumman Corporation, *BQM-34 Firebee Aerial Target System*, (<http://www.northropgrumman.com/MediaResources/Pages/PhotoGallery.aspx>).
20. Wagner, W., *Lightning Bugs and Other Reconnaissance Drones* (Armed Forces Journal, 1982).
21. Anon., *Scout*, (<http://www.israeli-weapons.com/weapons/aircraft/uav/scout/Scout.html>).
22. Anon., Defense Technical Information Center, *RQ-2A Pioneer UAV*, (<http://www.dtic.mil/dtic/tr/fulltext/u2/a469608.pdf>).
23. Zaloga, S., Palmer, I., *Unmanned Aerial Vehicles: Robotic Air Warfare, 1917-2007* (Osprey, 2008).
24. Anon., United States Navy, *RQ-7B Shadow*, (<http://www.htii.com/holmes-tucker-installs-aircraft-pictorial-tribute-to-its-veterans/>).
25. Anon., United States Air Force, *General Atomics MQ-1 Predator*, (<https://warisboring.com/u-s-air-force-pulls-predators-from-djibouti-c2325c0283c#.ci5adrvzd>).
26. Mueller, T. J., *International Journal of Micro Air Vehicles* (2009).
27. Anon., United States Department of Defense, *Inventory of DoD UAS, 2013*, (<http://www.defense.gov/portals/1/documents/pubs/dod-usrm-2013.pdf>).
28. Anon., United States Department of Defense, *Unmanned Systems Integrated Roadmap FY2013-2038, 2013*, (<http://www.defense.gov/portals/1/documents/pubs/dod-usrm-2013.pdf>).
29. Hildebrandt, E., *Fly Navy, Celebrating the First Century of Naval Aviation*, ([http://www.northropgrumman.com/mediaresources/mediakits/naval100/documents/fly\\_navy\\_calendar.pdf](http://www.northropgrumman.com/mediaresources/mediakits/naval100/documents/fly_navy_calendar.pdf)).
30. Anon., G., *The DASH Weapon System*, (<http://www.gyrodynehelicopters.com>).
31. Anon., Franche-Comte Museums, *Oehmichen No. 2*, ([http://www.musees-franche-comte.com/index.php?p=5&art\\_id=38](http://www.musees-franche-comte.com/index.php?p=5&art_id=38)).
32. Anon., Smithsonian Institution, *De Bothezat Flying Octopus*, (<http://www.heartlandscience.org/aeroav/>).
33. Anon., *DJI Phantom 3 - 05 Der erste Flug*, (<https://www.youtube.com/watch?v=TsCsKWQP7I>).
34. Anon., Mobile Recon Systems, *Video*, ([http://www.mobilereconsystems.com/?page\\_id=188](http://www.mobilereconsystems.com/?page_id=188)).
35. Manteufel, R., *Dornier Do-31, 1968*, (<http://www.airliners.net/photo/Germany-Air-Force/Dornier-Do-31E/1265410>).
36. Anon., United States Marine Corps, *F-35B Lightning II, 2013*, (<https://www.f35.com/media/photos-detail/first-f-35b-vertical-landing-at-mcas-yuma3>).

37. Anon., NATO Association of Canada, *Canadair CL-84*, (<http://natoassociation.ca/the-osprey-or-the-albatross/>).
38. Anon., United States Air Force, *Bell Boeing V-22 Osprey*, (<https://commons.wikimedia.org/wiki/File:58thoperationsgroup-ospry-2.jpg>).
39. Anon., (<http://www.airliners.net/photo/UK-Air-Force/Hawker-Siddeley-Harrier-GR3/750455>).
40. Anon., ([https://upload.wikimedia.org/wikipedia/commons/thumb/d/d2/Ryan\\_VZ-3RY\\_Vertiplane.jpg/1280px-Ryan\\_VZ-3RY\\_Vertiplane.jpg](https://upload.wikimedia.org/wikipedia/commons/thumb/d/d2/Ryan_VZ-3RY_Vertiplane.jpg/1280px-Ryan_VZ-3RY_Vertiplane.jpg)).
41. Anon., *Niezwykłe samoloty Hitlera II*, (<http://www.wykop.pl/ramka/2348420/niezwykłe-samoloty-hitlera-ii/>).
42. Anon., *XFY-1 Pogo*, (<http://www.airwar.ru/enc/xplane/xfy1.html>).
43. *Vertical Takeoff and Landing Experimental Plane (VTOL X-Plane)*, 2015, (<http://www.darpa.mil/news-events/2015-12-28>).
44. Hambling, D., *Popular Mechanics* (Apr. 2010).
45. Barrett, R., *Volume I: Technical Management Proposal* (KU Transportation Research Institute, 2013).
46. Anon., Aurora Flight Sciences, *LightningStrike*, 2016, (<http://www.aurora.aero/lightningstrike/>).
47. Bagai, A., *Vertical Takeoff and Landing Experimental Plane (VTOL X-Plane)*, 2013, (<http://www.darpa.mil/program/vertical-takeoff-and-landing-experimental-plane>).
48. Anon., Aurora Flight Sciences, *DARPA Selects Aurora to Build VTOL X-Plane Technology Demonstrator*, 2016, (<http://www.multivu.com/players/English/7617851-aurora-flight-sciences-vtol-xplane-darpa/>).
49. Barrett, R. M., et al, *AERIAL VEHICLES AND METHODS OF USE*, Jan. 21, 2016.
50. Anon., QuadRKT, LLC, *QuadRKT Shop*, (<http://quadrkt.com/product/quadrkt/>).
51. Anon., American Helicopter Society, *V/STOL aircraft and propulsion concepts*, ([www.vtol.org/wheel](http://www.vtol.org/wheel)).
52. Anon., *IHS Jane's Database*, 2016, (<https://janes.ihs.com>).
53. Anon., AviaStar, *Nord Aviation Nord-500*, 2007, ([http://www.aviaStar.org/helicopters\\_eng/nord-500.php](http://www.aviaStar.org/helicopters_eng/nord-500.php)).
54. *Vertipedia*, 2016, (<http://vertipedia.vtol.org/>).
55. White, J. T., *Convair XFY-1 Pogo*, 2010, (<http://blog.seattlepi.com/americanaerospace/2010/11/01/convair-xfy-1-pogo/>).
56. Anon., *Ryan VZ-3*, 2013, (<http://www.globalsecurity.org/military/systems/aircraft/vz-3.htm>).
57. Yaggy, P. F., Mort, K. W., *NASA Technical Note D-776: A Wind-Tunnel Investigation of a 4-Foot-Diameter Ducted Fan Mounted on the Tip of a Semispan Wing*, 1961.
58. Anon., Curtiss-Wright Corporation, *Technical Report AD826319: The X-19 V/STOL Technology - A Critical Review*, 1967.

59. Anon., Bell Aerospace Company, *Technical Report AD871466: X-22A Tri-Service V/STOL Aircraft Final Progress Report*, 1970.
60. Leishman, J. G., *Principles of helicopter aerodynamics* (Cambridge University Press, 2006).
61. Munson, B. R., Young, D. F., Okiishi, T. H., *Fundamentals of fluid mechanics* (J. Wiley Sons, 2006).
62. Anon., *Airfoil Tools*, (<http://airfoiltools.com/>).
63. Pounds, P. E., Mahony, R. E., Corke, P. I., *J. Aerosp. Eng. Journal of Aerospace Engineering* **22**, 85–94 (2009).
64. Johnson, W., *Rotorcraft Aeromechanics* (Cambridge University Press, 2013).
65. Anon., Smart Rotor Systems, *Smart Rotor Systems*, (<http://www.smartrotorsystems.ca/>).
66. Farokhi, S., *Aircraft Propulsion, 2nd Edition* (John Wiley Sons, 2014).
67. Anon., United States Department of Energy, *Gas Turbines in Simple Cycle Combined Cycle Applications*.
68. Prouty, R. W., Coyle, S., *Helicopter aerodynamics* (Eagle Eye Solutions, 2009).
69. Cooke, A. K., Fitzpatrick, E. W. H., *Helicopter test and evaluation* (American Institute of Aeronautics and Astronautics, 2002).
70. Anon., United States Department of Defense, ([https://fas.org/irp/doddir/dod/jp3\\_09\\_3.pdf](https://fas.org/irp/doddir/dod/jp3_09_3.pdf)) (Nov. 2014).
71. Wilde, P. R. (2012).
72. Anon., Office of the Secretary of Defense, ([https://fas.org/irp/program/collect/uav\\_roadmap2005.pdf](https://fas.org/irp/program/collect/uav_roadmap2005.pdf)) (2005).
73. Anon., U.S. Geological Survey, 2013, ([http://uas.usgs.gov/pdf/THawk/THawk\\_poster\\_24x32.pdf](http://uas.usgs.gov/pdf/THawk/THawk_poster_24x32.pdf)).
74. Law, W., *A Serious Call to a Devout and Holy Life* (William Innys, 1729).
75. RC, E.-F., *Brushless Motors*, 2016, (<http://www.e-fliterc.com/powersystems/motors/brushless.aspx>).
76. Anon., ElectriFly, *Motors Systems*, 2016, (<http://www.electrifly.com/motorsgears.html>).
77. Anon., ALIGN Corporation, Ltd, *Brushless Motor Manuals*, 2015, (<http://www.align.com.tw/manuals-en/motor/>).
78. Anon., YASA Motors, *The YASA Product Range*, 2016, (<http://www.yasamotors.com/products/>).
79. Anon., Remy International, Inc, *Remy Electric Motors for Electric and Hybrid Applications*, 2016, (<https://www.remyinc.com/Hybrid.aspx>).
80. Anon., EMAX, *Products*, 2016, (<http://www.emaxmodel.com/>).
81. Anon., National Aeronautics and Space Administration, *Transformative Vertical Flight Workshop 2015*, 2015, (<http://nari.arc.nasa.gov/sites/default/files/attachments/Korbinian-TVFW-Aug2015.pdf>).



82. Anon., Jakadofsky Jet Engines, *Specifications: Gearbox Information*, 2015, ([http://www.jakadofsky.com/htm\\_en/daten.htm](http://www.jakadofsky.com/htm_en/daten.htm)).
83. Anon., Turbine Solution Group, Inc, *TP100 Turboprop Engine*, 2016, ([http://www.turbinesolutiongroup.com/tsg\\_TP100.htm](http://www.turbinesolutiongroup.com/tsg_TP100.htm)).
84. Anon., Rotron Power Ltd, *Rotron Products Brochure*, 2015, (<http://www.rottronuav.com/pdfs/RottronBrochure.pdf>).
85. Anon., UAV Engines Ltd, *Products: UAV Engines*, 2016, (<http://www.uavenginesltd.co.uk/products/>).
86. Anon., Meggitt Target Systems, *Whirlwind UAV Engine*, 2015, ([https://meggitttargetsystems.com/static/media/files/Whirlwind\\_2015.pdf](https://meggitttargetsystems.com/static/media/files/Whirlwind_2015.pdf)).
87. Anon., Barnard Microsystems Ltd, *Wankel Engines*, 2015, (<http://www.barnardmicrosystems.com/UAV/engines/wankel.html>).
88. Thomas, G., *Overview of Storage Development DOE Hydrogen Program*, May 2000, (<http://www1.eere.energy.gov/hydrogenandfuelcells/pdfs/storage.pdf>).
89. Anderman, M., *The Tesla Battery Report*, Nov. 2014, (<http://www.totalbatteryconsulting.com/industry-reports/Tesla-report/Extract-from-the-Tesla-battery-report.pdf>).
90. Anderman, M., *The xEV Industry Insider Report*, Nov. 2014, ([totalbatteryconsulting.com/industry-reports/Extract-from-the-xEV-Industry-Report.pdf](http://www.totalbatteryconsulting.com/industry-reports/Extract-from-the-xEV-Industry-Report.pdf)).
91. Anon., Airbus Group, *E-FAN: The New Way to Fly*, 2015, (<https://www.airbusgroup.com/service/mediacenter/download/?uuid=48b1bd2c-a428-4c65-82e5-ed3e923bd142>).
92. Anon., CNET, 2014, (<http://www.cnet.com/au/pictures/airbus-electric-e-fan-training-plane-pictures/2/>).
93. Anon., Joby Aviation, 2015, (<http://www.ecotechtube.com/photo/flashreleases2015/Joby3.jpg>).
94. Kroninger, C. M., Harrington, A., Munson, M., *52nd Aerospace Sciences Meeting* (Oct. 2014).
95. Anon., UQM Technologies, 2010, (<https://www.neweagle.net/support/wiki/docs/Datasheets/UQM/PP75.pdf>).
96. Anon., A123 Systems, Inc, *20Ah Prismatic Pouch Cell Product Data Sheet*, 2015, (<http://www.a123systems.com/prismatic-cell-amp20.htm>).
97. Anon., Altairnano, *60 Amp Hour Cell*, 2015, (<http://www.altairnano.com/products/60-amp-hour-cell/>).
98. Anon., Leclanche, *LecCell 30Ah High Energy Sales Brochure*, 2015, (<http://www.leclanche.eu/img/pdf/Brosch%C3%BCren/LecCell1936C082015-03-03X4WEB.pdf>).
99. Anon., Leclanche, *LecCell G/NMC 43Ah/160Wh*, 2015, (<http://www.leclanche.eu/img/pdf/Brosch%C3%BCren/LecCell1946A012015-03-03X4.pdf>).
100. Anon., Phostech, *Life Power LFMP*, 2015, ([http://www.phostechlithium.com/prd\\_LiFeMnPO\\_e.php](http://www.phostechlithium.com/prd_LiFeMnPO_e.php)).

101. Anon., Toshiba, *SciB Rechargeable Battery Sales Brochure*, 2014, (<https://www.evhangar.com/wp-content/uploads/2015/02/Toshiba-SCiB-Brochure-2014-Final.pdf>).
102. Anon., Valence Technology, *Power Cells*, 2015, (<https://www.valence.com/products/cells/>).
103. Anon., A123 Systems, Inc., *Nanophosphate□ Basics: An Overview of the Structure, Properties and Benefits of A123 Systems□ Proprietary Lithium Ion Battery Technology*, 2011, ([https://www.neces.com/assets/A123-Systems\\_Nanophosphate-overview-whitepaper\\_FINAL1.pdf](https://www.neces.com/assets/A123-Systems_Nanophosphate-overview-whitepaper_FINAL1.pdf)).
104. Anon., Kokam, *Superior Lithium Polymer Battery (SLPB) KOKAM Li-ion/Polymer Cell*, 2016, (<http://kokam.com/wp-content/uploads/2016/03/SLPB-Cell-Brochure.pdf>).
105. Anon., Trojan Batteries, *Product Literature*, 2016, (<http://www.trojanbattery.com/literature/>).
106. Anon., Interstate Batteries, *Marine batteries*, (<http://www.interstatebatteries.com/m/category/marine/deepcycle>).
107. Anon., Discover Energy, *Discover EV Traction Dry Cell*, ([http://www.harrisbattery.com/sites/default/files/applications\\_downloads/Discover-EV-Traction-Dry-Cell-Brochure.pdf](http://www.harrisbattery.com/sites/default/files/applications_downloads/Discover-EV-Traction-Dry-Cell-Brochure.pdf)).
108. Anon., U.S. Battery, *US-2200XC2*, ([https://www.wetac.nl/media/filer\\_public/2014/12/01/us-2200\\_xc2\\_1.pdf](https://www.wetac.nl/media/filer_public/2014/12/01/us-2200_xc2_1.pdf)).
109. Anon., Power-sonic, *Nickel Cadmium and Nickel-Metal Hydride Rechargeable Batteries and Chargers*, ([http://www.power-sonic.com/images/powersonic/technical/1277751010\\_20106027-NiCdCatalog-Lo.pdf](http://www.power-sonic.com/images/powersonic/technical/1277751010_20106027-NiCdCatalog-Lo.pdf)).
110. Anon., Cobasys, 2007, (<http://www.cobasys.com/pdf/transportation/Series9500Brochure.pdf>).
111. Anon., Nilar Energy, *Nilar Energy Battery Technical Manual*, 2015, (<http://www.nilar.com/wp-content/uploads/2015/12/Nilar-Energy-Battery-Technical-manual-NIL16-0046.pdf>).
112. Hausmann, A., Depcik, C., *Journal of Power Sources* **235**, 148□158 (2013).
113. Anon., Rotron Power Ltd, 2016, (<http://www.rotroonuav.com/images/rotron-engine-application.png>).
114. Anon., Forbes Media LLC, 2014, (<http://blogs-images.forbes.com/davidprosser/files/2014/04/photo-of-e-go-aeroplane-flying.jpg>).
115. Anon., Rotron Power Ltd, 2016, (<http://www.rotroonuav.com/images/rotron-engine-application.png>).
116. Gudmundsson, S., *General aviation aircraft design: applied methods and procedures* (Elsevier, 2013).
117. Von Mises, R., *Theory of flight* (Dover Publications, 1959).

118. Hannum, R. W., Zimmerman, R. H., *Calculations of the economy of an 18-cylinder radial aircraft engine with an exhaust-gas turbine geared to the crankshaft at cruising speed* (National Advisory Committee for Aeronautics, 1945).
119. Pinkel, B., Turner, L. R., Voss, F., Humble, L. V., *Report No. 765: Exhaust-Stack Nozzle Area and Shape for Individual Cylinder Exhaust-Gas Jet-Propulsion System*, 1948.
120. Turner, L. R., White, M. D., *Flight Tests of NACA Jet-Propulsion Exhaust Stacks*, 1942.
121. Raymer, D. P., *Aircraft design: a conceptual approach* (American Institute of Aeronautics and Astronautics, 2006).
122. Hesse, W. J., Mumford, N., *Jet Propulsion for Aerospace Applications* (Pitman Publishing Corporation).
123. Aeronautics, N., Administration, S., 2015, (<http://www.nasa.gov/sites/default/files/thumbnails/image/gl10-hover-02.jpg>).
124. Anon., Horizon Aircraft, Inc, 2016, (<http://www.horizonaircraft.com/wp-content/uploads/2014/07/Horizon-Aircraft-X3-Prototype-Clouds.jpg>).
125. Rogoway, T., *DARPA's Revolutionary New VTOL X-Plane Design Looks Out Of This World*, Mar. 2016, (<http://foxtrotalpha.jalopnik.com/dapras-revolutionary-new-vtol-x-plane-design-looks-out-1762948914>).
126. C. W. Acree R.J. Peyran Jr., W. J., *Rotor Design Options for Improving XV-15 Whirl-Flutter Stability Margins*, Mar. 2004.
127. Anon., Advanced Precision Composites, *Engineering*, 2016, (<https://www.apcprop.com/Articles.asp?ID=262>).
128. Modarres, R., *Ideal Optimum Performance of Propellers, Lifting Rotors and Wind Turbines*, Aug. 2013.
129. Drela, M., *Xfoil, Subsonic Airfoil Development System*, 2013, (<http://web.mit.edu/drela/Public/web/xfoil/>).
130. Robert E. Sheldahl Paul C, K., *Aerodynamic Characteristics of Seven Symmetrical Airfoil Sections Through 180-Degree Angle of Attack for Use in Aerodynamic Analysis of Vertical Axis Wind Turbines*, Mar. 1981, ([www.osti.gov/servlets/purl/6548367/](http://www.osti.gov/servlets/purl/6548367/)).
131. Montgomerie, B., *Drag Coefficient Distribution on a Wing at 90 Degrees to the Wind*, Feb. 1996, (<ftp://ftp.ecn.nl/pub/www/library/report/1995/c95061.pdf>).
132. Traub, L. W., Snyder, R., Pellino, T., *Journal of Aircraft* **47**, 1068–1073 (2010).
133. Traub, L. W., Nix, T., *Journal of Aircraft* **49**, 183–192 (2012).
134. Anon., Hanley Innovations, *MultiSurface Aerodynamics and 3DFoil*, 2016, (<http://www.hanleyinnovations.com/multisurface/>).
135. Anon., Federal Aviation Administration, *art 23 AIRWORTHINESS STANDARDS: NORMAL, UTILITY, ACROBATIC, AND COMMUTER CATEGORY AIRPLANES*, 2016, ([http://rgl.faa.gov/Regulatory\\_and\\_Guidance\\_Library%5CrgFAR.nsf/0/D35E170180C8CB2185256687006D0C90?OpenDocument](http://rgl.faa.gov/Regulatory_and_Guidance_Library%5CrgFAR.nsf/0/D35E170180C8CB2185256687006D0C90?OpenDocument)).
136. Anon., Federal Aviation Administration, *Part 25 AIRWORTHINESS STANDARDS: TRANSPORT CATEGORY AIRPLANES*, 2016, ([http://rgl.faa.gov/Regulatory\\_and\\_Guidance\\_Library%5CrgFAR.nsf/0/5D3CEA6C015DDA8685256672004EC387?OpenDocument](http://rgl.faa.gov/Regulatory_and_Guidance_Library%5CrgFAR.nsf/0/5D3CEA6C015DDA8685256672004EC387?OpenDocument)).

137. Anon., Federal Aviation Administration, *Part 27 AIRWORTHINESS STANDARDS: NORMAL CATEGORY ROTORCRAFT*, 2016,  
([http://rgl.faa.gov/Regulatory\\_and\\_Guidance\\_Library%5CrgFAR.nsf/0/AEAD1A7505EF922F852565F6006C1678?OpenDocument](http://rgl.faa.gov/Regulatory_and_Guidance_Library%5CrgFAR.nsf/0/AEAD1A7505EF922F852565F6006C1678?OpenDocument)).
138. Anon., Federal Aviation Administration, *Part 29 AIRWORTHINESS STANDARDS: TRANSPORT CATEGORY ROTORCRAFT*, 2016,  
([http://rgl.faa.gov/Regulatory\\_and\\_Guidance\\_Library%5CrgFAR.nsf/0/9DEF90770C26A3EC85256613006B2A8B?OpenDocument](http://rgl.faa.gov/Regulatory_and_Guidance_Library%5CrgFAR.nsf/0/9DEF90770C26A3EC85256613006B2A8B?OpenDocument)).
139. Martin Neubauer Georg Günther, K. F., *Structural Design Aspects and Criteria for Military UAVs*, 2007, ([www.dtic.mil/cgi-bin/GetTRDoc?AD=ADA479056](http://www.dtic.mil/cgi-bin/GetTRDoc?AD=ADA479056)).
140. Stoll, A. M., Mikic, G. V., *Design Studies of Thin-Haul Commuter Aircraft with Distributed Electric Propulsion*, June 2016,  
([www.jobyaviation.com/DesignStudiesOfThinHaulAircraft.pdf](http://www.jobyaviation.com/DesignStudiesOfThinHaulAircraft.pdf)).
141. Nicolai, L. M., Carichner, G. E. (2010).
142. Norrarra, H., *Die Deutsche Luftrüstung 1933-1945*, 1985.
143. Carson, B., *Journal of Aircraft* **19**, 473–479 (1982).
144. Green, S. R., *Spirits from beyond* (Ace Books, 2013).
145. Anon., E-flite, *Power 10 Brushless Outrunner Motor, 1100Kv*, 2016,  
(<http://www.e-fliterc.com/Products/Default.aspx?ProdID=EFLM4010A>).
146. Anon., *Home of the Drive Calculator*, 2016, (<http://www.drivecalc.de/>).
147. Anon., Advanced Precision Composites, *12x6E*, 2016,  
([http://www.apcprop.com/product\\_p/lp12060e.htm](http://www.apcprop.com/product_p/lp12060e.htm)).
148. Anon., HobbyKing, *Turnigy H.A.L. (Heavy Aerial Lift) Quadcopter Frame 585mm*, 2016,  
([https://hobbyking.com/en\\_us/turnigy-h-a-l-heavy-aerial-lift-quadcopter-frame-585mm.html](https://hobbyking.com/en_us/turnigy-h-a-l-heavy-aerial-lift-quadcopter-frame-585mm.html)).
149. Jarrett, P., *The color encyclopedia of incredible airplanes* (DK Publishing, 2007).
150. Whitman, W., Cowley, M., *The works of Walt Whitman* (Funk Wagnalls, 1968).